NANOMECHANICS, NANOTRIBOLOGY AND SURFACE INTERACTIONS OF ULTRA THIN FILMS

A Dissertation

by

AHMAD SHAHEDI SHAKIL

Submitted to the Graduate and Professional School of
Texas A&M University
in partial fulfillment of the requirements for the degree of

DOCTOR OF PHILOSOPHY

Chair of Committee,	Andreas A. Polycarpou
Committee Members,	M. Cynthia Hipwell
	Matt Pharr
	George M. Pharr
Head of Department,	Guillermo Aguilar

December 2021

Major Subject: Mechanical Engineering

ABSTRACT

In this research, nanomechanical and nanotribological studies have been performed though experiments, finite element analysis, and analytical modeling to obtain maximum reliability of different thin film applications in terms of contacts between the surfaces at different temperatures and environmental conditions. Three types of contact conditions were considered in this study- solid-solid contact for hard coatings, solid-solid contact for soft coatings and solid-liquid contacts. One of the applications of solid-solid contact is heat assisted magnetic recording (HAMR) that utilizes nitrogen doped carbon overcoat (NCOC) or nitrogen doped diamond like carbon (NDLC) to protect the magnetic media. Nanotribological and nanomechanical studies were performed at different temperatures on NCOCs of different thicknesses (2.5, 3.5 and 4.5 nm). It was found that thicker NCOC led to better mechanical behavior and less wear at high temperature conditions, making them tribologically robust at high temperature. Due to difficulty in extracting true mechanical properties from pure experiments, finite element analysis (FEA) was also introduced in this research to determine nanomechanical properties of NCOCs with reduced substrate effect. The effect of carbon configuration of NDLCs on their mechanical and tribological behavior was also studied and found that higher sp^3 carbon contents led to better mechanical and wear performance and lower friction at different temperature conditions. Graphene oxide (GO), silicon fibroin (SF) and cellulose nanocrystal (CNC) nanocomposite was studied as a potential soft biomaterial for wearable electronics, thermal interfaces and protecting coatings for cooling components in electronic devices. Due to the nature of these applications, creep performance is crucial for overall reliability of the composite at elevated temperatures for longer time durations. In this study,

nanoindentation creep experiments were performed and FEA was used to determine creep properties of GO-SF-CNC coatings at different temperatures. Surface haptics is a state-of-the-art thin film application where voltage is applied to obtain tactile sensation between fingertips and the haptic device. Electroadhesion is a widely used term for the application where adhesion between the surfaces is influenced by external voltage. Fingertip contains sweat, sebum and moisture, which creates a solid-liquid interface, and this can affect the tactile sensation. An improved single asperity electroadhesion model was developed in this research to predict interfacial forces at different environmental conditions and the model was extended to a rough surface contact model to predict interfacial forces between the fingertip and the haptics surface over a finite region.

ACKNOWLEDGEMENTS

First of all, I would like to express my sincere gratitude to my advisor, Professor Andreas A. Polycarpou, for his resourceful guidance, steady support, and encouragement during all of the work toward this dissertation. He has been giving feedback and advice of great value all the time, both for research and personal life. I could not have successfully conducted and published all my research without his insightful input.

I would also like to thank my committee members, Dr. M. Cynthia Hipwell, Dr. Matt Pharr and Dr. George M. Pharr for their insightful suggestions and valuable comments throughout the research.

I would like to thank all members of Microtribodynamics research group for their help and support throughout the journey. Especially, I would like to thank Mohammad Humood, Youfeng Zhang, Md. Saifur Rahman, Jevon Phandi and Kian Bashandeh for their valuable help in research and also in graduate life.

I would like to thank Drs. H. Tang, H. Wang, C. Platt and X. Li for sample preparation and helpful discussions for the magnetic storage study. I would also like thank Dr. Sunghan Kim, Professor of Chung-Ang University in South Korea, and his students for preparing the GO-SF-CNC biocomposite samples. Special thanks to Dr. M. Cynthia Hipwell and her students for helpful discussions and suggestions for the haptics study.

I am indebted to my parents, Md. Shahid Ullah and Lutfun Nahar Lucky, for their immense love and support in my entire life. Without their perseverance and guidance, I would not be able to reach to this destination. I am also grateful to my in-laws for their

encouragement and support. I will always be grateful to my wife, Rajikun Nahar Nipa, for keeping faith in me and always encouraging me for the graduate study and most of all, giving birth to our lovely son, Adyan Ahmad, who brought joy and happiness to our family. Finally, I thank Almighty Allah for everything in my entire life.

CONTRIBUTORS AND FUNDING SOURCES

Contributors

This work was supervised by a dissertation committee consisting of Professors Andreas A. Polycarpou, M. Cynthia Hipwell, and Matt Pharr of the J. Mike Walker ’66 Department of Mechanical Engineering and Professor George M. Pharr of the Department of Material Science & Engineering.

The XPS results presented in Chapter II and Chapter IV were obtained and analyzed with the help of Dr. Ahmad Amiri, Visiting Assistant Professor of the J. Mike Walker ’66 Department of Mechanical Engineering. All XPS studies were performed at the Materials Characterization Facility located at Texas A&M University.

All other work conducted for the dissertation was completed by the student independently.

Funding Sources

The motivation of the works in Chapters II-IV were through a sponsored research program from Seagate Technology LLC, through Grant No. SRA-32724.

Part of the research in Chapter V was sponsored from a summer graduate research grant by the J. Mike Walker ’66 Department of Mechanical Engineering, Texas A&M University.

The study in Chapter VI was funded from the X-Grant Program by Texas A&M University.

TABLE OF CONTENTS

Page

LIST OF FIGURES

Page

LIST OF TABLES

Page

CHAPTER I

INTRODUCTION

Thin films are being widely used in different applications to protect components of unexpected failure. Depending on the applications, thin films need to be as reliable as possible, ranging from low temperature to high temperature applications. To ensure reliability, mechanical and tribological investigations are integral part of development of a new system. Thin films might be hard or soft, depending on whether the hardness is higher or lower than 10 GPa [1]. Some newer applications also involve the presence of foreign substance, which also effect the overall reliability of the system. This research aims at investigating the nanomechanical and nanotribological behavior of different thin film systems and predicting interfacial forces and the optimum properties for maximum reliability. Also, in one of the cases, a continuum-based nanomechanics model is developed and correlated with existing literature.

One of the state-of-the-art systems that utilizes hard coatings is heat assisted magnetic recording (HAMR) technology. As a novel high temperature (HT) application, HAMR technology uses diamond like carbon (DLC), also known as carbon overcoat (COC), to protect the magnetic materials from permanent deformation, where the magnetic disks are temporarily heated to HT using a laser during the writing process [2,3]. Literature shows that the laser heating and cooling cycle takes about 1 ns [4]. Temporarily heating makes the magnetic disks more amenable to magnetic effects, and increases the areal density, and thus data storage capacity. However, in spite of the effectiveness of HAMR, the

unidentified outcome of laser heating on the mechanical and chemical stability of the COC is of great concern. Also, COC needs to protect the magnetic media from damage due to unexpected contact of the recording head on the moving disk, which is critical at HT [5,6]. The utilization of nitrogen-doped COC (NCOC) has attracted numerous researchers in HAMR applications. Nitrogen doping has been used to improve thermal stability, friction, wear, and nanomechanical behavior of DLC [7,8].

The spacing between the recording head and magnetic media, commonly known as head-media spacing (HMS) is extremely important for the successful operation of HAMR drives. To achieve maximum areal density, HMS needs to be as small as possible [9]. The lower the thickness of NCOCs is used, the lower HMS can be achieved. At the same time, NCOCs have to be sufficiently robust to protect the media in case of accidental contact, especially at HT. The study of NCOC thickness dependence on HT nanomechanical and nanotribological behavior has also not received significant attention. In this research, nanomechanical and nanotribological experiments were performed to investigate NCOC's behavior with different thickness at different temperature conditions.

The true mechanical properties of sub-5 nm NCOCs cannot be obtained from pure experiments without substrate effect. To maintain robustness of the system, obtaining accurate mechanical properties of ultra-thin NDLC coatings at different temperature conditions are of great interest. At the same time, nanomechanical properties of other components, such as FeCo metal layer and glass substrate are also of great importance for overall robustness of HAMR media, especially during high temperature transient operations. Finite element analysis (FEA) has been frequently used with nanoindentation

to predict nanomechanical properties of thin films without substrate effect. In this case, FEA simulations are performed with varying mechanical properties of the material in order to correlate with experimental nanoindentation responses. In this research, FEA was applied using truncated sphere geometry to accurately predict different HAMR components, especially NDLCs, at different temperature conditions.

Chemical composition also plays an important role for the mechanical and tribological reliability of NDLCs. Especially, laser heating to high temperature can lead to changes in chemical structure, which may affect the behavior. For this reason, the effects of chemical configuration of sub- 5 nm NDLCs on their high temperature mechanical and tribological behavior are also of great importance, although it has not received significant attention, primarily due to instrumentation challenges. Specifically, sp^3 and sp^2 hybridized carbon contents can affect reliable performance of sub-5 nm NDLCs before and after heat treatment, which was not thoroughly studied. This research also aimed at investigating carbon configuration of NDLCs and their contribution to mechanical and tribological properties.

Soft thin films are also being used as protective coatings for different medium temperature applications. Their mechanical performances are affected by their viscous behavior and it needs to be considered to investigate their reliability in a particular application. Graphene oxide (GO), silk fibroin (SF) and cellulose nanocrystals (CNC) nanocomposite, also known as GO-SF-CNC composite, is a soft novel material which has a potential as protective coating of heat sink for electronics cooling applications. Typically, allowable maximum temperature of electronics is in the range of 60-70 ^{o}C. To ensure mechanical

integrity and reliability for practical applications, bionanofilms must exhibit improved mechanical behavior at different operating conditions, e.g., elevated temperatures and pressures. At the same time, creep behavior of bionanofilms is of great importance for longer time exposure to heat and/or applied load. Several researchers have worked on temperature dependent and viscoelastic behavior of individual GO, SF and CNC materials [10–13]. However, the literature is limited for temperature dependent and creep behavior GO-SF-CNC nanocomposites to ensure mechanical reliability for real life applications. To ensure long time reliability of the composite at elevated temperature, this research aims to investigate creep behavior of GO-SF-CNC composite at different temperatures.

Liquid droplets between contact surfaces makes the contact as solid-liquid contact, which can play an important role for overall reliability of the system. One of the state-of-the-art applications with solid-liquid contact is surface haptics which is gaining popularity in recent years due to their usage in devices with touchscreens. Surface haptics technology makes the touchscreen more engaging and interactive with human fingers. It involves interactions between haptic surfaces and fingertips. In order to predict better performance, all forces interacting between the two surfaces need to be accurately known. Experimental and modeling approaches have been used to understand contact behavior between the human fingertip and haptic devices. Haptic devices use electric field to sense the fingertip surface, which also can influence the contact performance. Electroadhesion is also a widely used term in this field, which is defined as the adhesion due to application of voltage on the haptic surface. At the same time, sweat, sebum etc. for finger surfaces also changes the moisture content between the two surfaces, affecting the adhesion behavior.

Literature shows that friction force between the fingertip and haptics surface increases with increasing relative humidity up to a certain limit. In this case, friction force is mostly affected due to adhesion between the two surfaces [14]. Adhesion between the surfaces largely depends on different interfacial forces. In this study, a single asperity model has been developed to predict adhesion forces between the haptics contact surfaces and the model was extended to a rough surface contact modeling to investigate interfacial forces between two surfaces with moisture content between them.

1.1. Objectives and Approach

The ultimate goal of the research is to predict optimum properties of thin films for different systems. Depending on the applications, nanomechanical properties were first determined from experiments using nanomechanical instruments and further modeling was performed to predict their behavior. Work flow of the research is shown in Figure 1. According to the figure, the research was categorized into three types of contacts for thin film systems:

1. Solid-solid contact for hard coatings: In this category, nitrogen doped diamond like carbon (NDLC)/ nitrogen doped carbon overcoat (NCOC) for HAMR system was investigated in Chapters (II-IV). In Chapter II, nanoindentation, nanoscratch and nanowear experiments were performed at different temperatures to investigate the reliability of NCOCs int terms of film thickness. Elemental analysis was also performed to investigate chemical changes before and after heat treatment for the samples. For further investigation of true mechanical properties of NDLCs and other HAMR components, finite element analysis was also coupled with

nanoindentation experiments, and results were discussed in Chapter III. In Chapter IV, the effect of carbon configuration on mechanical and tribological behavior of NDLCs were investigated using nanomechanical and nanowear measurements. Separate NDLC samples of almost the same thickness were used in this study. Elemental analysis was also performed to investigate different components the films before and after heat treatment.

2. Solid-solid contact for soft coatings: Creep behavior of GO-SF-CNC was investigated under this category in the Chapter V. The thin films were fabricated using spin assisted layer by layer (S-LbL) method on a silicon substrate. Nanoindentation creep experiments were performed on the samples using constant load and hold (CLH) method which involves holding the maximum load of nanoindentation for longer period of time. Hardness and reduced modulus of the films were determined from the experiments. FEA was incorporated in this study to investigate creep properties of the coatings at elevated temperatures.
3. Solid-liquid contacts: Surface haptics was studied under this category in Chapter VI, where the human fingertip-haptics interface behavior can be significantly affected by meniscus actions. First, mechanical and surface properties of haptics surface were determined using nanoindentations and AFM respectively. mechanical properties of human fingertip and other properties were taken from literature. Using the properties, an improved single asperity electroadhesion model was developed and extended to a rough surface contact model to predict interfacial forces between human fingertip and haptics surfaces.

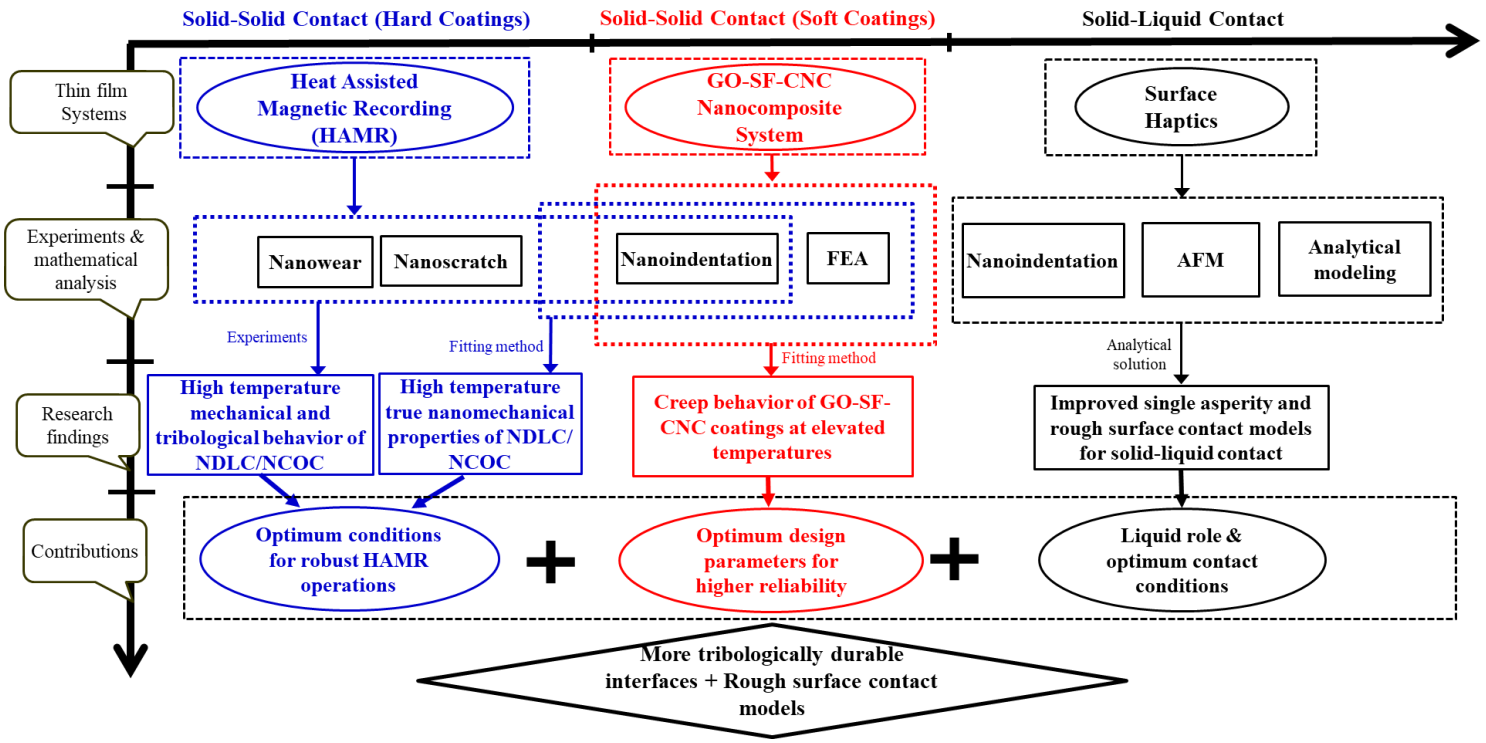

Figure 1. Flow chart of the research

CHAPTER II

HIGH-TEMPERATURE NANOMECHANICAL AND NANOTRIBOLOGICAL BEHAVIOR OF SUB- 5 NM NITROGEN-DOPED CARBON OVERCOAT FILMS

[15]1

2.1. Introduction

Diamond-like carbon (DLC) is widely used as a protective coating layer due to outstanding mechanical properties e.g., high hardness, low friction coefficient (COF), and excellent wear performance [9–11]. Depending on the application, various amorphous diamonds have been synthesized [12]. Especially in magnetic storage applications, DLC is widely used without any competitor due to its chemical inertness, smoothness with root-mean-square roughness below 1 nm [13]. Possessing high mechanical, thermal and chemical stabilities at high temperature (HT) also makes DLC a candidate for elevated temperature applications [3,14].

Nitrogen doped carbon overcoat (NCOC) is a potential protective coating due to its mechanical tribological and high temperature reliability. Different types of N-doped COC have been synthesized by different deposition techniques [15–18]. Khurshudov et al. [19] investigated the mechanical properties of thin coating films of carbon nitride and showed a considerable reduction in the COF after doping of carbon structure with nitrogen. In

[1] Reprinted with permission from "High temperature nanomechanical and nanotribological behavior of sub-5 nm nitrogen-doped carbon overcoat films." by Shakil A, Amiri A, Tang H and Polycarpou A.A. *Applied Surface Science, p.147662*. Copyright 2021 by Elsevier B.V.

sliding surfaces, doped nitrogen groups act as a lubricant, reducing the COF and subsequently enhancing the wear resistance.

Experimental results reported by Ferrari et al. [20] confirmed that the relative percentage of sp^3-hybridized carbon content in COC films show no notable change up to 10% N content. Beyond 10% N content in NCOC leads to a sharp drop in the sp^3 content, density, and hardness [21,22]. Therefore, the nitrogen content of 10% is optimum for maximizing N-associated effects on the mechanical properties, in particular COF. Although various processes have been applied to fabricate durable thin NCOC films for hard disks, the basic understanding of the chemical structure and nanoscale mechanical/wear properties at HT have not received significant attention.

In this study, HT nanomechanical and nanotribological behavior of NCOCs is investigated. NCOCs with different thicknesses are studied to investigate the dependence of mechanical behavior on coating thickness. Permanent changes in the chemical structure are traced by X-ray Photoelectron Spectroscopy (XPS). The nanomechanical and nanotribological behavior of NCOCs are compared before and after annealing to investigate the effect of heat treatment. Also, connections between chemical and mechanical changes are made.

2.2 Experimental

2.2.1. Sample description

A schematic diagram of the cross section of the samples is shown in Figure 2 (a). As shown, a FeCo based amorphous metal layer of 200 nm thickness was deposited on a glass substrate using magnetron sputtering. The metal layer represents the underlayer in a

typical magnetic storage disk. On top of the metal layer, hydrogen rich COC was deposited using plasma enhanced chemical vapor deposition. In this deposition technique, plasma is created from a hydrocarbon gas precursor by using a hot filament cathode. Then, the surface of COC was doped with nitrogen for the purpose of increasing lubricant bonding sites. Three different samples with NCOC thicknesses of 2.5, 3.5, and 4.5 nm were fabricated and referred to as NCOC-2.5, NCOC-3.5, and NCOC-4.5, respectively. The coating thicknesses were measured using ellipsometry.

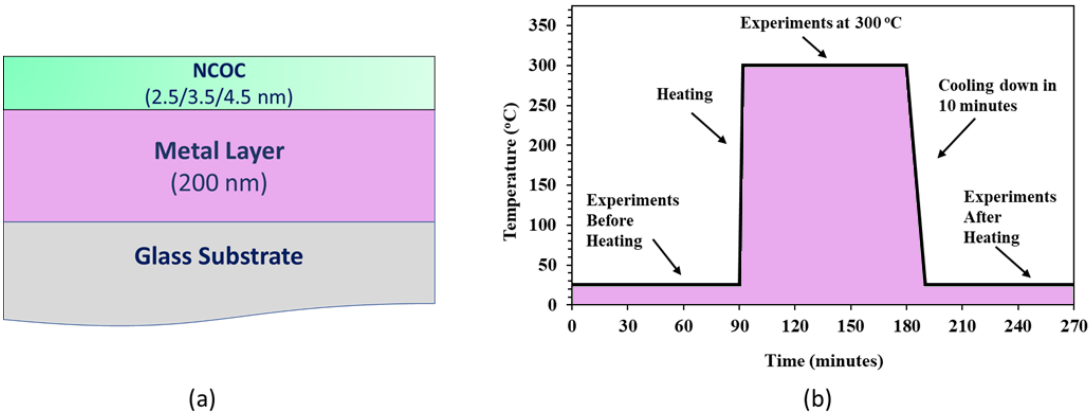

Figure 2. (a) Schematic diagram of cross-section of the samples; (b) Experimental protocol used in this study.

Literature shows that HAMR hard drives may reach up to 600 ºC with laser heating [16]. However, nanomechanical and nanotribological characterization at high temperatures using a diamond indenter has always been a challenge. Diamond indenters are not suitable for temperatures equal to or greater than 400 ºC in air environment due to rapid oxidation, which may change the topography of the indenter, thereby making the measurements unreliable [17]. Therefore, 300 ºC was chosen for elevated temperature experiments in this study. Also, multiple data are required for in-situ reliable and repeatable measurements at 300 ºC. Specifically, scratch hardness and nanowear tests require in-situ SPM

measurements by the same tip used for the experiments. Thermal drift is also a major concern that occurs due to the expansion or contraction of the sensor while in contact. The thermal drift of the transducer increases at elevated temperatures and it needs to be minimum for reliable measurements. The instrument takes some time to reduce thermal expansion. Overall, the samples were heated for a longer time than they will be subjected to real applications in their entire life. By heating for a long time, the robustness of HAMR samples can be better understood.

The NCOC samples were heat-treated in an inert environment with a heating rate of 150 ºC/min, as shown in Figure 2 (b), to reach a temperature of 300 ºC for 90 minutes, and cooled with a cooling rate of 30 ºC/min. To determine the effect of heat treatment on the chemical structure and thermal stability of N dopants, the untreated and heat-treated samples were analyzed using XPS. Due to the importance of mechanical behavior of NCOC at 300 ºC, all the nanomechanical experiments were performed at 300 ºC, before, and after heat treatment.

2.2.2. Nanomechanical experiments

Nanoindentation, nanoscratch, and nanowear experiments were performed to investigate the nanomechanical and nanotribological properties. Except temperature, all three types of nanomechanical tests were performed at the same experimental conditions, for direct comparison. A summary of the experimental conditions used in this work are shown in Table 1. Set 1 samples were subjected to mechanical tests under air at room temperature (RT) and set aside for the mechanical and elemental analyses. Set 2 were heat-treated

samples to 300 ºC and were subjected to tests at 300 ºC under argon environment (for preventing oxidation of the diamond probe).

The steady-state condition of the stage (T= 300 ºC) was maintained via heating the stage by a heater and cooling it using water to prevent overheating. The force transducer was also cooled by blowing air during the experiments. After annealing, the NCOC samples were cooled down to RT and kept in an argon environment for 30 minutes. Experiments at HT lasted for ~ 90 minutes. The same heating and cooling cycles were repeated for the preparation of Set 3 samples. Set 3 samples were mechanically tested under air atmosphere at RT to obtain mechanical attributes and nanotribological properties after heat treatment process, and were also used for elemental analysis.

Table 1. Summary of sample sets for different experimental conditions.

Sample sets	**Experimental conditions**	**Experiments performed**	**Samples tested in each set**
Set 1	25 °C Before heating	Nanomechanical tests and elemental analysis	NCOC-2.5 NCOC-3.5 NCOC-4.5
Set 2	300 °C	Nanomechanical tests	
Set 3	25 °C After heating	Nanomechanical tests and elemental analysis	

2.2.3. Characterization and instrumentation

Nanomechanical property measurements were performed using a Bruker TI Premier instrument. The instrument was equipped with an HT stage to test samples up to 800 °C. Nanoindentation tests were performed at very shallow depths for the determination of the reduced modulus and hardness of the samples. Both nanotribological and nanomechanical

properties were also obtained via nanoscratch. An Omicron XPS system with an Mg X-ray source was used to acquire the XPS spectra. Sample charging was minimized by installing a CN-10 charge neutralizer.

2.2.4. Data collection and processing

2.2.4.1. Nanoindentation

In a typical nanoindentation experiment, a preload of 2 μN through a trapezoidal load function was applied to the samples to ensure initial contact. The load function shown in Figure 3(a) involves several steps: loading linearly to the maximum load in 5 seconds, holding the sample to maximum load for 2 seconds to reduce creep effects, and unloading linearly to the initial load in 5 seconds. A cube corner indenter with a tip radius of 72 nm was employed for shallow indentations. Multiple nanoindentation experiments were performed using 11, 13, 15, and 17 μN peak loads. The Oliver and Pharr method was used to extract the reduced modulus only [18].

The contact depth (h_c) of nanoindentation is obtained by equation 1.

$$h_c = h_{max} - \varepsilon \frac{P_{max}}{S} \quad (1)$$

where P_{max}, h_{max}, and S are maximum load, maximum displacement, and the initial slope of the unloading curve, respectively. For cube corner and Berkovich indenters, $\varepsilon = 0.72$. The contact area (A_c) was calculated from h_c using a predetermined area calibration on a standard fused quartz sample. Hardness and reduced modulus are calculated using equations 2 and 3, respectively:

$$H = \frac{P_{max}}{A_c} \tag{2}$$

$$E_r = \frac{\sqrt{\pi} S}{2\beta\sqrt{A_c}} \tag{3}$$

In equation. 3, β = 1. In this study, only E_r was calculated using Oliver-Pharr method for a contact depth range of 1.8-4.2 nm. The tip areal function for nanoindentation experiments was determined using a fused quartz standard sample, and used for E_r calculations at room temperature before and after heating. High temperature nanoindentations in this study were performed at 300 ^oC in argon environment, which is lower than the oxidation (decomposition) temperature of diamond tip (400 °C) in air atmosphere [17]. In another study, the thermogravimetric analysis (TGA) results reported by Pu et. al. [19] clearly showed that the oxidization of the purely sp^3-diamond crystal begins at temperature > 674 °C. Therefore, the experimental conditions lead to no changes in the tip topography and the same tip areal function at room temperature was also used in this study for high temperature measurements.

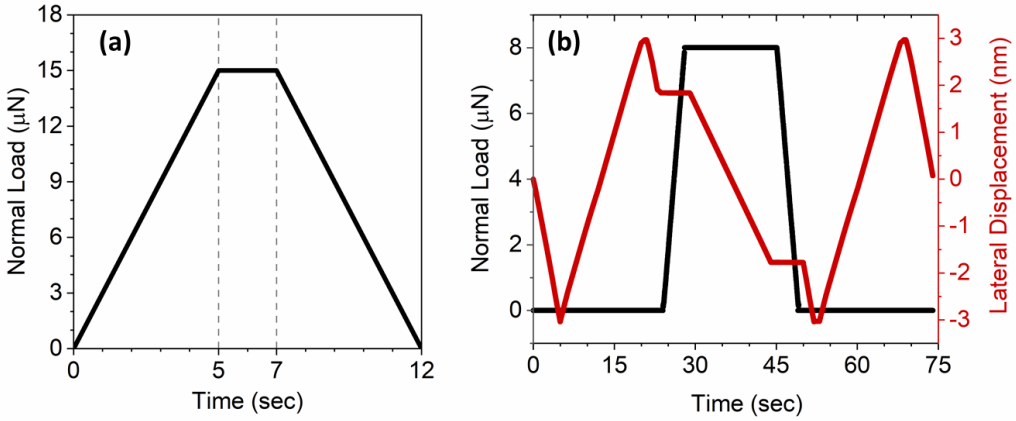

Figure 3. Load functions for (a) nanoindentation and (b) nanoscratch experiments

2.2.4.2. Nanoscratch

To obtain reliable measurements using nanoindentation, the indentation depth must not exceed 10-20% of the film thickness. For sub-20 nm thin films, it is very difficult to measure reliable mechanical properties using nanoindentation due to tip blunting, instrument limitations and surface roughness. For these reasons, hardness of thin films using nanoindentation were not reported in this study. On the other hand, nanoscratch overcomes some of the difficulties by considering normal force, lateral force and residual cross sectional area of the scratched region, minimizing substrate effects [20]. Nanoscratch can be performed deeper, up to 35% of the film thickness without any substrate effect [21].

In this study, nanoscratch experiments were performed to measure the scratch hardness and COF. To ensure correct mechanical property measurements, a sharp cube corner tip of radius 76 nm was used to obtain shallow scratches (and ensuring only the spherical tip was engaged during scratch). The substrate effect was reduced by selecting the sharp tip and consequently low loads during nanomechanical measurements at HT. Scratch experiments were performed as follows (Figure 3(b)):

1. Pre-scan the surface for 6 μm length with a minimal preload of 2 μN to identify any surface tilt correction during scratch;
2. Traverse the surface with the maximum scratch load for a length of 4 μm; and
3. Post-scan the surface for 6 μm length and 2 μN to measure the residual depth.

A maximum scratch load of 8 μN was applied at RT for Set 1 and Set 3 samples. The load was reduced to 6 μN at 300 ºC (Set 2) to minimalize plastic deformation effects. In-situ

normal and lateral forces, residual depths and COF were measured during the scratch. A 4x4 μm^2 scan of the surface (using the same tip) was performed to image the residual surface profile after scratch.

Tayebi et al. [20] proposed a model that relates hardness (*H*) and surface traction (*s*) of a material to the normal force (*N*) and lateral force (*F*) during scratch. That is:

$$\begin{cases} F = Hr^2\left[\alpha - \sin\alpha\cos\alpha\right] + 2sr^2\left[\int_0^{\frac{\pi}{2}}\int_0^{\alpha} \sin\zeta\sqrt{\sin^2\xi + \cos^2\xi\cos^2\zeta}\, d\zeta d\xi\right] \\ N = \frac{\pi}{2}Hr^2\sin^2\alpha - sr^2\left\{\sin\alpha - \cos^2\alpha\ln\left(\sec\alpha + \tan\alpha\right)\right\} \end{cases} \quad (4)$$

where α is the angle of first contact between the indenter and the material under sliding, and it is related to the indenter tip radius (*r*) and in-situ contact width (*w*) by equation 5.

$$\alpha = \sin^{-1}\left(\frac{w}{2r}\right) \quad (5)$$

The in-situ profile was determined by superimposing the residual profile taken after the scratch and elastic recovery profile of the surface using Boussinesq theory of potentials.

Tayebi's model was originally derived from Goddard's scratch model where scratch hardness was calculated using average flow pressure on a spherical indenter, lateral force and friction coefficient. Tayebi's model includes tangential shear stress components during scratch and elastic recovery of the material. The model has been compared with other scratch models and FEA to calculate hardness of bulk materials [20,22] and it has also been used to calculate hardness of thin films [21]. However, for elastic recovery calculations, elastic modulus of the material needs to be used which can be obtained from

other techniques such as nanoindentation. Therefore, nanoindentation experiments have been performed and reduced moduli have been reported from nanoindentations in this study.

2.3. Results and discussion

2.3.1. Elemental XPS analysis

Elemental analysis was performed to determine changes in the chemical structure of NCOC samples after heat treatment. Figure A1 of Appendix A and Table 2 show the survey spectra of NCOC samples and the chemical composition of the samples evaluated by XPS. The chemical composition after annealing shows ~ 4% drop, which is related to the evaporation of absorbed water. In addition, the N content showed no conspicuous change after heat treatment.

Table 2. Sample chemical composition evaluated by XPS (BHT/AHT=Before/After heat treatment).

Sample	C (At%)	N (At%)	O (At%)	sp^3 Carbon content	sp^2 Carbon content	Pyridinic N (At%)	Pyrrolic N At%)	Graphitic N (At%)	Oxidized N (At%)
NCOC-2.5 (BHT)	79.12±0.1	9.95±0.1	10.93±0.1	89.11	10.89	7.47	57.72	22.67	12.14
NCOC-2.5 (AHT)	83.96±0.1	9.63±0.1	6.41±0.1	80.63	19.37	2.12	51.36	37.99	8.53
NCOC-3.5 (AHT)	83.77±0.1	9.56±0.1	6.67±0.1	84.54	15.46	2.74	50.23	41.19	5.85
NCOC-4.5 (AHT)	84.91±0.1	8.76±0.1	6.32±0.1	83.77	16.23	4.48	46.62	44.21	4.89

High resolution XPS spectra were also collected to study the terminal groups in detail. Figure 4 (a) and 4 (b) depict the C 1s XPS spectrum of NCOC-2.5 sample before and after heat

treatment, respectively. The high-resolution C 1s spectra of both samples include four peaks by curve fitting. The peaks at ~ 284.0, 284.9, 286.1, and 287.9 eV were attributed to the C=C, C-C, C-N/C-O, and C=O bonds, respectively [23]. The C 1s bond showed an obvious sharp peak at 284.9, corresponding to sp^3 hybridized carbon, which was less-intensified after heat treatment, as shown in Table 2. This phenomenon confirmed the partial conversion of sp^3- to sp^2-hybridized carbons after heat treatment at 300 ºC (implying partial graphitization). The ratio of sp^2/sp^3 carbon changed from 12% in 2.5 NCOC (before heating) to 24% in NCOC-2.5 (after heating). This ratio shows almost the same enhancement in the samples with different thicknesses, after heat treatment (Figure 4 (c) and 4 (d)). It verifies that the chemical composition of NCOC is not a function of thickness up to 4.5 nm.

The growth of the sp^2/sp^3-hybridized carbon ratio makes the structure softer [24]**.** Growth of sp^2/sp^3-hybridized carbon ratio is in good agreement with the reduction of oxygen content. As shown in Figure A1 and Table 2, a small fraction of oxygen-containing groups on NCOC surface was decomposed during the annealing procedure, converting some of the sp^3 hybridized carbons to sp^2 or remaining some holes instead. Both possible phenomena may result in a softer material.

The chemical configuration of N dopants was also evaluated via analyzing high resolution N 1s spectrum of NCOC. There are three common N configurations in carbon structures: pyridinic N, pyrrolic N, and graphitic N. The N 1s spectra are represented in Figure 4 (e-h). They were deconvoluted into four peaks with binding energies of 397.1, 398.8, 400.4, and 402.2 eV, attributed to the pyridinic N, pyrrolic N, graphitic N, and oxidized N, respectively [25–29]. While the atomic percentage of N remained constant during the heat treatment

procedure (Table 2, Figure 4 (e) and 4 (f)), the configuration of N atoms was altered. Upon heat treatment, an increase in the sp^2-hybridized nitrogen (graphitic N and pyridinic N) or a drop in the sp^3-hybridized nitrogen (pyrrolic N) was obtained, confirming a shift from low-stable to high-stable configuration. Similar to the carbon structural change, converting sp^3- to sp^2-hybridized nitrogen may play a role in making the material softer.

The results in Table 2 confirmed that the percentage of pyrrolic N reduced from 57.72 to 51.36 after heat treatment. On the other hand, graphitic N content increased by 6.7%, which indicates a chemically stable and softer. These values were consistent for samples of different thicknesses (Figure 4 (e-h)). Despite the presence of relatively low alteration, the chemical structure results confirmed the gradual softening of NCOC structure after heat treatment at 300 ºC.

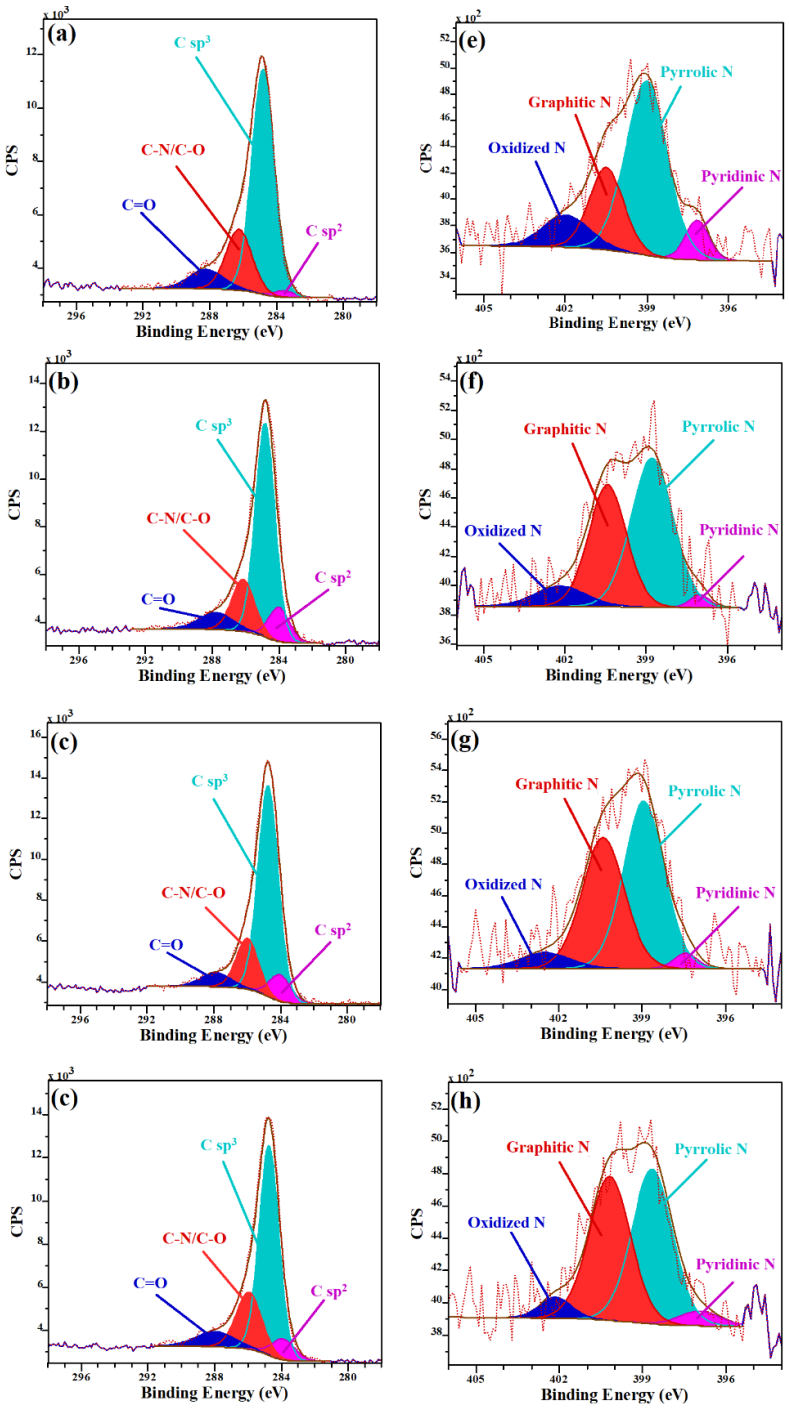

Figure 4. C 1s XPS spectra of **(a)** NCOC-2.5 (BHT); **(b)** NCOC-2.5 (AHT); **(c)** NCOC-3.5 (AHT); and **(d)** NCOC-4.5 (AHT). N 1s XPS spectra of **(e)** NCOC-2.5 (BHT); **(f)** NCOC-2.5 (AHT); **(g)** NCOC-3.5 (AHT); and **(h)** NCOC-4.5 (AHT). BHT/AHT=Before/After heat treatment.

2.3.2. Nanomechanical analysis

2.3.2.1. Nanoindentation experiments

Figure 5(a), 5(b), and 5(c) depict the load–displacement curves of NCOC samples for the three experimental sets. All the tests were performed with a peak load of 15 μN. The load–displacement curves showed a right shift with increasing temperature and/or with annealing. The maximum indentation depth decreased with thickness and increased with temperature. For example, at 300 °C, NCOC-2.5 sample experienced a maximum penetration depth of 4.6 nm, whereas for NCOC-4.5 it was 4 nm.

As discussed earlier, nanoscratch experiments offer less underlayer effect, compared to nanoindentation, and therefore nanoscratch hardness values were extracted and reported in this study. To calculate the nanoscratch hardness, the reduced modulus of the samples is required, which were obtained from nanoindentation experiments, Figure 5(d). Despite no clear trend for the reduced modulus as a function of thickness, the range of average reduced modulus for the NCOC samples dropped from 170-185 GPa to 170-173 GPa after heating, implying the presence of a few percentage of permanent deformation (sp^3 -to sp^2) after each heating-cooling cycle.

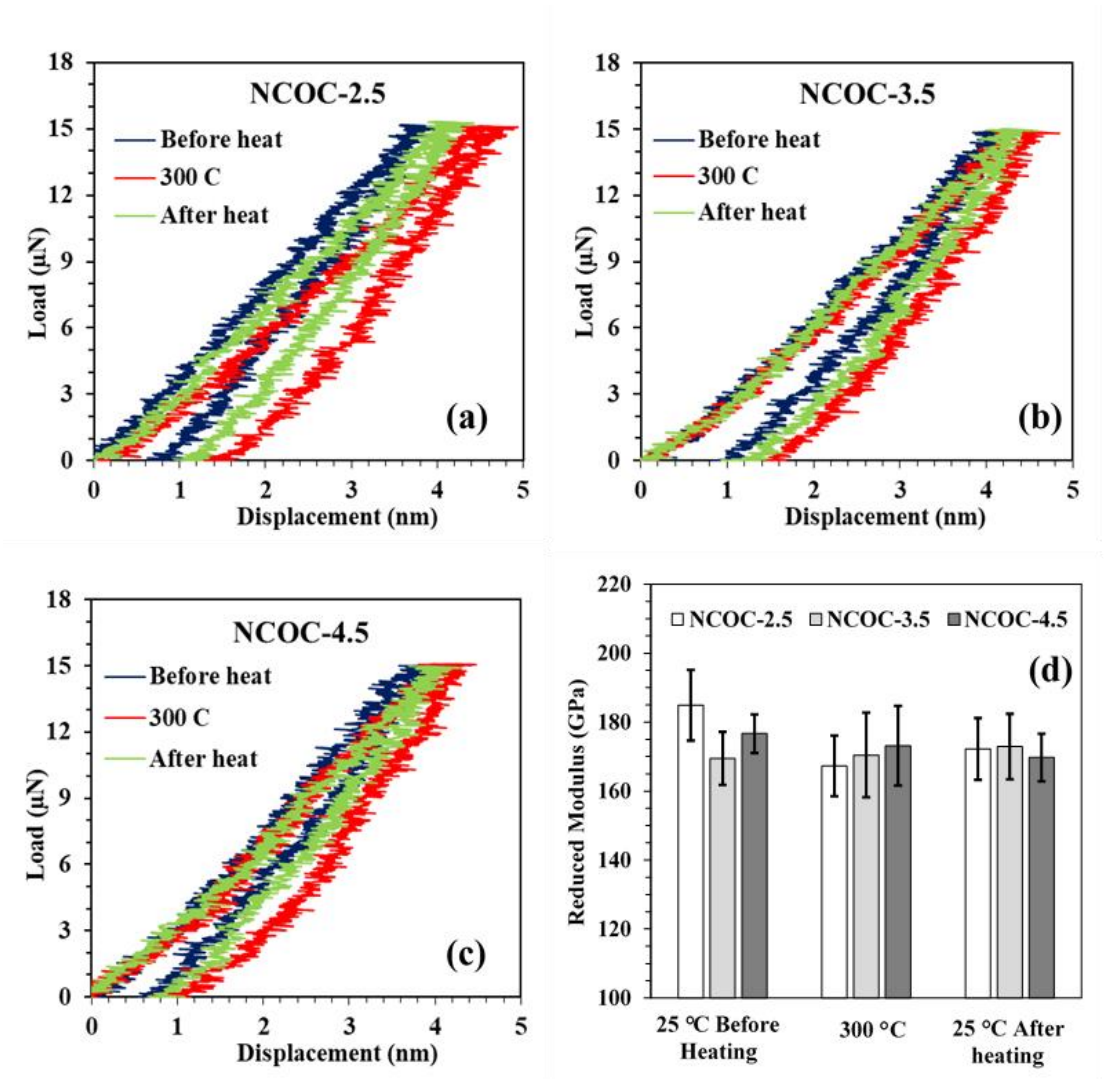

Figure 5. Nanoindentation load-displacement curves of (a) NCOC-2.5; (b) NCOC-3.5; and (c) NCOC-4.5 before heating, at 300 ºC, and after heating. (d) Reduced modulus values obtained from nanoindentation. Error bars designate ± one standard deviation.

2.3.2.2. Nanoscratch experiments

Figure 6 depicts scanning probe microscopy images and associated height profiles with each panel at the maximum-load points for NCOC samples at 25 °C (before heating), 300 °C and 25 °C (after heating). Upon exposure to the load scratch experiments, a groove

formed via the plowing probe on the NCOC samples. The formed grooves offer visual characterization as well as comparison of the wear. As shown in Figure 6, before heating, the NCOC films of different thicknesses demonstrated faint scratch marks and trivial wear near the peak load. On the other hand, the scratch mark becomes clear and deeper with increasing temperature to 300 °C. After heat treatment procedure and cooling at RT, all NCOC samples featured faint scratch marks again, but slightly deeper than those of NCOC samples before heat treatment. It is attributed to the softening of NCOC after heat treatment, which is in agreement with the growth of the sp^2/sp^3 ratio of both carbon and nitrogen elements after heat treatment.

2.3.2.2.1. Nanoscratch hardness

Table 3 lists the different measured contact parameters to calculate scratch hardness under different experimental conditions. Figure 7 shows a summary of the scratch hardness for NCOC samples at different thickness and operating conditions. The scratch hardness of all samples was about 23 GPa at RT before heat treatment, which are higher than scratch hardness of carbon overcoats without nitrogen doping reported in the literature [5,21]. This indicates that nitrogen doping enhances the mechanical properties of the NCOC samples. As the temperature increases to 300 °C, the scratch hardness associated with all NCOC samples decreased because of deeper scratch and larger contact area. The percentage of reduction in the scratch hardness was lower for samples with higher thickness of NCOC. After the heat treatment process, the scratch hardness of the NCOC-

3.5 and NCOC-4.5 samples recovered almost entirely. These small drops can be attributed to the graphitization and changes in the configuration of the N atoms.

On the other hand, the hardness value for NCOC-2.5 sample changed from 22.68 GPa before heat treatment to 20.64 GPa after heating, representing ~ 9% reduction after each heating-cooling cycle. While the chemical structure is the same for samples with different thicknesses, they showed different mechanical behavior when experiencing annealing. It can be concluded that 3.5 nm is a critical minimum thickness for NCOC samples to be used in HAMR.

The in-situ contact depths during scratch experiments for all experimental conditions, as shown in Table 3, are more than 35% of the film thicknesses, even though a very sharp indenter and very low load have been used. This implies that it is very difficult to determine the nanomechanical properties sub-5 nm thin films from experiments only without any underlayer effect. However, the residual depths of scratch for all NCOC samples and experimental conditions are much lower than 35% of the film thickness, which indicates that the experimental approaches in this study can be used for reliable measurements of NCOC samples with reduced underlayer effect.

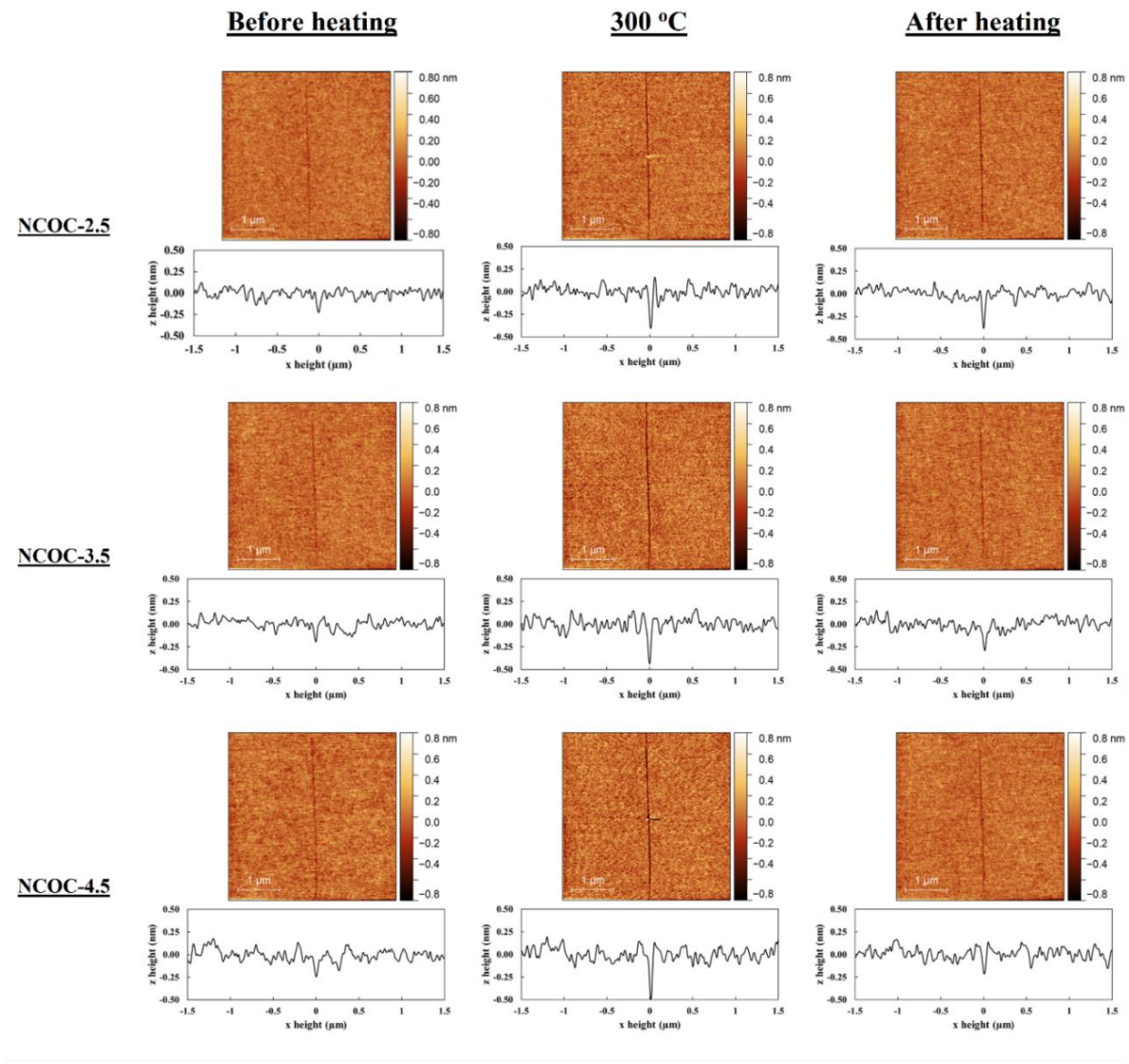

Figure 6. Scanning probe microscopy images and cross-sectional profiles of NCOC before heating (25 °C), at 300 °C and after heating and cooling to 25 °C. The scratch lines are located at the center of the scanned areas, from top to bottom. All images have the same scan size of 4 µm. Scale bars are 1 µm.

Table 3. Contact parameters from nanoscratch experiments. BHT/AHT=Before/After heat treatment.

Samples	Conditions	Normal force (μN)	Lateral force (μN)	Residual depth (nm)	In-situ contact width (nm)	In-situ contact depth (nm)	Hardness (GPa)
NCOC-2.5	**BHT**	8.07	0.88	0.22	30.00	1.49	22.68
	300 ºC	5.98	1.42	0.45	31.00	1.60	16.05
	AHT	8.03	1.81	0.38	33.50	1.87	20.64
NCOC-3.5	**BHT**	8.06	0.96	0.20	30.00	1.49	22.68
	300 ºC	6.00	1.19	0.44	29.50	1.45	17.74
	AHT	8.03	1.65	0.29	30.50	1.55	22.64
NCOC-4.5	**BHT**	7.97	1.52	0.20	29.50	1.45	23.01
	300 ºC	6.05	1.07	0.49	28.00	1.30	18.94
	AHT	8.06	1.96	0.22	30.00	1.49	22.66

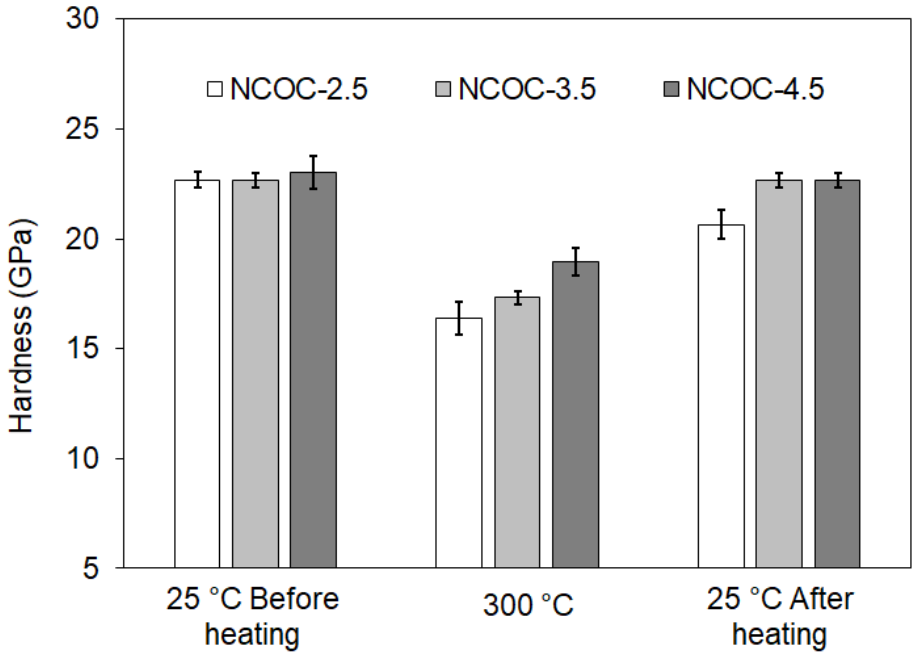

Figure 7. Scratch hardness of NCOC samples. Error bars designate ± one standard deviation.

2.3.2.2.2. Coefficient of friction

It has been shown by several researchers [30,31] that the COF of amorphous carbon structure can be greatly reduced by nitrogen doping or functionalization with amine-based groups. In sliding surfaces, nitrogen groups, in particular, pyridinic N and pyrrolic N as the planar terminal groups, act as a lubricant, resulting in lower COF. Figure 8 shows the variation of the average COF with temperature and thickness for the NCOC samples after reaching steady-state values. The COF for NCOC samples before heating was in the range of 0.15-0.19 at 25 °C. The obtained range is in good agreement with recently reported experimental data for COFs of thin COC films [5,32,33]. On average, the COFs of NCOC samples with various thicknesses increased more than 100 % with increasing temperature from 25 °C to 300 °C, reaching values in the range of 0.38-0.42. High standard deviations were evident at 300 °C due to the use of low normal load with a sharp indenter.

The softening behavior of NCOC permitted deeper scratches to take place even at lower loads of 6 μN. Similar results were obtained for COC samples with no dopants [5]. After a cycle involving a heating process to 300 °C and cooling back to 25 °C, the COF increased from 0.16 to 0.18 for NCOC-2.5, from 0.15 to 0.18 for NCOC-3.5, and from 0.19 to 0.21 for NCOC-4.5. These results are in good agreement with the XPS results (growth of the sp^2/sp^3 ratio) as well as the experimental data reported by Cui et al. [34]. They concluded that a higher degree of graphitization results in higher COF values. All NCOC samples

showed no specific trend of COF as a function of thickness at 25 °C before heating, 300 °C and 25 °C after heating.

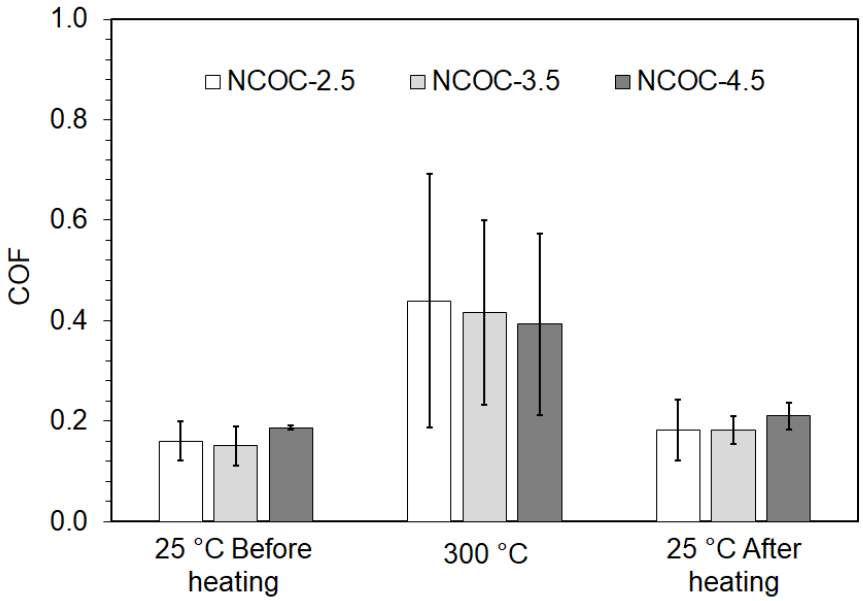

Figure 8. Average COFs for NCOC samples as a function of temperature and film thickness. Error bars designate ± one standard deviation.

Increase in COF is significant at 300 °C. Bowden and Tabor [35] proposed a simple theory to interpret the friction behavior of sliding surfaces. In this theory, two separate terms of adhesive and deformation friction are considered as main independent mechanisms. The adhesive COF is due to van der Waals interactions. Local mechanical properties of sliding surfaces e.g., elastic/plastic properties, surface roughness, and interface surface energy are all effective parameters to define van der Waals interactions [36]. The deformation COF is due to resistance to plowing the asperities of the softer surface through the harder surface. Although softening phenomena at HT can facilitate the deformation friction mechanism, the dominant mechanism for the sharp augmentation of the COF at 300 °C is adhesive friction [5].

Consistent with our recent results, it can be concluded that sp^2 – hybridized (unsaturated) carbon and nitrogen atoms in the NCOC films may undergo chemical reactions, inferring greater adhesion between the NCOC film and the diamond tip, therefore increasing friction [37].

In addition, the drop in the structural hydrogen atoms causes more sp^2 – hybridized carbon and N atoms on the surface. At 300 °C, due to more sp^2 – hybridized active sites on the surface and the presence of sufficient energy for covalent bonding, the COF intensified. After cooling, the above-mentioned reason became passive, as indicated by the XPS results. The enhancement of the sp^2/sp^3-hybridized carbon ratio after heat treatment double-confirms the accuracy of results with molecular dynamics [37].

2.3.2.3. Nanowear experiments

In order to measure the nanowear resistance of thin films such as COC, nanowear experiments are widely used [32,38]. To this end, a diamond indenter is used to scratch and form a rectangular area on the surface of the sample with a fixed normal load. After the wear experiment, a larger area involving the worn region is rescanned with the same indenter via applying a minimal contact force of 2 μN. Chatterjee et al. [39] performed surface displacement analysis of scratch using FEA, showing that after elastic recovery, the residual scratch groove is shallower than in-situ scratch groove, which can be easily traced by the same indenter. Scanning the surface with the same indenter right after the wear test also allows to obtain the worn surface topography under the same temperature and environmental conditions. It allows to scan the surface especially for high temperature

tests in inert environments. Using minimal contact force for rescanning reduces the possibility of additional material removal from the worn area and surface profile of the worn area can be reliably obtained. Similar approaches have been used elsewhere [5,40,41]. After rescanning the surface, the mean heights of both worn and unworn areas were calculated. A Berkovich indenter with a tip radius of 270 nm was used for the nanowear experiments. A normal load of 30 μN was applied and the surface scan was 2 μm by 1 μm area. After the wear experiments, the residual surface of the worn area was scanned using the same probe with 2 μN load on a 3.8 μm by 3.8 μm area. Wear depths were calculated by comparing the average surface height of the worn area with the average surface height of the unworn area. Figure 9 shows residual scanning probe microscopy images for the NCOC samples after the nanowear experiments. The z-axis was scaled automatically and represents the minimum and maximum height values.

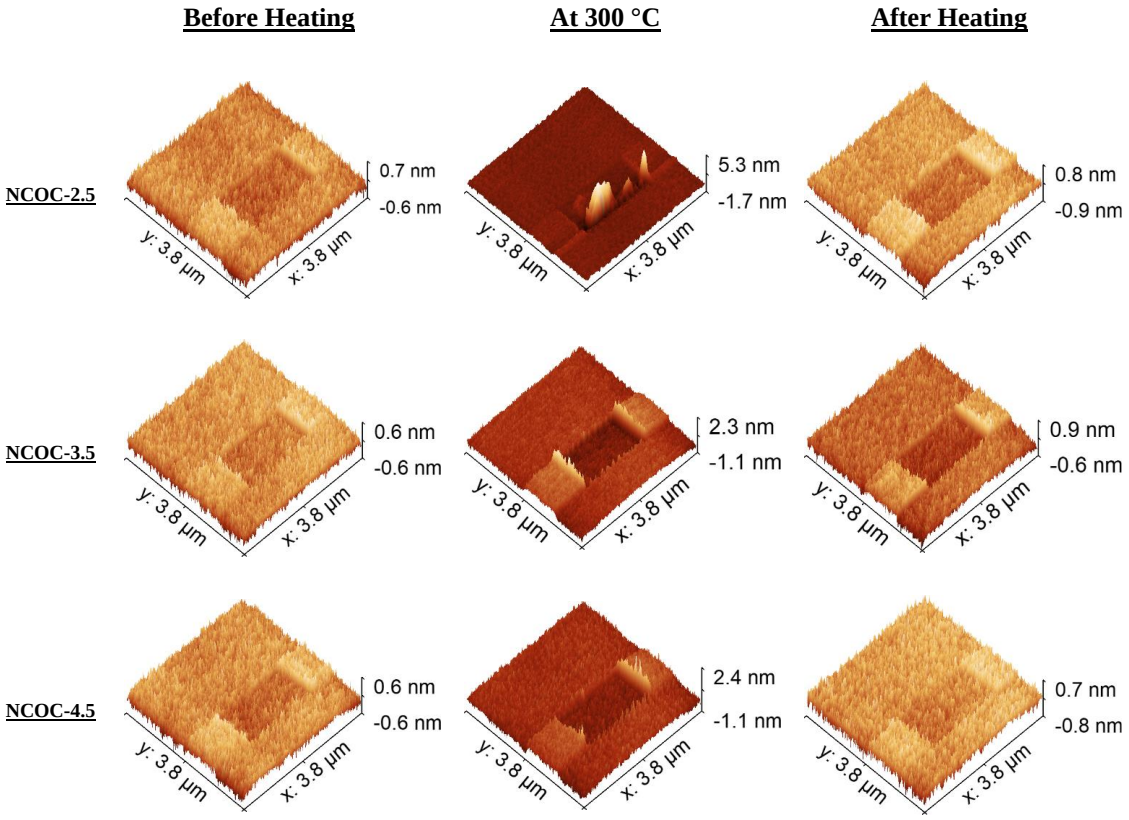

Figure 9. Residual surface scans of NCOC samples after nanowear experiments: before heating (at 25 °C), at 300 °C and after heating (at 25 °C).

The wear tracks showed a maximum depth of 0.6 nm for all three samples, NCOC-2.5, NCOC-3.5, and NCOC-4.5, before heating. These values increased to 1.7 nm, 1.1 nm, and 1.1 nm at 300 °C, respectively. Beside higher wear within the worn region, the existence of material pile-up at the border is also seen, implying a more intense material removal process. At 300 °C, NCOC-2.5 film was abruptly worn out and the majority of the produced wear-track was associated with a very high pile up due to the irregular removal of the coating (catastrophic NCOC damage). After the heat treatment process and cooling,

the NCOC films show significant but not full recovery, exhibiting higher wear (permanent damage), compared to the initial state before heating.

As discussed above, increasing the atomic percentage of sp^2-hybridized carbon and nitrogen atoms after heat treatment is the main reason for softening the NCOC structure. All the images in Figure 9 represent some extent of material pile-up. As can be seen, the height of the pile-up is a function of temperature and thickness of the NCOC layers. As the temperature increased, greater wear was measured. Furthermore, as the thickness of NCOC increased, the height of the pile-up decreased.

Figure 10 depicts the average wear depth for NCOC samples of different thicknesses along the scanning direction at three conditions: before heat treatment at RT, at 300 °C, and after heat treatment. Interestingly, the NCOC samples show average wear depth values in the range of 0.21-0.25 nm under normal working conditions (before heating at 25 °C). It confirms the promising durability and protective attributes of NCOC under nominal operating conditions. Therefore, abrasion resistance of NCOC samples with thickness of 2.5, 3.5 and 4.5 nm is excellent, and thus able to protect the magnetic disks from scratch initiated by contacting the recording head on the disk surface. The average wear depth increased with temperature to 0.9 nm for NCOC-2.5, 0.81 nm for NCOC-3.5, and 0.64 nm for NCOC-4.5 at 300 °C. The average wear depth showed significant drop with thickness at HT. This could be attributed to increase of hardness with NCOC thicknesses at 300 °C. Higher hardness indicates lesser permanent deformation of the coating. Therefore, NCOC-4.5 represents the least permanent deformation during the wear experiments, leading to lower wear than the thinner NCOC samples, at extreme temperature conditions.

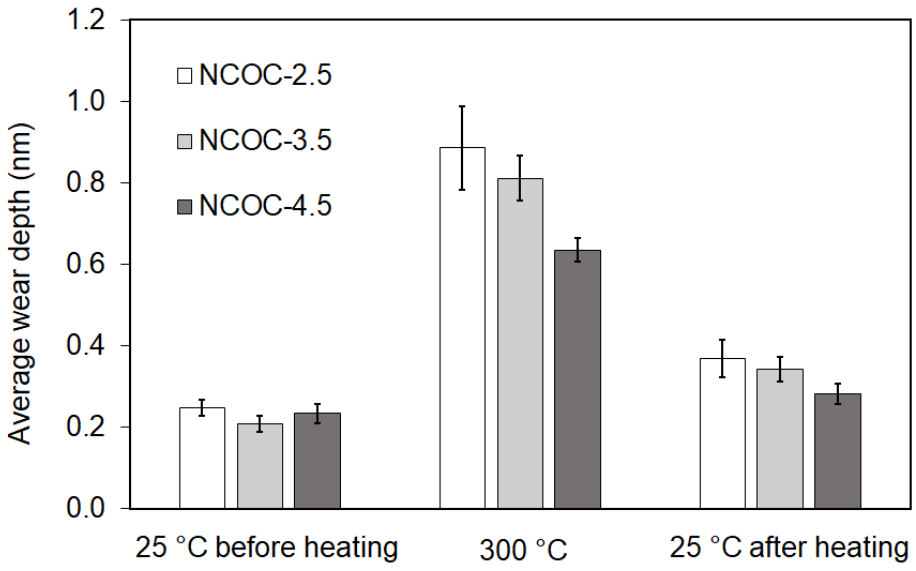

Figure 10. Average wear depth of NCOC samples. Error bars designate ± one standard deviation.

Overall, the outstanding nanotribological properties of NCOC samples are degraded with temperature due to the decrease of sp^3 content and subsequently increased adhesion, in agreement with Rose et al. [42], and XPS results. After heat treatment, the NCOC samples with different thickness showed an average wear depth of < 0.38 nm, implying few percent of irreversible degradation and permanent changes in the chemical structure. It is noteworthy that the percentage of permanent change in the NCOC samples were significantly less than that of COC counterparts without nitrogen dopants, as presented in our earlier study [5]. Wear depths of NCOCs at room temperature were also found less than wear depths of sub-5nm diamond like carbon without nitrogen doping, as reported in literature [21,40]. Also, the average wear depth showed a reduction with COC thickness, which is explainable by considering the small increase in the sp^2/sp^3 ratio and change in hardness after heat treatment.

2.4. Summary

The nanotribological properties of nitrogen-doped COC films with different thicknesses were studied experimentally through nanoscratch and nanowear experiments. Hardness, COF, reduced modulus of elasticity, scratch and wear depths were measured and used as mechanical metrics. As chemical metrics, changes in the sp^2/sp^3 ratio of carbon and nitrogen elements were analyzed by XPS. Based on the results, the following conclusions could be drawn:

(1) Nanoscratch experiments show that the COF of NCOC samples is a strong function of temperature and less dependent on NCOC thickness. The COF increases more than 100% at 300 ºC for all samples;

(2) NCOC samples with thicknesses of 3.5 nm and 4.5 nm exhibited stable mechanical and chemical stabilities. In addition to excellent mechanical properties, the heating effects on changing the chemical and mechanical stabilities of NCOC is reduced in the presence of N dopants. A comparison of the results presented in this study and our recent study on COC (without N dopants) [5] confirms the positive effect of N dopants on reducing wear;

(3) Through nanowear experiments, the wear track depth of the NCOC film increases dramatically with increasing temperature from 25 ºC to 300 ºC. XPS results revealed that the increase in the sp^2/sp^3 ratio of C and N in inert environment at HT is the main reason for the wear rate changes. Increasing thickness of the film showed significant drop on the wear at 300 ºC as well as after heat treatment; and

(4) XPS results confirmed that graphitization is an integral part of annealing process at 300 ºC. The structural conversion (sp^3-to sp^2-configuration) offers a mechanism to explain the deterioration of the wear resistance (softening).

In this chapter, nanoindentation and nanoscratch experiments were performed to obtain mechanical properties of NCOCs. However, due to instrument limitations and very thin films, obtaining true mechanical properties of NCOCs from pure experiments was very challenging without any substrate effect. Finite element is one of the tools that can be integrated with the experimental results to determine true mechanical properties without any substrate effect. In Chapter III, nanoindentation experiments were coupled with finite element modeling using modified indenter geometry and true mechanical properties of NCOCs were determined.

CHAPTER III

HIGH TEMPERATURE NANOMECHANICAL PROPERTIES OF SUB-5 NM NITROGEN DOPED DIAMOND-LIKE CARBON USING NANOINDENTATION AND FINITE ELEMENT ANALYSIS [43][2]

3.1. Introduction

Recently, nitrogen doped diamond like carbon (NDLC), also known as NCOC, has caught much attention in magnetic storage research. In the previous chapter, it was shown that nitrogen doping improves mechanical and wear performance of ultra-thin sub-5 nm NDLC even at high temperature conditions, compared to DLC without nitrogen doping [47]. To ensure the robustness of the HAMR media, mechanical properties of ultra-thin sub 5-nm NDLC coatings are of great interest. It is very challenging to accurately measure sub-5 nm NDLC films and other HAMR components from experiments without substrate effects.

Nanoindentation is a popular technique to measure nanomechanical properties of thin films. However, for sub 20-nm films, the nanoindentation technique faces several challenges. A rule-of-thumb is that for reliable measurements of thin films with minimal substrate effect, the maximum penetration depth of indentation must be within 10-20% of the film thickness, which is very difficult for sub-20 nm films. Due to instrument

[2] Reprinted with permission from "High temperature nanomechanical properties of sub-5 nm nitrogen doped diamond-like carbon using nanoindentation and finite element analysis." by Shakil A and Polycarpou A.A. *Journal of Applied Physics, 129(13), p.135302*. Copyright 2021 by American Institute of Physics.

limitations, indenter bluntness and roughness of the samples, it becomes very difficult to reliably measure mechanical properties of sub-20 nm films without any substrate effect [26].

Nanoscratch is another technique that overcomes some of the indentation difficulties. For nanoscratch, the maximum scratch depth must be less than 35% of the film thickness for mechanical property measurements without significant substrate effect [27]. However, nanoscratch also has limitations for ultra-thin films. For sub 5-nm NDLC films, it is almost impossible to determine their mechanical properties without any substrate effect from experiments only.

Finite element analysis (FEA) has been frequently used with nanoindentation to predict nanomechanical properties of thin films without substrate effect. In this case, FEA simulations are performed with varying mechanical properties of the material in order to correlate with experimental nanoindentation responses. Bhattacharia and Nix [48] first introduced FEA to determine the nanomechanical properties of bulk material from sub-micrometer indentations. Since then, numerous researchers have been using FEA to predict mechanical properties of thin films. Lichinchi et al. [49] performed nanoindentation experiments and compared the responses with FEA to obtain yield strength of TiN and high-speed steel. They also compared the experimental results with a 3D model and a 2D conical model and found that the 2D model showed similar results as the 3D model. Yu et al. [50] introduced the roundness of a cube corner indenter in their FEA model to obtain nanomechanical properties of bilayer samples with sub-50 nm thin coatings. Zhang et al. [51] showed that for mechanical properties of sub-20 nm thin films,

assuming perfect spherical shape at the end of the indenter does not give accurate predictions. They introduced a truncated sphere shape at the very end of the indenter so that there was a flat surface contact at zero contact depth. The model has been successfully used to determine nanomechanical properties of different layers of magnetic storage samples.

In this study, nanoindentation experiments were performed at different contact depths under different temperature conditions and FEA was performed using the truncated sphere model from Zhang et al. [51] in order to measure the mechanical properties of different thin layered HAMR media components, especially sub-5 nm thicknesses NDLC films without any substrate effect. After obtaining the Elastic Modulus (*E*) and Yield strength (*Y*) of the NDLC films from FEA, the results were compared with scratch hardness (*H*) data from a previous study to investigate the *H/Y* ratio for NDLC films at different experimental conditions.

3.2. Experimental

3.2.1. Sample description

Figure 11(a) shows the schematic diagram of a HAMR sample with different layers. The bottom layer in Fig 1(a) is the glass substrate with a glass transition temperature (T_g) of 691 ^oC, which was provided by the vendor. On top of the glass substrate is the FeCo metal layer which is used as underlayer in a typical HAMR media. The metal layer has a thickness of 200 nm which was deposited by magnetron sputtering. The topmost layer shown is the NDLC coating, which was also termed as nitrogen doped carbon overcoat in other studies [15]. At first, the DLC was deposited on top of the metal layer by plasma

enhanced chemical vapor deposition technique. After that, nitrogen was doped on top of the DLC film to increase lubricating bonding sites. In this study, NDLC films of 3.5 nm and 4.5 nm were deposited and termed as NDLC-3.5 and NDLC-4.5 respectively. Another 2.1 nm NDLC was deposited on top of the metal layer, and the sample was used to measure the mechanical properties of the metal layer at different temperatures. Thicknesses of the coating were measured using optical ellipsometry. To determine the mechanical properties of the glass substrate, a bare glass sample was also used.

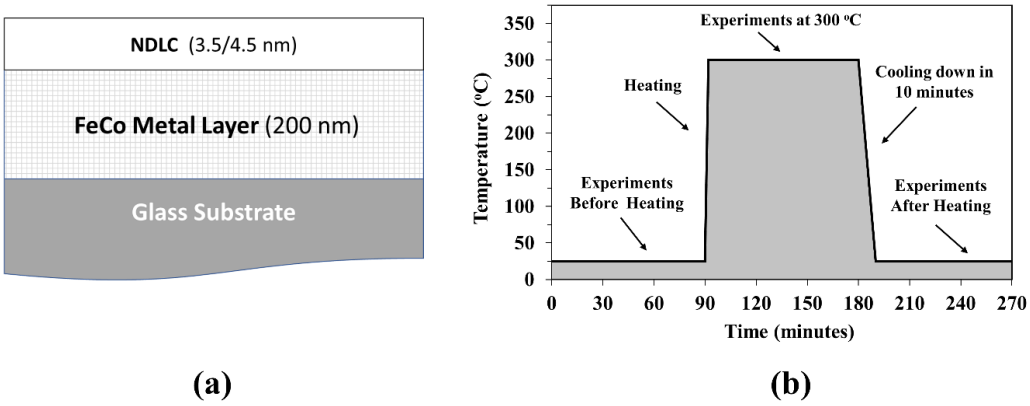

Figure 11. (a) Schematic diagram of cross section of HAMR media, (b) experimental procedure used in this study.

The experimental procedure used in this study is shown in Figure 11(b). Three experimental conditions were selected for the study, namely 25 ^{o}C before heating, 300 ^{o}C and 25 ^{o}C after heating. The literature shows that laser heating can instantaneously (in nanoseconds) increase the temperature of HAMR media up to 600 ^{o}C [16]. However, diamond indenters used for nanoindentation experiments undergo rapid oxidation at or above 400 ^{o}C in air environment, which may affect the surface of the indenter, leading to unreliable measurements [17]. To prevent this rapid oxidation of the diamond indenter, 300 ^{o}C was chosen for the high temperature tests in this study. The samples were heated

to 300 ºC in argon gas environment at a rate of 150 ºC/min and kept for 90 minutes in order to perform multiple tests for reliable measurements with minimal thermal drift. After performing high temperature nanoindentations, the samples were cooled down to room temperature (25 ºC) in argon environment with a cooling rate of 30 ºC/min. All room temperature experiments before and after heating were performed in air environment. Therefore, the HAMR samples were heated for much longer time than the application, which is considered a more extreme condition.

X-ray Photoelectron Spectroscopy (XPS) was performed in order to investigate the chemical structure of NDLC films after heat treatment. From the XPS results, nitrogen content in NDLC-3.5 and NDLC-4.5 films were found to be 9-10% before and after heating. The amount is close to the optimum nitrogen content (10%) beyond which DLC leads to decrease in sp^3 content, and thus hardness and density [44,45]. XPS results also revealed that carbon and nitrogen atoms of both NDLC-3.5 and NDLC-4.5 films underwent sp^3 to sp^2 transformation after heating at 300 ºC, making the thin films softer after heat treatment. However, no significant difference in sp^3/sp^2 ratio between NDLCs before and after heat treatment was found, implying thickness independent behavior of sp^3/sp^2 ratio.

3.2.2. Nanoindentation experiments

Nanoindentation experiments were performed using different indenters to measure mechanical properties of different film layers of HAMR media. Specifically, three different indenters were used as shown in Table 4. First, a Berkovich indenter with a radius of 320 nm, termed as Indenter 1, was used for nanoindentation experiments to determine

mechanical properties of bare glass. For characterization of thinner layers, cube corner indenters were used and experimental responses were fitted with an FEA model to extract their nanomechanical properties. To obtain mechanical properties of FeCo metal layer using nanoindentation, a cube corner indenter with a radius of 80 nm, termed as Indenter 2, was used. For NDLC-3.5 and NDLC-4.5 layers, even shallower indentations were necessary using much sharper intenders. For this purpose, another cube corner indenter with a radius of 72 nm was used (termed as Indenter 3). All nanoindentation experiments were performed at three experimental conditions: 25 ^{o}C before heating, at 300 ^{o}C and 25 ^{o}C after heating.

Table 4. List of indenters used for this study

Indenter No.	Indenter type	Radius (nm)	Use of indenter geometry in FEA	Used for mechanical properties of
1	Berkovich	320	No	Bare glass
2	Cube Corner	80	Yes	FeCo metal layer
3	Cube Corner	72	Yes	NDLCs

3.3. Finite element modeling

3.3.1. Model description

An FEA model, as shown in Figure 12, was created and used in the study to simulate nanoindentation load-displacement responses to accurately predict the nanomechanical properties of FeCo metal layer and NDLC films. The model was built as 2D axisymmetric in ABAQUS 6.14 software [46] to reduce computational complexities. The indenter was modeled as an analytic rigid surface. To capture the tip bluntness, the bottom part of the indenter was modeled as a truncated sphere along with the cube corner indenter geometry.

As shown in Figure 12(b), “a” is the flat part length of the indenter, “R” is the indenter radius and "θ" is the effective cone angle for cube corner geometry. For shallower indentations, the maximum penetration depths were within the spherical part of the indenter. The sample geometry was modeled with NDLC layer of thickness 3.5/4.5 nm, FeCo metal layer of 200 nm thickness and glass substrate of 400 nm thickness. The width of the model was 400 nm. The sample was modeled with 5467 linear quadrilateral reduced integration elements (CAX4R) [47]. Only the thickness of NDLCs were changed (3.5 nm and 4.5 nm), keeping the total number of elements constant. The region closer to the indenter was heavily meshed. The minimum element size was $1 \times 0.6\ \mathrm{nm}^2$ for the model with 3.5 nm NDLC layer and $1 \times 0.7\ \mathrm{nm}^2$ for the model with 4.5 nm NDLC layer. Maximum element size was $15 \times 20\ \mathrm{nm}^2$, which was used for glass substrate. The stress-strain response was assumed as elastic-perfectly plastic. Similar assumption was also used in other studies [48,49]. Due to very thin NDLC films, and to reduce complexities in FEA, von mises plasticity theorem has been applied for NDLCs. The plasticity theorem was also applied for the FeCo metal underlayer. Similar approach has been found elsewhere [50–53]. Boundary conditions were applied on the axis of symmetry to constrain rotations and lateral movements; and to the bottom of the sample to constrain rotations and vertical movements. As Indenters 2 and 3 were separately used for FeCo metal layers and NDLCs respectively, both geometries were used in the FEA model.

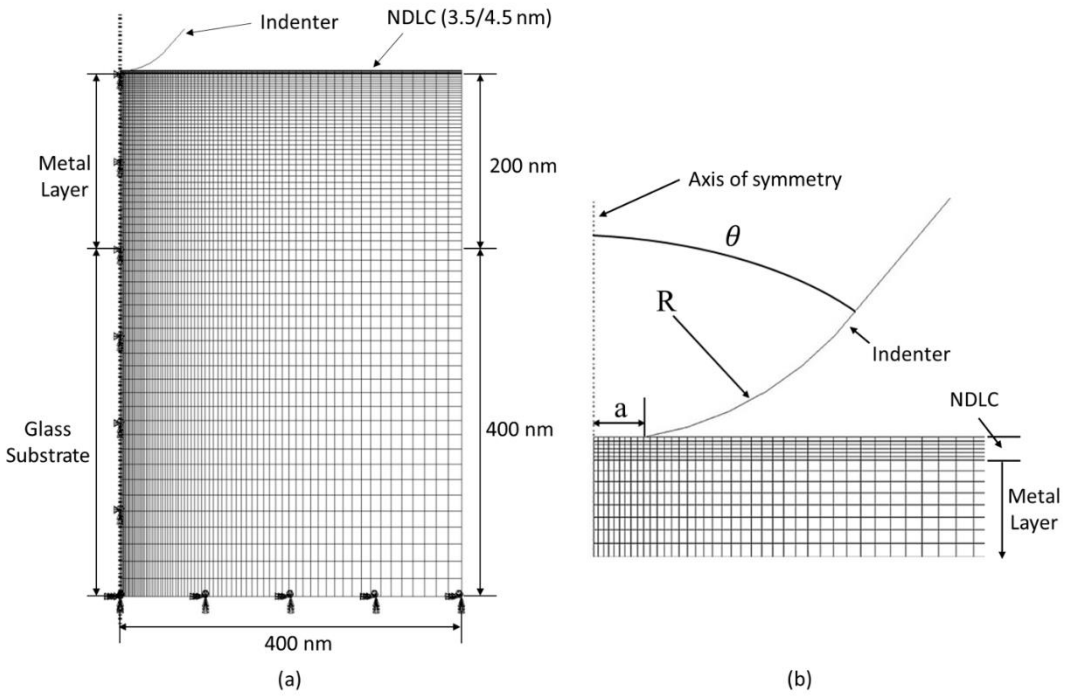

Figure 12. (a) FEA model of the indenter and sample with different layers (b) zoomed-in view of the model showing NDLC layer and indenter details.

3.3.2. Model validation

Fused quartz was used as reference material to determine the flat part geometries of Indenters 2 and 3 from FEA. At first, very low load indentations were performed using both indenters so that the fused quartz does not undergo any plastic deformation. In this case, the indenter acts as a flat punch which only elastically compresses the fused quartz [54]. After that, experimental responses were fitted with FEA to determine the flat part lengths of the indenters. A reduced modulus of 69.6 GPa and Poisson's ratio of 0.17 were used for fused quartz in the FEA model. The hardness of fused quartz was 9.25 GPa, which was found from vendor data.

Figure 13 shows nanoindentation load-displacement responses with FEA fittings using both Indenter 2, Figure 13(a-f), and Indenter 3, Figure 13(g-l). To determine the flat part

length of Indenter 2, very shallow indentation was performed causing no plastic deformation and FEA was performed to simulate elastic nanoindentation response as shown in Figure 13(a). From FEA fitting, the flat part radius was determined to be 13 nm. To validate the geometry from FEA, shallow nanoindentations were performed using Indenter 2 at different loads (Figure 13(b-f)) and FEA fittings were performed to predict the elastic modulus and yield strength of fused quartz. Table 5 summarizes the properties of fused quartz from FEA fitting for Indenter 2. The average elastic modulus and yield strength was found as 68.6 GPa and 4.8 GPa respectively, which were within the acceptable range from the literature, as shown in Table 5. Using the same procedure, the flat part length of Indenter 3 was found as 10.5 nm (Figure 13(g)). After FEA fittings of nanoindentation responses for Indenter 3 (Figure 13(h-l)), the average elastic modulus and yield strength were found as 69.7 GPa and 4.5 GPa respectively, which were also within acceptable range from the literature.

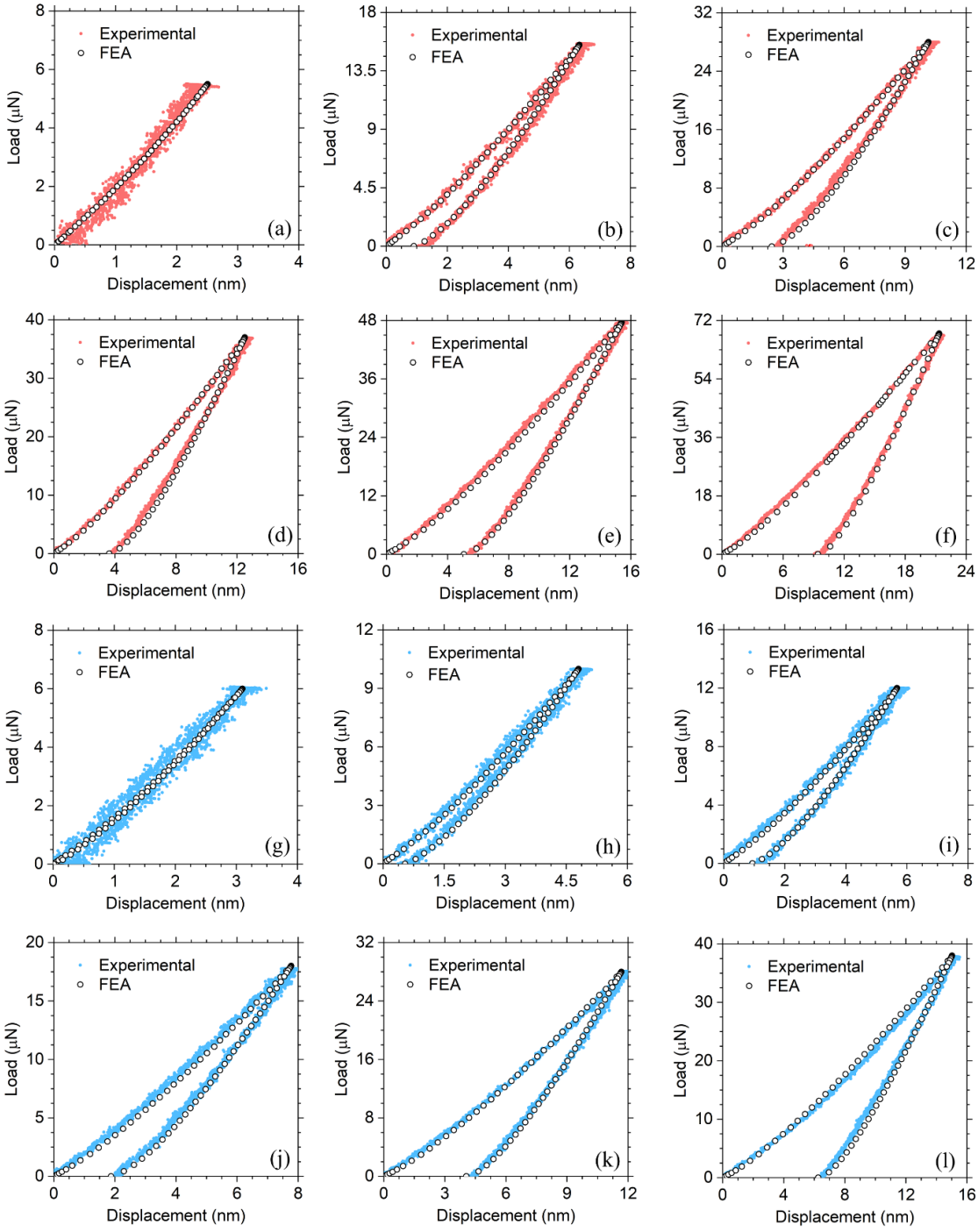

Figure 13. Experimental and FEA comparison of nanoindentation load-displacement curves (at different peak loads) to extract mechanical properties of fused quartz. Figures (a-f) and (g-l) represent the results for Indenters 2 and 3 respectively.

Table 5. FEA fitted results of nanoindentation on fused quartz using Indenters 2 and 3.

Indenter 2 R: 80 nm a: 13 nm	**Load (μN)**	6	16	28	37	48	68	**Average**	**Yu et al. (2004)**[49]	**Shim et al. (2005)**[48]
	Elastic Modulus (GPa)	72	68	68	69	68	67	**68.6**	67.6	72
	Yield Strength (GPa)	-	4.3	4.7	4.9	5.1	4.8	**4.8**	4.3	5.5
Indenter 3 R: 72 nm a: 10.5 nm	**Load (μN)**	6	10	12	18	28	38	**Average**	**Yu et al. (2004)**[49]	**Shim et al. (2005)**[48]
	Elastic Modulus (GPa)	72	71	70	71	67	67	**69.7**	67.6	72
	Yield Strength (GPa)	-	4.6	4.4	4.6	4.4	4.4	**4.5**	4.3	5.5

3.4. Results and discussion

3.4.1. Mechanical properties of bare glass from nanoindentation

Figure 14 shows nanoindentation results of bare glass using Indenter 1. Figure 14(a) shows nanoindentation curves of bare glass with 200 μN applied load for 3 different conditions: 25 ^{o}C before heat, at 300 ^{o}C and 25 ^{o}C after heat. In Figure 14(a), it is evident that nanoindentation curves before heat and after heat are overlapped, indicating that the maximum displacement and residual displacement of indentation at 25 ^{o}C before and after heating were almost the same, and therefore the nanomechanical properties were also almost the same for both conditions. However, at 300 ^{o}C, nanoindentation showed higher maximum depth and higher residual depth than 25 ^{o}C before and after heating. From the behavior shown in Fig 4(a), it can be concluded that although the mechanical behavior of bare glass deteriorated at 300 ^{o}C, its mechanical properties were almost fully recovered after removal of heat. The Oliver-Pharr method [18] was used to calculate hardness and elastic modulus of the glass substrate, given by equations (1-3).

Figure 14(b) shows the extracted nanomechanical properties. It was found that the reduced modulus of bare glass remained almost unchanged at 25 ^{o}C before heating, 300 ^{o}C and 25 ^{o}C after heating. The reduced modulus was found in the range of 95.2-97.3 GPa. However, the mean hardness of the bare glass decreased from 8.5 GPa at 25 ^{o}C before heating to 6.7 GPa at 300 ^{o}C, showing about 21% decrease in hardness at 300 ^{o}C. Interestingly, after removal of heat, the mean hardness of bare glass was fully recovered to 8.5 GPa. Due to very high glass transition temperature, the reduced modulus of the glass did not significantly change at 300 ^{o}C. However, the hardness of the glass reduced at 300 ^{o}C due to annealing effect. Similar behavior was also found for soda-lime glass in the literature [55]. Thorough investigation is required to understand more details of temperature dependence behavior of the glass. In order to use bare glass properties in FEA, Poisson's ratio and yield strength of glass need to be known. From vendor data, the Poisson's ratio of glass was 0.2 and used for all temperature conditions. Lee et al. [51] proposed a model to correlate H, E and yield strength (Y) of a material using FEA, and compared their model with other models and experimental findings. The model correlation is given by equation 6.

$$\frac{H}{Y} = 2.7936 + 0.2438\left(\frac{E-200}{100}\right) - 0.0244\left(\frac{Y-7.5}{2.5}\right) - 0.2123\left(\frac{E-200}{100}\right)^{2}\left(\frac{Y-7.5}{2.5}\right) \quad (6)$$

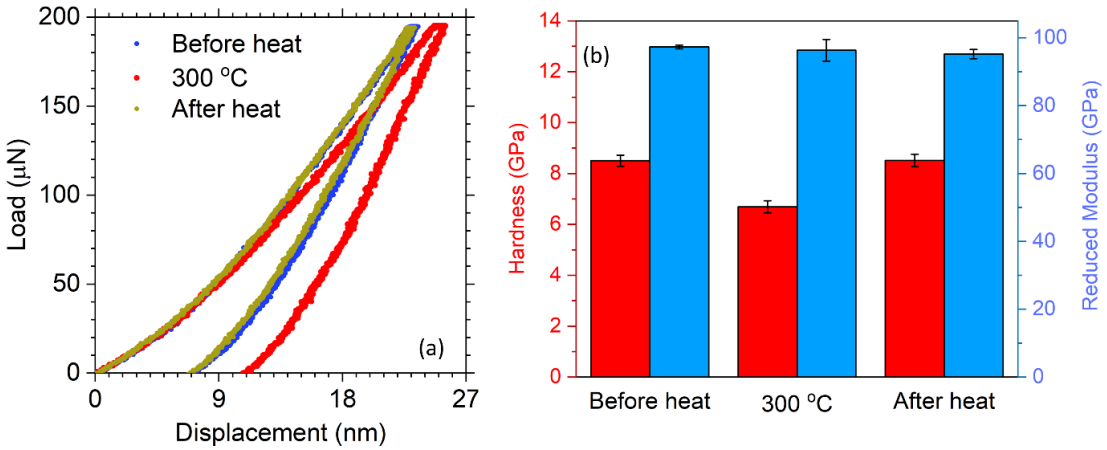

Figure 14. (a) Nanoindentation curves of bare glass for 200 µN load at different temperature conditions, (b) Nanomechanical properties of bare glass extracted from nanoindentation.

From equation 6, the Y of glass substrate at different temperature conditions was calculated using the nanoindentation results. As E_r remained almost constant at all temperature conditions, the average value of 96.27 GPa was used in FEA. A summary of bare glass properties used for FEA are shown in Table 6. From the table, it is evident that Y of glass before heating was 2.8 GPa, showing good agreement with results found from the literature [54]. At 300 °C, Y decreased to 2.2 GPa, showing a 21% reduction from 25 °C before heating. However, after removal of heat, Y was recovered to 2.8 GPa.

Table 6. Mechanical properties of bare glass

Condition	Yield Strength, Y (GPa) from equation (4)	Average Reduced Modulus, E_r (GPa)	Poisson's ratio
25 °C Before heat	2.8	96.27	0.2
300 °C	2.2		
25 °C After heat	2.8		

3.4.2. Mechanical properties of FeCo metal layer from FEA

Nanoindentation experiments were performed using Indenter 2 with a maximum depth range of 14-20 nm to extract nanomechanical properties of the FeCo metal layer. The sample with NDLC thickness of 2.1 nm was used for the study of the metal layer. The depth range is much higher than the NDLC thicknesses so that the effects of NDLC can be considered negligible [54]. Peak loads with a range of 100-110 μN were used for nanoindentations at 25 ^{o}C before heat and 70-90 μN range was used for nanoindentations at 300 ^{o}C and 25 ^{o}C after heat. Using the input from bare glass properties, nanoindentation load displacement curves were fitted with FEA simulations and the mechanical properties of FeCo metal layer were extracted. To obtain FeCo properties at a particular temperature condition, bare glass properties at the same temperature condition was entered in FEA. Poisson's ratio of 0.3 was used for FeCo metal layer which was also used by Katta et al. [52]

Figure 15 shows experimental and FEA fitted data of nanoindentation load-displacement curves for metal layers at different temperature conditions. Figures. 15(a-d), 15(e-h) and 15(i-l) correspond to 25 ^{o}C before heat, 300 ^{o}C and 25 ^{o}C after heat conditions. From Figure 15, it was found that indenter 2 penetrated the NDLC coatings at higher displacements, causing very small steps during loading. This may be attributed to cracking of NDLCs at higher displacements. Similar behavior was also found in the literature for DLC coatings on soft substrate systems [56,57]. A summary of FEA predicted nanomechanical properties of FeCo metal layer were shown in Table 7. Average elastic modulus and yield strength of the FeCo metal layer were determined as 148.9 GPa and

5.95 GPa, respectively. Mechanical properties found before heating were higher than those reported in other studies[52,54]. This may be attributed to higher FeCo metal layer thickness in HAMR media than earlier magnetic media samples. Increasing FeCo thickness may lead to increase in rigidity of the film, and thus enhancement of the mechanical behavior of the film.[52,54]. At 300 ^{o}C, both elastic modulus and yield strength decreased to 141.4 GPa and 5.45 GPa respectively, showing 4% and 9% reductions respectively, compared to 25 ^{o}C before heating. However, after removal of heat, the average elastic modulus and yield strength were found as 147.2 GPa and 6.0 GPa, showing almost full recovery of the properties before heating. This also ensures the robustness of the FeCo metal layer up to 300 ^{o}C, which is very important for HAMR disk reliability.

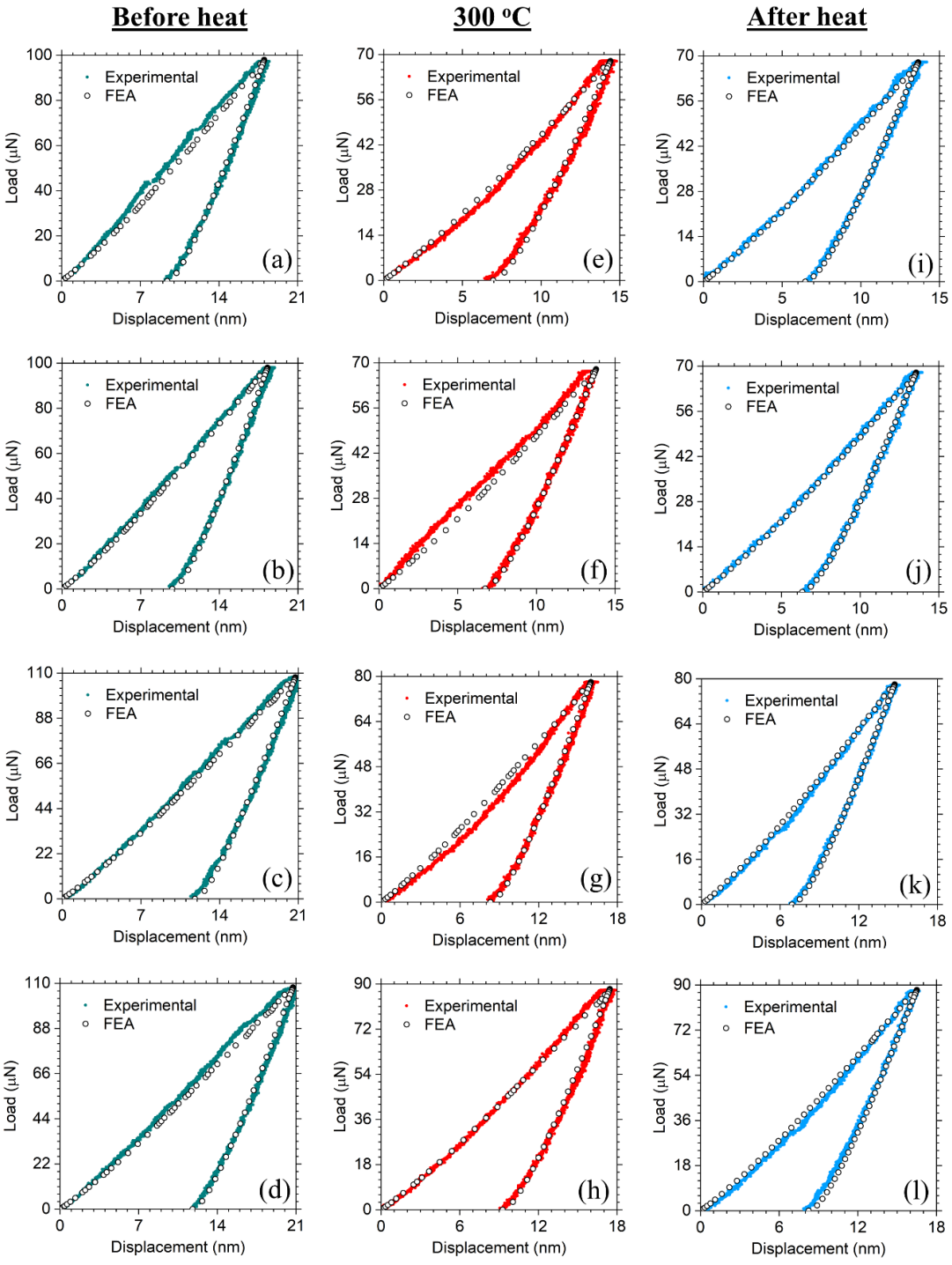

Figure 15. Experimental and FEA comparison of nanoindentation load-displacement curves at different temperature conditions to extract mechanical properties of FeCo metal layer. Figures (a-d), (e-h) and (i-l) represent the results for 25 °C before heat, 300 °C and 25 °C after heat respectively. Four experiments are shown at each condition to ensure repeatability.

Table 7. Nanomechanical properties of FeCo metal layer predicted from FEA

Before heat			300 ºC			After heat		
Load (µN)	**Elastic Modulus (GPa)**	**Yield Strength (GPa)**	**Load (µN)**	**Elastic Modulus (GPa)**	**Yield Strength (GPa)**	**Load(µN)**	**Elastic Modulus (GPa)**	**Yield Strength (GPa)**
100	151	6.2	70	133	5.4	70	145	5.7
100	152	6	70	150	5.5	70	145	5.8
110	146	5.8	80	141	5.4	80	150	6.3
110	146	5.8	90	142	5.5	90	150	6.2
Average	**148.9**	**5.95**		**141.4**	**5.45**		**147.2**	**6.00**
St. Dev.	3.0	0.17		5.9	0.05		2.6	0.25

3.4.3. Nanomechanical properties of NDLCs from FEA

Due to very shallow sub-5 nm thickness of NDLCs and instrument limitations, it is almost impossible to perform nanoindentations within 10% of the NDLC film thicknesses. Therefore, very shallow indentations were performed with different loads at each temperature to obtain plastic deformations at minimal contact depths (that is, the peak load was varied to obtain the same contact depth). Very shallow nanoindentations were performed using Indenter 3 to measure the nanomechanical properties of NDLC-3.5 and NDLC-4.5 films. Mechanical properties of glass and FeCo metal layer determined previously were entered in the FEA model to curve fit the experimental responses for NDLCs. To obtain NDLC properties at a particular temperature condition, glass and FeCo properties at that temperature condition were entered in FEA. For NDLCs, Poisson's ratio of 0.24 was used for all temperature conditions, in agreement with Katta et al. [52] in their study of magnetic storage applications. Figures 16 and 17 show load-displacement responses with fitted FEA simulations of NDLC-3.5 and NDLC-4.5 samples respectively

at different experimental conditions. FEA fitted results of NDLC-3.5 and NDLC-4.5 were shown in Table 8 and average mechanical properties were calculated.

Comparison of elastic modulus and yield strength between NDLC-3.5 and NDLC-4.5 are also shown in Figure 18. It was found that at 25 ^{o}C before heating, NDLC-4.5 showed higher elastic modulus and yield strength than NDLC-3.5. Higher thickness of NDLC-4.5 led to its enhanced rigidity and resistance to permanent deformation compared to NDLC-3.5. Average elastic modulus of NDLC-3.5 and NDLC-4.5 were found as 237.2 GPa and 255.6 respectively. Average yield strength of NDLC-3.5 and NDLC-4.5 were found as 11.0 GPa and 12.8 GPa respectively. At 300 ^{o}C, both elastic modulus and yield strength of the thin films deteriorated. For NDLC-3.5, elastic modulus and yield strength were found as 222.4 GPa and 7.4 GPa respectively, showing 6% and 32% reduction, compared to 25 ^{o}C before heat properties. Similarly, for NDLC-4.5, reduced modulus and yield strength were found as 227.8 GPa and 8.8 GPa respectively, showing 11% and 31% reduction, compared to 25 ^{o}C before heat. NDLC-4.5 showed better mechanical properties than NDLC-3.5 due to increased resistance to plastic deformation with thickness.

After cooling down to room temperature, elastic modulus and yield strength of both NDLC-3.5 and NDLC-4.5 were not fully recovered, contrary to bare glass substrate and FeCo metal layer behavior. For NOC-3.5, elastic modulus and yield strength were found as 225.2 GPa and 8.6 GPa respectively, showing 5% and 22% reduction, compared to 25 ^{o}C before heat properties. For NDLC-4.5, elastic modulus and yield strength were found as 239.6 GPa and 10.2 GPa respectively, showing 6% and 20% reduction, compared to 25 ^{o}C before heat properties. Even after cooling down to room temperature, NDLC-4.5

showed better mechanical properties than NDLC-3.5. The reduction in mechanical properties for both NDLC films is attributed to the sp^3 to sp^2 transformation of carbon and nitrogen atoms of NDLC films, which was in good agreement with Rose et al.[42] and XPS analysis from a separate study [15].

In this study, the standard deviation in elastic modulus values of NDLCs were found within 5-14% of the average elastic moduli, whereas standard deviations in yield strength were within 7-12% of average yield strength values. Due to very shallow sub-5 nm thickness of NDLCs and instrument limitations, it is very difficult to measure true mechanical properties of NDLCs from experiments alone, without any substrate effect. Therefore, experimental results of NDLCs were not reported in this study. Instead, FEA was used to predict the properties of NDLCs using modified indenter geometry and entering other HAMR components' mechanical properties. Variation of FEA predicted mechanical properties of NDLCs with nanoindentation contact depths was also shown in Appendix B.

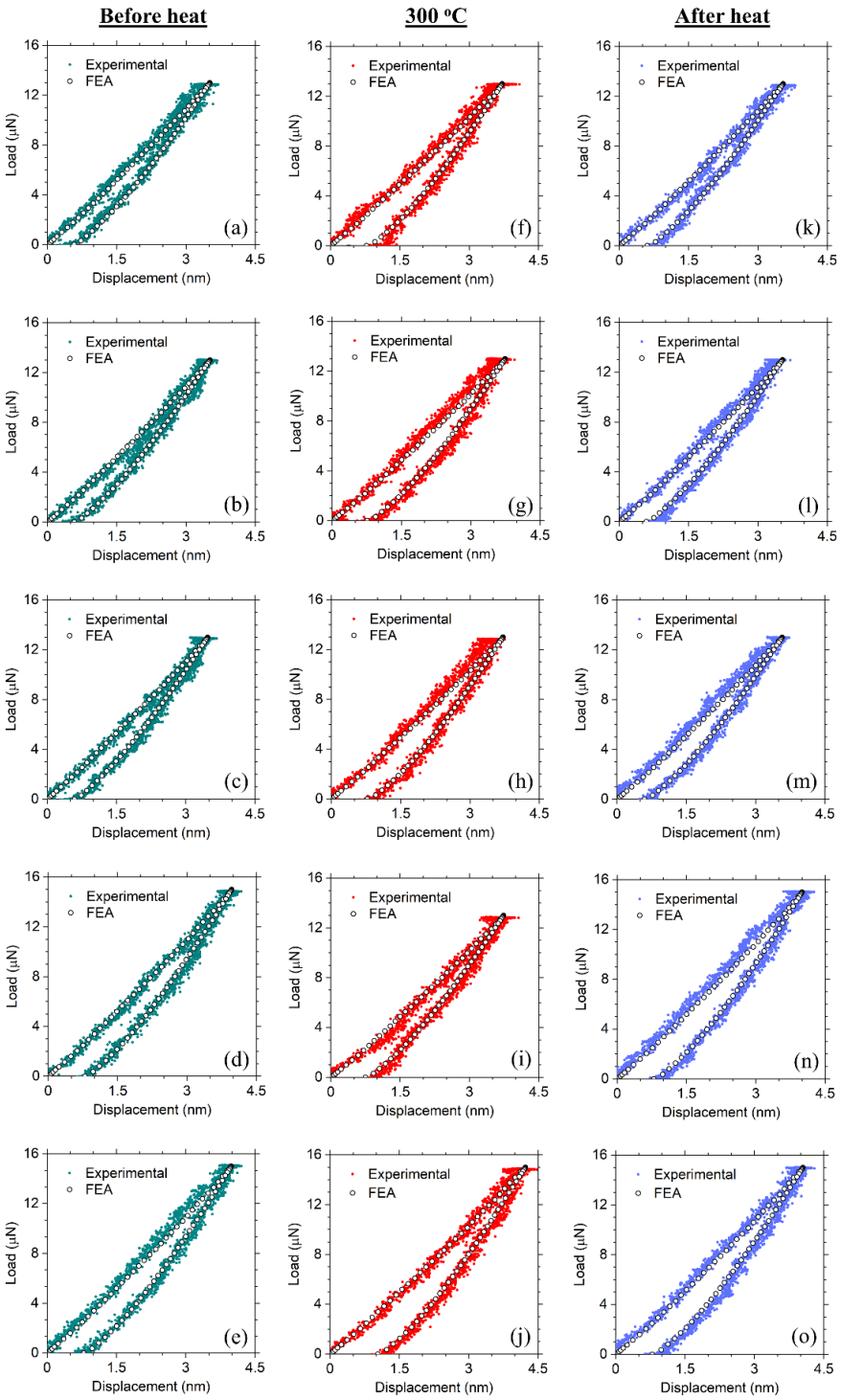

Figure 16. Experimental and FEA comparison of nanoindentation load-displacement curves at different temperature conditions to extract mechanical properties of NDLC-3.5 film. Figures (a-e), (f-j) and (k-o) represent the results for 25 °C before heat, 300 °C and 25 °C after heat respectively. Five experiments are shown at each condition to ensure repeatability.

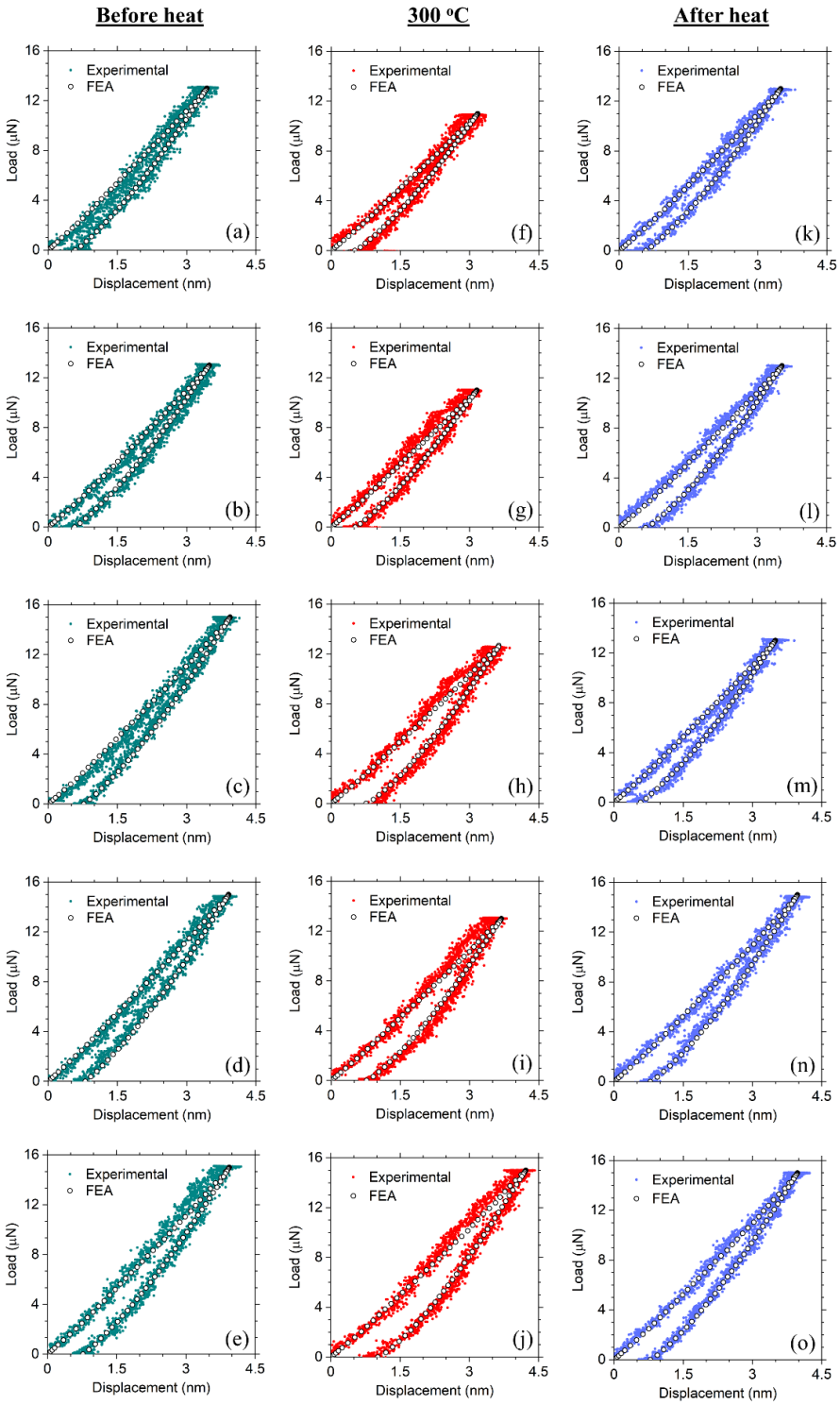

Figure 17. Experimental and FEA comparison of nanoindentation load-displacement curves at different temperature conditions to extract mechanical properties of NDLC-4.5 film. Figures (a-e), (f-j) and (k-o) represent the results for 25 °C before heat, 300 °C and 25 °C after heat respectively. Five experiments are shown at each condition to ensure repeatability.

Table 8. Nanomechanical properties of NDLC-3.5 and NDLC-4.5 predicted from FEA

	Before heat			300 ºC			After heat		
	Load (µN)	**Elastic Modulus (GPa)**	**Yield Strength (GPa)**	**Load (µN)**	**Elastic Modulus (GPa)**	**Yield Strength (GPa)**	**Load (µN)**	**Elastic Modulus (GPa)**	**Yield Strength (GPa)**
NDLC-3.5	13	216	12	13	245	7	13	245	8
	13	216	10	13	245	7	13	245	10
	13	292	12	13	188	7	13	202	8
	15	245	12	13	188	8	15	188	8
	15	216	9	15	245	8	15	245	9
	Average	**237.2**	**11.0**		**222.4**	**7.4**		**225.2**	**8.6**
	Standard Deviation	29.8	1.3		28.2	0.5		25.2	0.8
	Before heat			**300 ºC**			**After heat**		
	Load (µN)	**Elastic Modulus (GPa)**	**Yield Strength (GPa)**	**Load (µN)**	**Elastic Modulus (GPa)**	**Yield Strength (GPa)**	**Load (µN)**	**Elastic Modulus (GPa)**	**Yield Strength (GPa)**
NDLC-4.5	13	216	11	11	216	9	13	216	9
	13	245	11	11	245	10	13	245	11
	15	245	14	13	245	9	13	245	11
	15	245	14	13	216	8	15	245	10
	15	325	14	15	216	8	15	245	10
	Average	**255.6**	**12.8**		**227.8**	**8.8**		**239.6**	**10.2**
	Standard Deviation	36.7	1.5		14.4	0.7		11.8	0.7

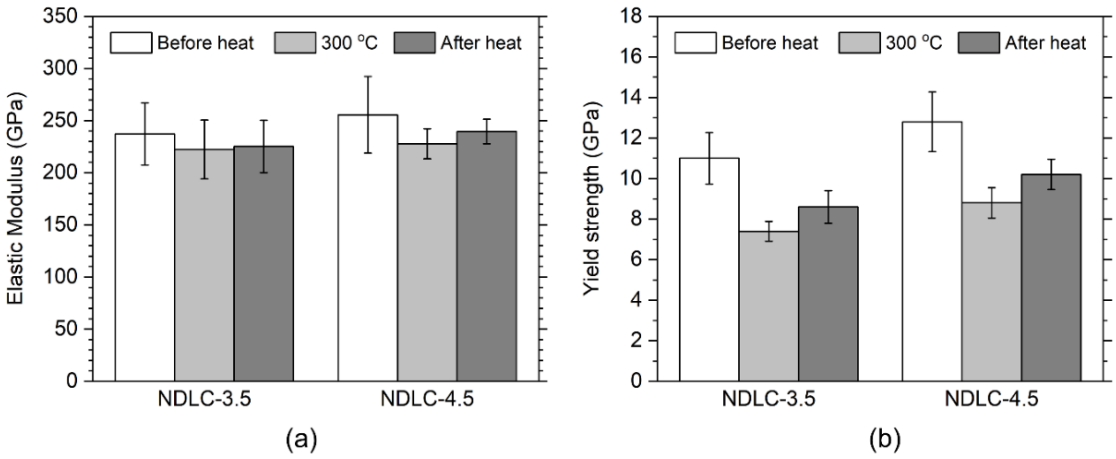

Figure 18. (a) Elastic modulus and (b) Yield strength of NDLC films at different temperature conditions

3.4.4. Comparison of extracted yield strength values of NDLCs using scratch hardness

In an earlier study, nanoscratch hardness of NDLC films were calculated for NDLC-3.5 and NDLC-4.5 films. Tayebi's model [20] was used in that study to determine scratch hardness with minimum substrate effect. Detailed experimental procedures of scratch hardness tests were discussed in that study [15]. To calculate scratch hardness using the Tayebi model, elastic modulus of the material is required, which was determined from nanoindentation. Due to instrument limitations and very thin NDLC films, it was found that the elastic modulus of NDLC cannot be determined without substrate effect from the experiments. A method to overcome this substrate effect is to use the true elastic modulus of NDLCs in Tayebi's model to accurately calculate scratch hardness. In this FEA study, the elastic modulus of NDLCs was determined and then used in Tayebi's model to recalculate scratch hardness of NDLC films.

Figure 19 shows the summary of the updated scratch hardness results of NDLC films at different temperature conditions. The calculated hardness values were found much higher than those reported in our recent study, ranging from 7% to 24% increase in scratch hardness values compared to previous study for different NDLCs and experimental conditions. Changes in values are due to the use of true elastic modulus of NDLCs from this study which were not possible to accurately determine from pure experiments performed in the previous study, due to substrate effects. However, the trend of the new results remained similar with the previous findings. It was found that at 300 ^{o}C, scratch hardness of NDLC films decrease from 25 ^{o}C before heating, and then recovered up to a certain limit at 25 ^{o}C after removal of heat. NDLC-4.5 showed higher scratch hardness than NDLC-3.5 at all temperature conditions, as higher NDLC thickness leads to better resistance to permanent deformation.

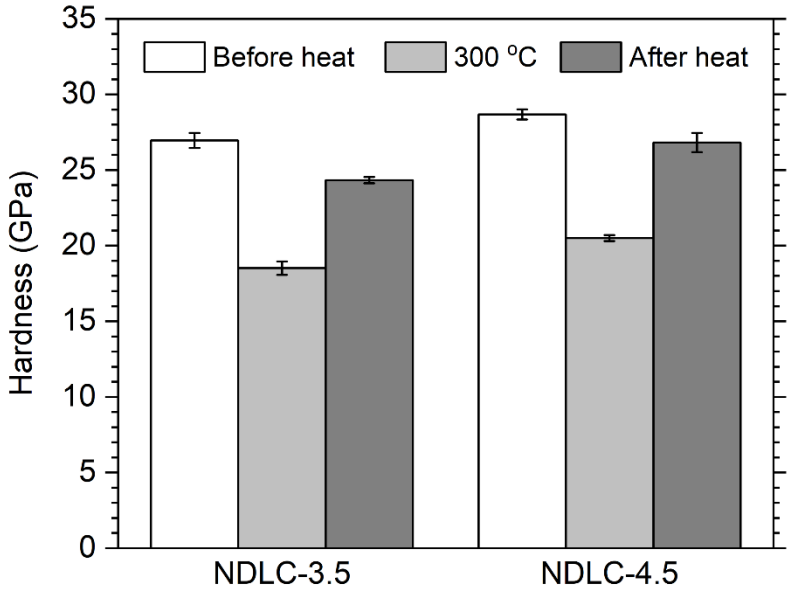

Figure 19. Updated scratch hardness of NDLC films at different temperature conditions

Using updated scratch hardness results, hardness (*H*) to yield strength (*Y*) ratio was compared for NDLCs of sub 5-nm thickness at different experimental conditions. The calculated results are shown in Table 9. From the results, it is evident that *H/Y* is not a fixed value for NDLC films with different thicknesses and at different temperature conditions. Overall, the *H/Y* ratio ranges between 2.2-2.8. From the literature, the H/Y ratio of DLC films is found to be within the range of 1.0-2.0 [58–63], which is lower than the *H/Y* ratio of NDLC films found in this study. This may be attributed to the following factors. First, the earlier studies were performed on thicker DLC films, whereas the NDLC films are of sub- 5 nm thickness, which may affect the *H/Y* ratio. NDLC-4.5 showed lower *H/Y* ratios compared to NDLC-3.5, at all experimental conditions, indicating thickness dependence of *H/Y* ratio. Moreover, *H/Y* ratio also changed with temperature and chemical structure of NDLCs. Nitrogen doping may also have an effect of *H/Y* ratio of NDLCs. Further studies are needed to investigate *H/Y* ratio of NDLCs with respect to film thickness.

Table 9. *H/Y* ratios of NDLC films at different thickness and temperature conditions

Conditions	Mechanical Properties	NDLC- 3.5	NDLC- 4.5
Before heat	Average Hardness, H (GPa)	26.95	28.68
	Average Yield Strength, Y (GPa)	11.00	12.80
	H/Y	**2.45**	**2.24**
300 °C	Average Hardness, H (GPa)	18.52	20.51
	Average Yield Strength, Y (GPa)	7.40	8.80
	H/Y	**2.50**	**2.33**
After heat	Average Hardness, H (GPa)	24.33	26.82
	Average Yield Strength, Y (GPa)	8.60	10.20
	H/Y	**2.83**	**2.63**

3.5. Summary

In this study, nanoindentation experiments were performed on HAMR magnetic media at different contact depths and temperature conditions. The results were fitted with FEA to extract the yield strength and elastic modulus of different thin film layers. Following conclusions can be drawn from this study:

(1) Elastic modulus of the glass substate remained constant at 25 ^{o}C before and after heating, and at 300 ^{o}C. However, the hardness of the glass substrate decreased at 300 ^{o}C, but recovered after removal of heat, showing similar hardness of glass substrate at 25 ^{o}C before and after heating.

(2) For FeCo metal layers, at 300 ^{o}C, both elastic modulus and yield strength decreased, compared to 25 ^{o}C before heating. After removal of heat, both properties were recovered to the initial values. Higher recovery of mechanical properties of the glass substrate and the FeCo metal layer indicates enhanced robustness of HAMR media system up to 300 ^{o}C.

(3) At 300 ^{o}C, both NDLC-3.5 and NDLC-4.5 films showed reduction in elastic modulus and yield strength, compared to 25 ^{o}C before heating. The properties of NDLCs were not fully recovered after removal of heat and significant reduction in elastic modulus and yield strength were found at 300 ^{o}C and 25 ^{o}C after heat. NDLC-4.5 showed better mechanical properties than NDLC-3.5 at all temperature conditions, indicating that higher film thickness leads to better rigidity of the film and resistance to permanent deformation at high temperature operations.

(4) *H/Y* ratios of NDLC films were found in the range of 2.2-2.8, which was higher than previous *H/Y* studies on thicker DLC films. These changes may be attributed to film thickness, temperature, chemical structure and doping materials.

In this chapter, true mechanical properties were obtained for NDLCs with similar carbon configurations, focusing only on thickness dependence mechanical properties. Next, in Chapter IV, NDLCs with different carbon configurations were studied and their effect on mechanical and tribological behaviors were investigated.

CHAPTER IV

EFFECT OF CARBON CONFIGURATION ON MECHANICAL, FRICTION AND WEAR BEHAVIOR OF NITROGEN-DOPED DIAMOND LIKE CARBON FILMS FOR MAGNETIC STORAGE APPLICATIONS [64][3]

4.1. Introduction

Different doping materials have been utilized to improve the performance of DLCs for different applications [65–67]. For magnetic storage applications, nitrogen doped DLC (NDLC) has caught the most attention. Nitrogen has been used as the dopant to improve mechanical, friction and wear behavior, and thermal stability of DLCs [7,31,68]. Khurshudov et al. studied the mechanical properties of carbon nitride thin films and showed that friction can be significantly reduced by doping carbon films with nitrogen [30]. Nitrogen doping can also increase adhesion performance of DLC films. However, higher amount (> 10%) of nitrogen can decrease sp^3 carbon content, which may lead to deterioration of mechanical properties and increase of surface roughness [69]. Literature shows the optimum amount of nitrogen in DLCs is up to 10%, beyond which, mechanical and tribological behavior deteriorate [44,45,70].

Chemical configuration of NDLCs plays an important role in their mechanical and tribological integrity. Especially, sp^3 and sp^2 carbon contents play a major role in mechanical, friction and wear behavior of NDLC thin films. In this study, high

[3] Reprinted with permission from "Effect of Carbon Configuration on Mechanical, Friction and Wear Behavior of Nitrogen-Doped Diamond-Like Carbon Films for Magnetic Storage Applications." by Shakil A, Amiri A and Polycarpou A.A. *Tribology Letters, 69(4), pp.1-12*. Copyright 2021 by Springer Nature B.V.

temperature mechanical and tribological tests of NDLCs with different sp^2/sp^3 carbon ratios were performed. Chemical compositions of NDLCs before and after heat treatment were investigated using x-ray photoelectron spectroscopy (XPS). Correlation of sp^2/sp^3 ratio of carbon content with mechanical and tribological properties of NDLCs were investigated at room temperature before and after heat treatment and at high temperature.

4.2. Experimental

4.2.1. Sample description and testing protocol

Figure 20(a) depicts a schematic diagram of a simulated HAMR media sample used in this study. Each sample consists of a NDLC film, a FeCo metal layer of 200 nm thickness and a glass substrate as shown in Figure 20(a). The FeCo layer is used as soft underlayer in magnetic storage applications. The glass substrate has a glass transition temperature of 691 ^{o}C, which was found from vendor data. The FeCo metal layer was deposited on the glass by magnetron sputtering technique. DLC was then deposited on the FeCo layer by plasma enhanced chemical vapor deposition (PECVD). The DLC surface was then doped with nitrogen to enhance lubricant bonding sites. NDLC films of two different thicknesses of 3.1 nm and 3.3 nm were deposited using different deposition parameters and named as NDLC-1 and NDLC-2, respectively. Optical ellipsometry was used to measure the coating thicknesses of the samples. Note that samples used in the study are different than those used for the studies in Chapters II and III.

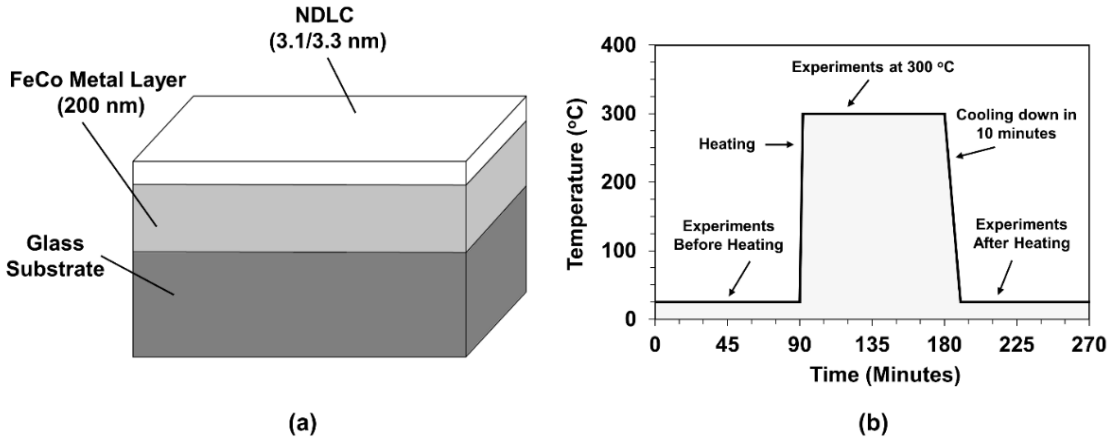

Figure 20. (a) Schematic representation of cross-section of a simulated HAMR disk; (b) Experimental protocol.

Due to laser heating, HAMR drives may instantaneously reach the maximum temperature up to 600 ^{o}C [16]. However, diamond indenters used for nanomechanical characterizations cannot be used at such high temperature. Literature showed that diamond indenters undergo rapid oxidation at 400 ^{o}C, which may significantly alter the surface topography and properties of the indenter, leading to unreliable measurements [17]. Hence, a lower temperature of 300 ^{o}C was chosen for reliable high temperature measurements using the diamond indenter. Moreover, reliable measurements were performed using multiple experiments under the same experimental conditions, which required more time. Also, thermal drift is a major concern especially for high temperature nanomechanical and nanotribological testing and the instrument needs some time before the tests to reduce thermal drift for reliable measurements. As a result, the NDLC samples were heated to higher temperature for much longer time than what they will ever encounter in a hard-disk drive. Surviving samples that subjected to heating for longer time can be considered as a parameter for verification of robustness of the samples [15].

The testing protocol for this study is shown in Figure 20(b). The data collection for NDLC samples was performed at three temperature conditions: at 25 ^{o}C before subjecting samples to heat treatment, at 300 ^{o}C, and at 25 ^{o}C after subjecting the samples to heat treatment. At first, all mechanical and tribological tests were performed under air environment at 25 ^{o}C before heat treatment. The samples were then heated to 300 ^{o}C under inert argon gas environment at a heating rate of 150 ^{o}C/minute and kept for about 90 minutes at 300 ^{o}C. Argon environment was used to reduce the indenter oxidation at high temperature. After high temperature tests, the tested samples were cooled down to 25 ^{o}C with a cooling rate of 30 ^{o}C/minute and mechanical and tribological tests were performed at 25 ^{o}C after removal of heat.

4.2.2. Types of experiments and instrumentation

To investigate the mechanical and tribological behavior of NDLC-1 and NDLC-2 at all three experimental conditions, nanoscratch, nanoindentation and nanowear experiments were performed. A Bruker TI Premier® nanomechanical instrument was used for these experiments, which can perform high temperature tests up to 800 ^{o}C. The standard transducer has a force resolution of 45 nN and a displacement resolution of 0.23 nm. In this study, hardness, and coefficient of friction (COF) at different temperatures were determined from the nanoscratch experiments. Elastic recovery of the samples after nanoscratch tests need to be determined for hardness calculations, for which elastic modulus of NDLCs also need to be known. For this purpose, shallow nanoindentations were performed to determine the reduced modulus of NDLCs with minimal substrate effect. Nanowear tests were performed to compare wear behavior of NDLC-1 and NDLC-

2 thin films at different temperatures. Surface roughness measurements before and after heat treatment were performed using a Bruker Dimension 3100 AFM instrument. Tapping mode was used for the AFM measurements. For elemental analyses of NDLC-1 and NDLC-2 before and after heat treatment, XPS was employed.

4.2.3. Experimental steps and data processing

4.2.3.1. Nanoscratch

Nanoscratch is a technique used to determine mechanical properties of thin films up to 35% of their thicknesses without any substrate effect [71]. In this technique, normal force, lateral force, and residual surface profile are measured and the substrate effect is delayed, compared to nanoindentation [20]. Also, unlike nanoindentation, nanoscratch does not need any prior calibration on a standard sample to determine the mechanical properties. In this study, scratch hardness and COF of NDLC-1 and NDLC-2 were determined using the nanoscratch experiments. Figure 2. shows the load function *vs.* time used for the nanoscratch experiments. To determine scratch hardness with minimal substrate effect at 25 ^{o}C before and after heating and at 300 ^{o}C, a Berkovich indenter of tip radius 220 nm was used (the exact tip radius was determined from elastic nanoindentation on standard fused quartz sample and finite element analysis as per Ref. [43]). The maximum scratch normal load used was 30 μN to ensure plastic deformation of the NDLC samples with only the spherical part of the indenter in contact. The steps of nanoscratch experiments were as follows:

1. Pre-scan the NDLC surface with a minimal load of 2 μN and a lateral displacement of 6 μm to perform any tilt correction on the surface before the actual scratch experiment;
2. Increase the load to 30 μN and scratch the surface with this load for a lateral displacement of 4 μm;
3. Unload to 2 μN after the scratch and post-scan the surface for a lateral displacement of 6 μm to determine residual scan; and
4. Scanning probe microscopy (SPM) imaging of the surface with a 5 μm × 5 μm area using the same indenter after the scratch experiment.

In-situ normal and lateral forces were measured from nanoscratch experiments, and the residual surface scan was obtained from SPM imaging. Tayebi et al. scratch hardness model [20] was used to determine the nanoscratch hardness, given by equations (4-5).

To determine α for scratch hardness measurements from equation 5, an in-situ profile of the surface scan is required. The in-situ surface profile can be determined by superimposing the residual profile from the SPM scan and elastic recovery profile of the surface, which can be determined using Boussinesq theory of potentials. Known elastic modulus of the surface is used to determine the elastic recovery profile. Elastic modulus of NDLCs was determined from very shallow nanoindentation experiments using Oliver-Pharr method [18]. More details of nanoindentation results are discussed in Appendix C.

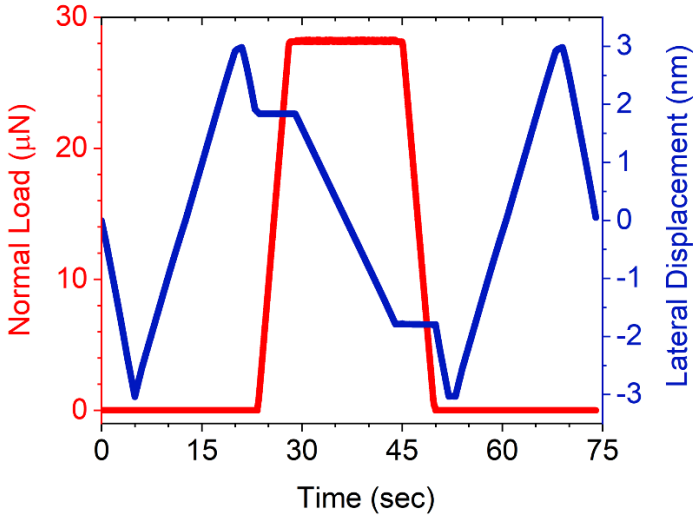

Figure 21. Load function for nanoscratch experiments.

4.2.3.2. Nanowear

In a typical nanowear experiment, the surface is scratched with a higher normal load using a diamond indenter and a rectangular worn area is formed [28,72]. After that, the surface is scanned using the same indenter using a minimal load on a larger area of the surface. Then the average wear depth is determined by comparing the mean height of the worn area with the mean height of the unworn area. In this study, nanowear tests of NDLC films were performed using a Berkovich indenter with a tip radius of 335 nm. Wear tests were performed using a normal load of 20 μN on a 2 μm × 1 μm area (with an initial Hertzian contact pressure of ~10 GPa). After the tests, the residual surface was rescanned with 2 μN normal load on a 3.8 μm × 3.8 μm area. Nanowear tests were performed three times at each temperature and average wear depths were reported for NDLC-1 and NDLC-2 films.

4.2.3.3. Surface analysis

All the samples were argon-sputtered with the lowest energy argon beam provided by the device to minimize the effect of detectable quantity of adventitious carbon contamination. Therefore, since the first layer was a DLC layer and according to [73,74] and the obtained D-parameter, the binding energy scale was calibrated by considering the C-C peak as the dominant peak present at 285.0 eV. Since Fe, Zr and Co elements (from 2nd layer) were initiated in the survey spectra from the 2nd layer, we used high resolution data to perform quantification. CasaXPs software was used for the data processing procedure through calculating peak areas of high-resolution spectra. The Omicron XPS system was equipped with an Argus detector and an excitation source of Mg Ka 1253.6 eV at X-ray power range of 200-300 W. The computer-controlled stage helps in angle-resolved XPS measurements and a CN10 charge neutralizer to minimizing the samples' charging.

4.3. Results and discussion

4.3.1 Elemental analysis

Elemental analysis was performed using XPS to investigate the chemical composition of NDLCs before and after heat treatment, as shown in Table 10. From this table, it was evident that carbon and nitrogen compositions before and after heat treatment were similar and the chemical composition did not change after annealing.

Table 10. Chemical composition of NDLCs from XPS study (BHT/AHT=Before/After heat treatment).

Sample	C 1s				N 1s				Element %		D-Value
	C-C	C=C	C-N/ C-O	C=O	Pyridinic N	Pyrrolic N	Graphitic N	Oxidized N	C (at. %)	N (at. %)	
NDLC-1 (BHT)	51.4± 1.2	16.4± 0.4	24.8± 0.3	7.3± 0.9	28.9±2.6	30.1±2.1	35.3±1.2	5.7±2.2	82.4± 0.2	7.7± 0.3	15.45± 0.1
NDLC-1 (AHT)	48.9± 1.8	18.9± 1.7	26.4± 1.3	5.7± 1.4	39.3±1.9	22.8±1.2	31.9±2.4	6.0±1.5	81.6± 0.9	8.3+ 0.4	15.53± 0.2
NDLC-2 (BHT)	65.4± 0.9	17.5± 1.4	13.4± 0.8	3.7± 0.4	23.5±1.5	48.5±1.5	25.4±1.9	2.6±1.7	84.7± 0.3	6.0± 1.2	15.27± 0.1
NDLC-2 (AHT)	62.8± 1.4	18.5± 1.6	13.6± 1.4	5.1± 1.1	34.4±0.9	39.9±1.4	20.8±0.4	4.9±0.3	82.4± 1.1	7.9± 0.8	15.45± 0.2

Different terminal groups were also studied from XPS spectra, as shown in Table 10. Figures. 22(a) and 22(b) show C 1s spectra of NDLC-1 sample before and after heating, respectively. Figures. 22(c) and 22(d) depict C 1s spectra of NDLC-2 sample before and after heating, respectively. In line with the literature [23,73–75], the C 1s spectra were fitted with four components, which are C=C (sp^2-hybridized carbons) peak at ~ 284.0 eV, C-C (sp^3-hybridized carbons) peak at ~ 285.2 eV, the hydroxyl/C-N bond at ~ 286.6 eV, and a carbonyl bond at ~288 eV. To verify the obtained sp^2/sp^3 content ratio from C 1s, the linear approximation proposed by Lascovich et al. [76] was employed. According to the method presented in the literature [73–75,77], the sp^2/sp^3 content can be evaluated from the C KLL spectra. To this end, it is required to determine the distance between the most positive maximum and most negative minimum of the first derivative of C KLL spectra [73–75,77]. As shown in Table 10, the D parameters for both NDLC-1 and -2 were determined from the same linear approximation method. The D parameter increased from 15.45 eV to 15.53 eV after subjecting to annealing step at 300 ^oC, corresponding to sp^2% content increasing from 23.7% to 24.6% consistent with the proposed linear

approximation by Lascovich et al. [76]. We gained the same value from the curve fitting of C 1s spectra.

A comparison of either Figures 22(a) and 22(b) or Figures. 22(c) and 22(d) clarifies that the peak assigned to sp^3 carbon drops slightly after heat treatment at 300 ^oC. This indicated the partial changes in hybridization of carbon atoms from sp^3 to sp^2 after subjecting samples to annealing at 300 ^oC. After heat treatment, the sp^2/sp^3 carbon ratio in both samples increased by ~7%, which may result in a softer layer [24].

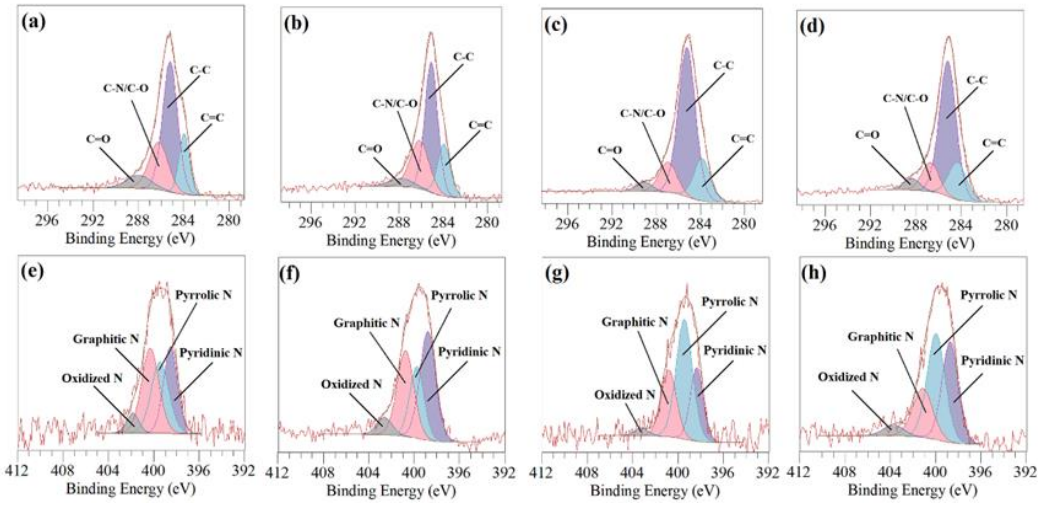

Figure 22. C 1s XPS spectra of (a) NDLC-1 (BHT); (b) NDLC-1 (AHT); (c) NDLC-2 (BHT); and (d) NDLC-2 (AHT). Nitrogen 1s XPS spectra of (e) NDLC-1 (BHT); (f) NDLC-1 (AHT); (g) NDLC-2 (BHT); and (h) NDLC-2 (AHT). BHT/AHT=Before/After heat treatment.

Figures 22(e) and 22(h) show the N 1s spectra for NDLCs before and after heat treatment. The N1s bonds are broad, and they were fitted with four peaks at 398.5, 399.5, 400.5, and 402.6 eV, attributed to pyridinic N, pyrrolic N, graphitic N, and oxidized N [25–29]. Quantitative analysis was performed and the results are provided in Table 10, where the pyrrolic, pyridinic, and graphitic nitrogen contents for both NDLCs before and after heat treatment are

shown. Similar to the N content, changes in nitrogen configurations were insignificant after annealing at 300 ^{o}C. Therefore, a majority of mechanical changes can be attributed to changes in configuration of carbons.

4.3.2. Nanoscratch

4.3.2.1. Scratch hardness

Figure 23(a) depicts a typical line scan of the residual surface after nanoscratch and calculated in-situ surface before elastic recovery. After obtaining the surface profiles, the in-situ profile was plotted on the same scale and the spherical radius of the indenter was fitted onto the profile to determine in-situ contact width (*w*). Since the contact width only depends on geometry, tip-sample convolution was not involved in this process [39]. Using this method, nanoscratch hardness was calculated for NDLC-1 and NDLC-2 films at all experimental conditions and the results were summarized in Figure 23(b). Contact parameters for nanoscratch calculations at different experimental conditions were also shown in Table 11.

From Figure 23(b), it is evident that scratch hardness of NDLC-2 was higher than that of NDLC-1 at 25 ^{o}C before heating. It was attributed to lower sp^2/sp^3 carbon ratio of NDLC-2 films as found from XPS results. Higher relative sp^3 carbon content of NDLC-2 led to increased rigidity of the films, thereby showing increased hardness than NDLC-1 [78,79]. Scratch hardness of NDLC-1 and NDLC-2 at 25 ^{o}C before heating were found as 21.44 GPa and 21.75 GPa, respectively, showing slightly higher hardness for NDLC-2. This may be due to higher percentage of sp^3/sp^2 ratio in NDLC-2. At 300 ^{o}C, scratch hardness of

both NDLC-1 and NDLC-2 deteriorated due to partial alternation of sp^3 to sp^2 hybridization, resulting in softer layer at 300 ^oC [15,42,80]. NDLC-2 showed higher hardness at 300 ^oC than NDLC-1 due to higher relative sp^3 carbon content. Average scratch hardness at 300 ^oC for NDLC-1 and NDLC-2 were 17.63 GPa and 18.62 GPa, respectively, showing ~6% higher hardness for NDLC-2 at 300 ^oC. After cooling down to 25 ^oC, scratch hardness of both NDLCs were lower, compared to those at 25^oC before heat treatment.

Scratch hardness of NDLC-2 after heating was higher than that of NDLC-1, which is related to higher relative sp^3 carbon contents. The same reason is valid for samples after heat treatment, as verified by XPS results. Average scratch hardness of NDLC-1 and NDLC-2 after heat treatment were 19.39 GPa and 20.72 GPa, respectively, showing ~7% higher hardness for NDLC-2.

Because of the nature of very thin films, it is difficult to determine hardness of sub-5 nm thin films from nanoscratch and nanoindentation experiments without any substrate effect. The in-situ contact depths for nanoscratch experiments were over 35 % of NDLC thicknesses (Table 11). However, the residual depths were less than 35% of films thickness, Fig 4(a), implying that nanoscratch can be used over nanoindentation to determine hardness of thin films with less substrate effect.

Table 11. Scratch hardness calculations from nanoscratch experiments. BHT/AHT=Before/After heat treatment.

Samples	Conditions	Normal force (μN)	Lateral force (μN)	In-situ contact width (nm)	In-situ contact depth (nm)	Scratch Hardness (GPa)
NDLC-1	BHT	28.28	3.05	57.0	1.85	22.10
	300 ºC	28.17	3.73	64.5	2.38	17.31
	AHT	28.11	3.45	61.0	2.12	19.30
NDLC-2	BHT	28.16	3.43	57.0	1.85	22.16
	300 ºC	28.23	9.91	62.0	2.20	19.02
	AHT	28.19	4.95	59.0	1.99	20.75

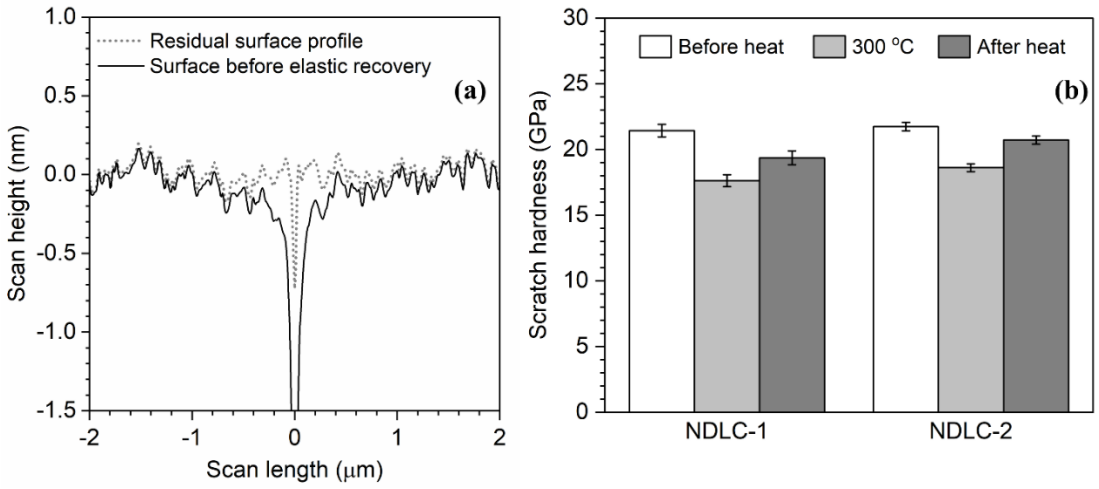

Figure 23**.** (a) Residual surface scan and in-situ (calculated) surface profile before elastic recovery, (b) Scratch hardness of NDLC-1 and NDLC-2 samples at 25 ºC before heating, 300 ºC and 25 ºC after heating. Error bars represent ± one standard deviation.

4.3.2.2. Coefficient of friction

Another set of nanoscratch experiments was performed to determine the coefficient of friction (COF) of the two films at different operational conditions. Normal and lateral forces were measured from nanoscratch experiments and COFs were determined by the ratio of lateral forces to normal forces. Figure 24(a) shows a typical COF response during a nanoscratch experiment. Average COFs for NDLC films (Figure 24(b)) were within the

range of 0.09 - 0.15 at 25 ^{o}C before heat treatment, which were in good agreement with values reported in DLC-related literature [81,82]. Bowden and Tabor [72] proposed a friction mechanism as a combination of two independent mechanisms: adhesion friction and deformation friction. The adhesion friction is due to van der Waals interactions resulting from surface roughness, interface surface energy, and elastic/plastic properties [36]. The deformation friction is due to plowing the softer surface by the asperities of a harder surface during sliding. The deformation COF (μ_{def}) can be determined using a simple analytical expression given by equation 7 [82,83],

$$\mu_{def} = \frac{4w}{3\pi r} \tag{7}$$

where, *w* is the in-situ scratch width, which is equivalent to the in-situ contact width calculated in nanoscratch experiments and *r* is the spherical radius of the indenter. In equation 3, it is assumed that normal force and lateral force act separately to yield the surface, which make μ_{def} independent of mechanical properties [83]. Using the results from the scratch tests, μ_{def} of NDLC films at all temperature conditions were found within the range of 0.1-0.12. Adhesion COF (μ_{adh}) can be determined by subtracting μ_{def} from the total COFs measured from the experiments. Comparing the COF results from Figure 24(b) with the results from equation (3), it was found that the average COF of both NDLCs at 25 ^{o}C before heating were almost the same and mostly attributed to deformation friction. Due to almost similar hardness of both NDLCs at 25 ^{o}C before heating, in-situ contact widths were similar during scratch tests, as indicated in Table 11, leading to similar

deformation COF. Adhesion COF components for both NDLCs were not significant before heating.

With increasing temperature to 300 ^{o}C, the COFs of both NDLCs increased more than 100%, increasing from 0.14 to 0.41 for NDLC-1 and from 0.13 to 0.26 for NDLC-2. The increases were attributed to significant increase of adhesion friction at 300 ^{o}C [15,82]. Notably, the increase in the COF was more dramatic for NDLC-1 at 300 ^{o}C, compared to NDLC-2. Interestingly, although NDLCs softened at 300 ^{o}C, the deformation friction did not significantly change according to equation (3). Molecular dynamics simulation showed that sp^2-hybridized carbon atoms undergo chemical reactions that can lead to adhesion between the diamond tip and NDLC surfaces. At 300 ^{o}C, the amount of hydrogen atoms on NDLCs decreased, which led to more sp^2-carbon atoms. At the same time, sp^3 to sp^2 carbon transformation also occurred at 300 ^{o}C. This change may provide more active sites on the surface of the NDLC, leading to higher adhesion between the diamond tip and NDLC surfaces at 300 ^{o}C [15,37,82].

After cooling down to 25 ^{o}C, the average COFs of NDLC-1 and NDLC-2 reduced to 0.24 and 0.20 respectively, which were still higher than the corresponding COFs before subjected to heat treatment. Softening of NDLCs due to higher percentage of sp^2/sp^3 ratios in both carbon and nitrogen after annealing may be the main cause for the obtained rise in COF. These findings were in agreement with the literature and the XPS results [34].

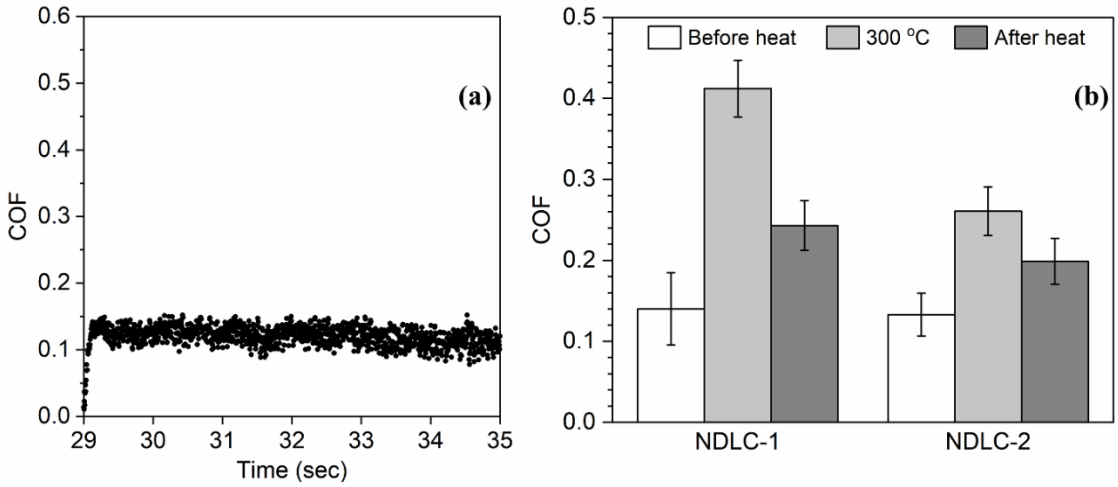

Figure 24. (a) Typical coefficient of friction (COF) response in a nanoscratch experiment; (b). Average COFs of NDLC samples at all three experimental conditions. Error bars represent ± one standard deviation.

4.3.3. Nanowear

Nanowear tests were carried out to study the wear mechanisms associated with NDLCs. After the experiments, residual surface scans with larger areas were obtained using scanning probe microscopy (SPM) technique. Figure 25 shows SPM images of residual NDLC surfaces after nanowear experiments at three experimental conditions: @ 25 ^{o}C before heat treatment, @ 300 ^{o}C, and @ 25 ^{o}C after heat treatment. The wear area showed a maximum depth of 0.70 nm and 0.66 nm for NDLC-1 and NDLC-2, respectively at 25 ^{o}C before subjecting to heat treatment process. The maximum depths increased to 1.7 nm and 1.1 nm for NDLC-1 and NDLC-2, respectively at 300 ^{o}C. Wear tracks were more clearly visible at 300 ^{o}C and the material pile-ups at the boundary of the wear tracks were obvious. The material pile-up was larger for NDLC-1 than for NDLC-2. After cooling down to 25 ^{o}C, the maximum wear depths for NDLC-1 and NDLC-2 were 0.80 nm and

0.70 nm, respectively. A comparison between samples before and after heat treatment shows that the obtained values at room temperature were higher after subjecting the samples to the heat treatment process. At all experimental conditions, NDLC-2 showed lower values of maximum depths than NDLC-1.

Wear experiments were performed 3 times at each experimental condition and average wear depths were calculated for both NDLCs as shown in Figure 26. Average wear depths for both NDLCs at 25 ^{o}C before heating were similar, with NDLC-2 having slightly less wear than NDLC-1. This is attributed to slightly higher hardness of NDLC-2 before heating than NDLC-1. Higher hardness gave NDLC-2 better resistance to permanent deformation, leading to better wear resistance. At 300 ^{o}C, the average wear depths of NDLC-1 and NDLC-2 increased to 0.76 nm and 0.57 nm respectively, showing more than 100% increase in wear. Increase in wear was attributed to reduction in sp^3 contents and increased adhesion, which were in agreement with Rose et al. [42] and the XPS results. NDLC-2 showed better wear resistance than NDLC-1 at 300 ^{o}C due to higher hardness and sp^3 carbon contents than NDLC-1. After cooling down to 25 ^{o}C, wear depths of NDLC-1 and NDLC-2 were found as 0.24 nm and 0.23 nm respectively, which were higher than 25 ^{o}C before heating. Similar to 25 ^{o}C before heating, wear depths of NDLC-2 were slightly lower than NDLC-1 after heat treatment due to higher hardness of NDLC-2 than NDLC-1. Interestingly, none of the NDLCs showed any delamination even at 300 ^{o}C and maximum average wear depths were found less than 1 nm for both NDLCs, indicating that both NDLCs were able to protect the substrate from direct contact with the indenter.

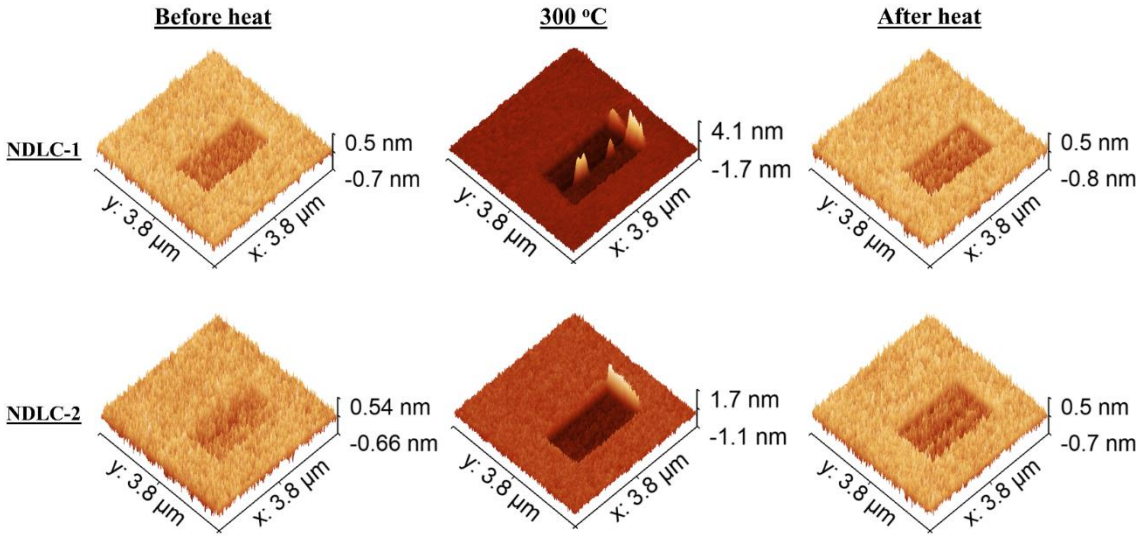

Figure 25. Residual surface profiles of NDLC samples after nanowear tests at 25 °C before heating, 300 °C and 25 °C after heating.

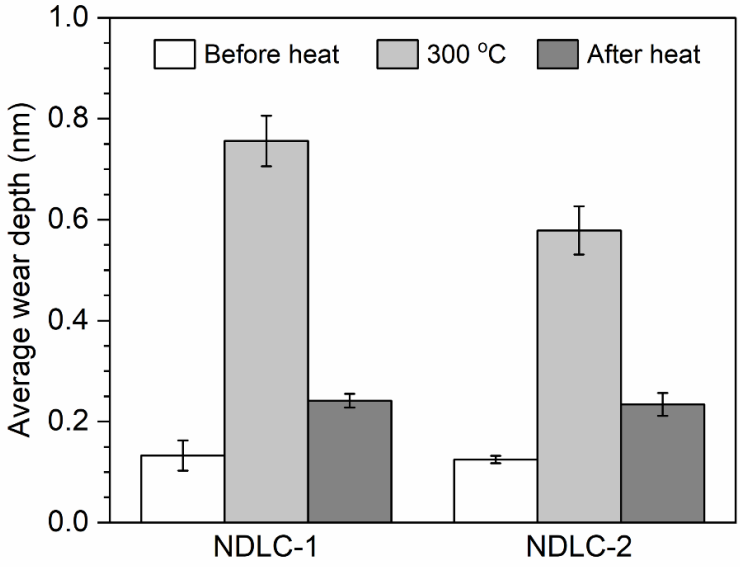

Figure 26. Average wear depths of NDLCs at 25 °C before heating, 300 °C and 25 °C after heating. Error bars designate ± one standard deviation.

4.3.4. Effect of heat treatment on surface roughness

Tapping mode AFM was used for the roughness measurements with a scan area of 4.8 µm 4.8 µm. Figure 27 shows surface scans of NDLC-1 and NDLC-2 samples for two experimental conditions: before and after annealing at 25 ^{o}C. The measurements showed that RMS surface roughness (R_q) of NDLC-1 and NDLC-2 subjected to different experimental conditions were within the same range of 0.09-0.12 nm, indicating that surface roughness remained almost the same after heat treatment. This indicates that the NDLCs are robust samples and can be at least used up to 300 ^{o}C without serious damage.

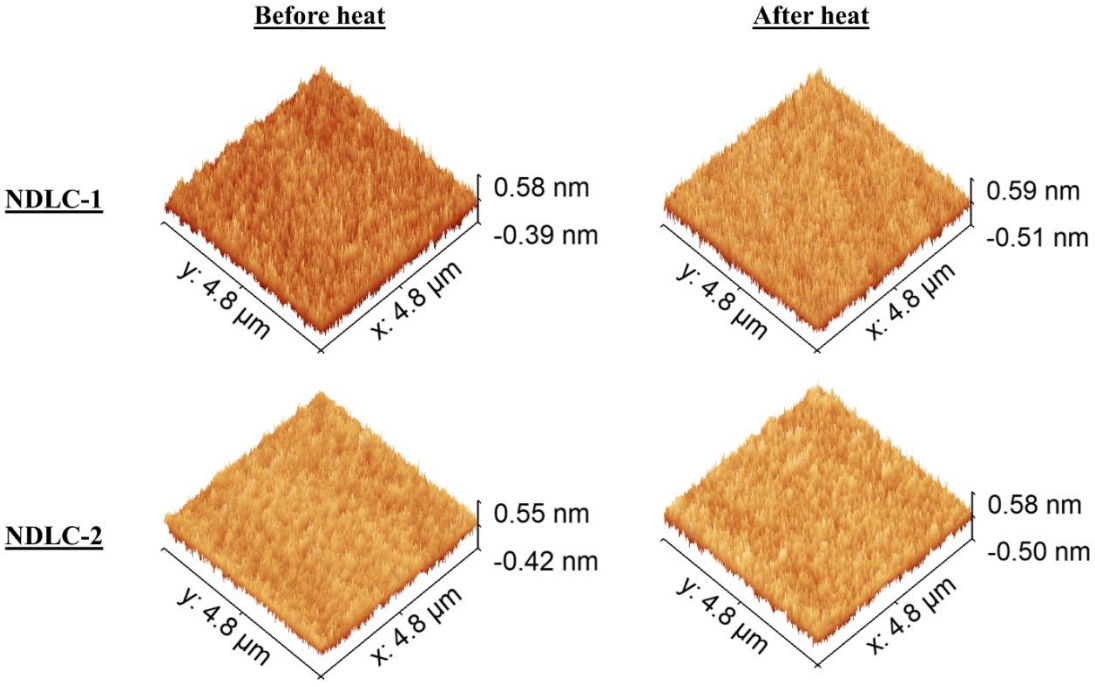

Figure 27. AFM Surface scans of NDLC-1 and NDLC-2 at 25 ^{o}C before heating and 25 ^{o}C after heating.

4.4. Summary

Mechanical and tribological studies were performed for ultra-thin NDLC films with different sp^2/sp^3 carbon ratios and almost the same nitrogen content, which were determined from XPS study. Hardness, COF, and wear were measured and compared for the NDLC films at 25 ^oC before and after heat treatment, and at high temperature of 300 ^oC. The following conclusions can be drawn:

1. The XPS studies showed that sp^2/sp^3 carbon ratios of NDLC increases after subjecting samples to a heat treatment process at 300 ^oC;
2. NDLC-2 with lower sp^2/sp^3 carbon ratios showed better mechano-tribological properties e.g., hardness, COF, and wear. At 300 ^oC, the hardness of NDLCs decreased due to softening and reduction in sp^3 carbon and nitrogen contents. After cooling back to 25 ^oC, the hardness of NDLCs reduced, compared to the original film before heating, which is attributed to changes in sp^2/sp^3 ratio;
3. Because of heat treatment, adhesive friction of both NDLCs samples increased significantly due to increased sp^2 carbon and nitrogen contents, leading to more than 100% increase in overall COFs, compared to before heat treatment. After annealing, COFs of NDLCs were also higher than before heat treatment as a result of graphitization. NDLC-2 having lower sp^2/sp^3 ratio showed lower COF than NDLC-1 at both 300 ^oC, and after heat treatment;
4. NDLC-2 with lower sp^2/sp^3 carbon ratio showed better wear performance than NDLC-1 with higher sp^2/sp^3 ratio. Wear resistance deteriorated at 300 ^oC due to softening and increased adhesion of NDLCs. Higher hardness led to increased

resistance to permanent deformation, resulting in better wear performance. After heat treatment, wear behavior was predominantly recovered to before heating values; and

5. Although NDLC-2 having lower sp^2/sp^3 carbon ratio showed better wear performance than NDLC-1, none of the NDLCs were delaminated and maximum values of wear depths were less than the thickness of the coatings, i.e., 1 nm. This indicated that both NDLCs were able to protect the substrate from direct content, especially at high temperature conditions.

This chapter concludes solid-solid contact studies for hard coatings. NDLCs did not show creep behavior at higher temperature due to higher strength. If one of the contact surfaces is softer, creep behavior may be observed at elevated temperatures. In the next chapter, a state-of-the-art bionanocomposite thin film system has been chosen for solid-solid contact study for soft coatings, and creep behavior of the composite was studied at elevated temperatures.

CHAPTER V

ELEVATED TEMPERATURE MECHANICAL AND CREEP BEHAVIOR OF GRAPHENE OXIDE, SILK FIBROIN AND CELLULOSE NANOCRYSTALS BIO NANOCOMPOSITE FILMS

5.1. Introduction

Ultra-thin nanobiofilms are widely considered as potential functional materials for various state-of-the art applications e.g., flexible electronic devices, thermal interface materials, energy storage, and lubricants due to their outstanding mechanical properties [84–86]. Especially, nacre-like biopolymer films with distinctive laminated structure exhibited superior mechanical properties [87,88]. These improvements in mechanical properties compared to their constituent components were attributed to the brick-and-mortar structure of the films [89,90]. Among the potential constituent materials, two-dimensional (2D) graphene oxide (GO) film is a well-known candidate due to its superior mechanical properties, electrical conductivity after reduction, and better optical properties [91] . However, the assembled GO films do not show the same mechanical behavior as GO flakes because of debonding and delamination, limiting their usage in practical applications [92,93].

To improve the mechanical properties of GO-based films, suitable materials must be assembled with GO to form nacre-like structures. Several materials have caught researchers' attention to develop GO-based nanofilms. Silk fibroin (SF) is one of the promising materials with suitable mechanical properties. SF can be easily fabricated from

natural silk cocoons, which makes the nacre structure having biocompatibility [94]. At the same time, SF also showed better interfacial and adhesion strength with GO films [95]. Previous studies showed that GO-SF nanocomposite exhibited superior mechanical properties, compared to individual components [88,96]. On the other hand, cellulose nanocrystals (CNC) is also another candidate material for GO-based bionanofilms. CNC also showed better mechanical integrity, high aspect ratio and the mechanical behavior was also improved when assembled to form GO-CNC nanocomposite [13,97,98]. CNC also exhibited improvement in mechanical performances when assembled with SF due to hydrogen bonding and increased interfacial interactions [99]. Therefore, GO-SF-CNC assembled nacre like composite is expected to significantly improve mechanical properties compared to other bionanofilms. Several fabrication methods have been implemented to fabricate nacre-like structures with tunable mechanical properties. Spin assisted layer-by-layer (SA-LbL) assembly is one of the most popular methods to fabricate the nacre like composites with their thicknesses at the nanoscale [96,100].

Creep behavior of bionanofilms is of great importance as they will be subjected to longer time exposure to heat and/or applied load. Several researchers have worked on temperature dependent and viscoelastic behavior of individual GO, SF and CNC materials [10–13]. However, the literature is limited for temperature dependent and creep behavior of GO-SF-CNC nanocomposite to ensure mechanical reliability for real life applications. Nanoindentation technique is a widely used method to determine mechanical properties of thin films, including at elevated temperatures. The same technique can be used to perform creep experiments of a material by holding the maximum load for sufficiently

longer time to determine creep displacements. This method is commonly known as constant load hold (CLH) method. To predict creep properties from the experiments, different approaches have been used in the literature. Finite element analysis (FEA) is one of the widely used methods to determine creep properties of a material by curve fitting nanoindentation load-displacement responses [101]. For predicting true properties of thin films from nanoindentation and FEA, the indenter geometry is also an important factor and needs to be considered in FEA [43,54].

In this study, GO-SF-CNC nanocomposite films were fabricated using SA-LbL method and nanoindentation creep experiments were performed to investigate mechanical and creep behavior of GO-SF-CNC nanocomposite at different temperature conditions. Finite element method was also performed in this study using modified indenter geometry to investigate creep properties of the nanocomposite.

5.2. Experimental

5.2.1. Preparation of the nanocomposites

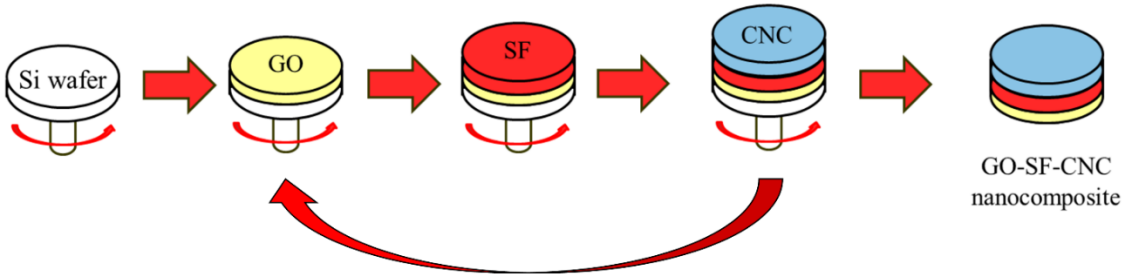

Figure 28. Schematic representation of SA- LbL method to fabricate GO-SF-CNC nanocomposite.

GO, SF and CNC were prepared using separate methods and SA-LbL was used to fabricate GO-SF-CNC nanocomposite. Figure 28 shows a schematic representation of SA-LbL process used for GO-SF-CNC fabrication. GO component was prepared using Hummer's method [102,103]. In this method, the graphite powder was first oxidized using sulfuric acid, potassium permanganate and sodium nitrate. After that, the oxidized solution was slowly quenched with de-ionized water and heated for 2 hours at 95 ^{o}C. The solution was then cooled down to room temperature, and de-ionized water and hydrogen peroxide were added to the solution. The solution was stirred for an hour after the addition of each component. Then the solution was sedimented for 6 hours, and the process was repeated multiple times. After that, the sedimented solution was percolated and finally GO was obtained after heating at 60 ^{o}C. SF solution was obtained from Bombyx mori silkworm cocoons. At first, the cocoon was degummed and dissolved using sodium sulfate solutions of two different concentrations. Then the solution was dialyzed using de-ionized water and then centrifuged twice at 9000 rpm for 10 minutes to remove the supernatant and

obtain the SF solution [104]. Cellulose nanocrystals were fabricated from microcrystalline cellulose (MCC). At first, the MCC was hydrolyzed using sulfuric acid and then the solution was quenched using de-ionized water. After that, the quenched solution was centrifuged multiple times at 10000 rpm for 10 minutes using de-ionized water and then it was dialyzed for 2-3 days. The dialyzed solution was then sonicated and again centrifuged at 5000 rpm for 5 minutes to obtain CNC suspensions [105].

SA-LbL method was used to fabricate GO-SF-CNC nanocomposites. During the SA-LbL process, all three components were dispersed in de-ionized water and then the solutions were alternatively deposited on a silicon substrate until desired thickness was obtained. The SA-LbL process was performed at 3000 rpm to obtain very thin GO-SF-CNC nanocomposite films. In this study, GO-SF-CNC nanocomposite film with a thickness of 180 nm was deposited on a silicon substrate.

5.2.2. Nanomechanical experiments

Nanoindentation creep experiments with longer dwell times were performed to determine mechanical and creep properties of GO-SF-CNC nanocomposite. The load function used for the nanoindentation tests is shown in Figure 29. The steps for the nanoindentation tests involve loading to a maximum load in 5 seconds, holding the maximum load for 30 seconds to obtain the creep displacement, unloading to 1 μN in 5 seconds, holding 1 μN for 30 seconds to obtain viscoelastic recovery and final unloading. Five different temperature conditions were used to investigate temperature dependent mechanical and creep behavior -25 ^{o}C, 40 ^{o}C, 60 ^{o}C, 80 ^{o}C and 100 ^{o}C. Nanoindentation tests were

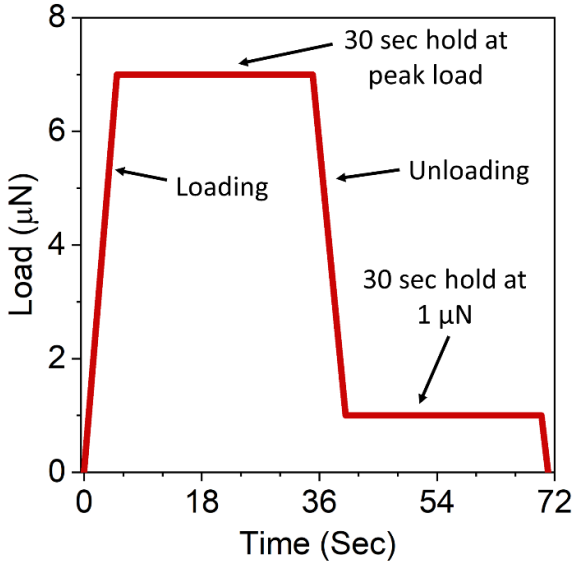

Figure 29. Load function for nanoindentation creep study.

repeated three times at each temperature conditions to ensure repeatability. For all experiments, 7 µN was chosen as the maximum normal load to maintain the maximum displacement within 10-15% of the film thicknesses, to avoid any substrate effect from silicon. A very sharp cube corner indenter with a tip radius of 80 nm was used to initiate plastic deformation at minimal displacements. Shallow indentations were performed to avoid substrate effect and because of that, the maximum displacements were within the spherical shape of the cube corner indenter. The drift rate was calculated before starting the experiments by holding the indenter on the sample for 40 seconds under minimal load. The drift rates were found within 0-0.1 nm/s for all temperature conditions.

The Oliver-Pharr [18] method is widely used to determine hardness and elastic modulus from the nanoindentation experiments, given by equations (1-3). Feng et. al [106] suggested a correction to Oliver-Pharr method to reduce creep effect, especially for

reduced modulus calculations at high temperatures. They proposed a modified unloading stiffness S_m, given by equation (8)

$$\frac{1}{S_m} = \frac{1}{S} + \frac{\dot{h}_h^c}{|\dot{P}|} \tag{8}$$

where, $\dot{h}_h^c$ is the creep rate at the end of the load hold stage and $\dot{P}$ is the unloading rate at the beginning of the unloading. In this study, S_m was used instead of S in equations (1-3) to calculate the hardness and reduced modulus at different temperature conditions. Nanoindentation experiments were also performed to determine the hardness and reduced modulus of the bare silicon substrate using a trapezoidal load function and equations (1-3). More details of the experiments are discussed in the Appendix C. Results were entered into the FEA model (section 5.3.1) to determine the yield strength and creep properties of the GO-SF-CNC nanocomposite.

5.3. Finite element modeling for creep study

5.3.1. Model description

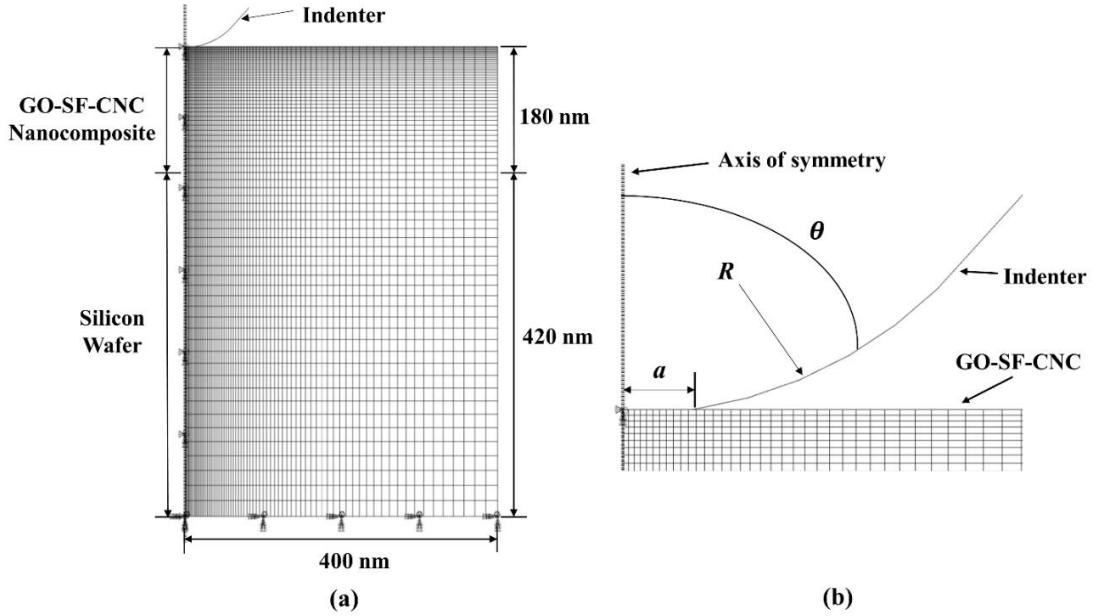

Figure 30. (a) Schematic of the finite element model to predict creep properties of GO-SF-CNC, (b) zoom-in view of the model to show the indenter geometry and surface elements.

Figure 30(a) shows the finite element model used in this study to predict yield strength and creep properties of GO-SF-CNC nanocomposite by simulating the experimental responses. The GO-SF-CNC nanocomposite was considered as a single material in the FEA model to predict the overall mechanical and creep behavior. A 2D axisymmetric model was built for reduced computational complexities using ABAQUS 6.14 software. The cube corner indenter was modeled as an analytic rigid surface. The bottom of the indenter was modeled as flat, along with spherical geometry as shown in Figure 30(b). In the figure, 'a' is the flat part length of the indenter, 'R' is the radius of the indenter and 'θ' is the effective cone angle. The model sample consisted of GO-SF-CNC nanocomposite layer of 180 nm and silicon substrate of 320 nm thickness. Mechanical

properties of silicon substrate were entered into the FEA model, which were determined from separate nanoindentation experiments on bare silicon substrate (see Appendix E). The width of the model sample was 400 nm. 5775 linear quadrilateral reduced integration elements (CAX4R) were used to build the model sample. The minimum element area was 1×1 nm^2, used for GO-SF-CNC layer and the maximum element area was 15×20 nm^2, used for the silicon wafer. Heavy mesh was used for the region closer to the indenter. The strain-stress response of the sample was assumed as elastic-viscoelastic-plastic. Von-mises criterion was used to simulate mechanical behavior of both GO-SF-CNC and silicon wafer. The axis of symmetry was constrained for rotations and lateral movements; and the bottom surface of the sample was constrained for rotations and vertical movements. Following the work from Zhang et al. and Shakil et al. [43,54], the flat part length (a) was determined to be 12.5 nm for the indenter radius (R) of 80 nm. More details of the indenter geometry determination and model validation are discussed in the Appendix D.

5.3.2. Two-layer viscoplasticity theory for creep

Two-layer viscoplasticity theory has been adopted in this study to investigate creep behavior of GO-SF-CNC nanocomposite material at different temperature conditions. The model can be used for polymers when they show plastic deformation for any specific loading conditions, along with viscoelasticity [107,108]. The theory is available as a built-in material model in the ABAQUS software. Figure 31 shows one dimensional idealization of the two-layer viscoplasticity model. The model consists of an elastic-plastic network and a viscoelastic network, both in parallel with each other as shown in Figure

31. K_p and K_v are elastic modulus of elastic-plastic and viscoelastic network, respectively. σ_y and *H'* are yield strength and hardening coefficient of the material, respectively. Another parameter, *'f'* is also defined as the ratio of elastic modulus of viscoelastic network (K_v) to the instantaneous elastic modulus of the material, $E = K_p + K_v$, shown in equation (9).

$$f = \frac{K_v}{K_p + K_v} = \frac{K_v}{E} \tag{9}$$

In this model, viscous or creep behavior is defined by Norton-Hoff equation below

$$\dot{\varepsilon}_v = A{\sigma_v}^n \tag{10}$$

Where, $\dot{\varepsilon}_v$ and σ_v are the creep strain rate and creep stress, respectively. ***A*** and ***n*** represent creep coefficient and creep exponent respectively for the material under study.

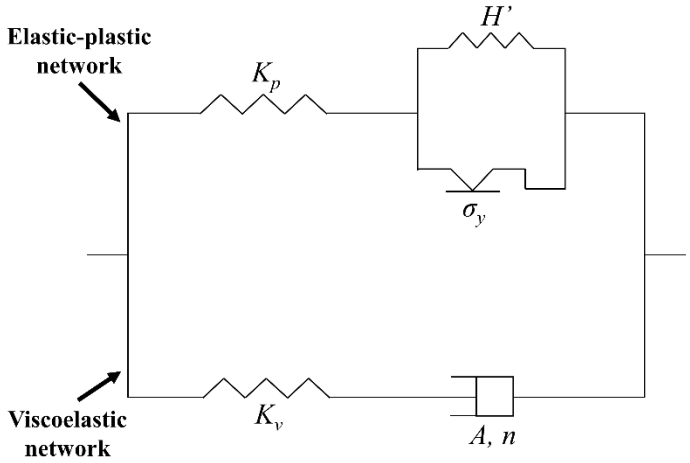

Figure 31. One-dimensional idealization of the two-layer viscoplasticity model.

For GO-SF-CNC nanocomposite, the elastic-perfectly plastic behavior without any hardening was assumed in this study, i.e., ***H'= 0***. Elastic modulus values of the

nanocomposite, determined from nanoindentation creep experiments, were entered in the finite element model and simulations were performed to curve fit the experimental responses to obtain $\boldsymbol{\sigma_y}$, $\boldsymbol{n}$ and $\boldsymbol{f}$ at different temperature conditions. After that, σ_y was compared with hardness (H) of the nanocomposite to investigate hardness to yield strength ratio (H/σ_y) at different temperature conditions.

5.4. Results and discussion

5.4.1. Hardness and elastic modulus from nanoindentation experiments

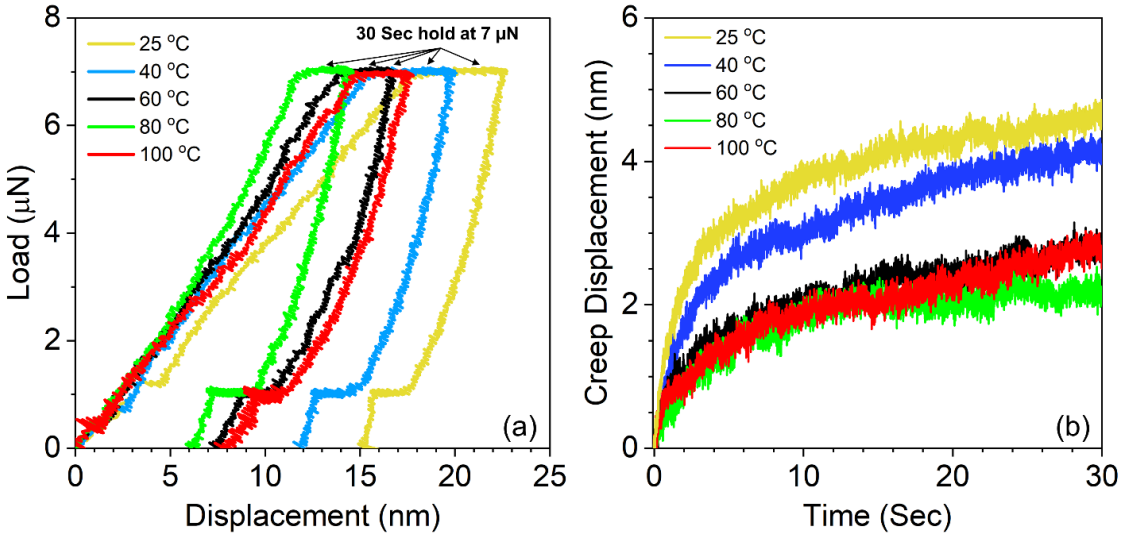

Figure 32. (a) Nanoindentation load-displacement responses for creep study of GO-SF-CNC at different temperatures, (b) Creep displacement for 30 seconds hold at 7 µN peak load at different temperature conditions.

Figure 32(a) depicts nanoindentation load-displacement responses of GO-SF-CNC samples at different temperature conditions of 25 °C, 40 °C, 60 °C, 80 °C and 100 °C. From Figure 32(a), it was evident that GO-SF-CNC underwent noticeable displacements due to creep during constant load hold at 7 µN for 30 seconds. Creep displacements at different temperatures for 30 seconds load hold was determined from the experiments and shown

in Figure 32(b). From Figure 32(a), it was found that the maximum displacement during nanoindentation tests was higher at 25 ^{o}C and then it gradually decreased with increasing the temperatures up to 80 ^{o}C. At 100 ^{o}C, the maximum displacement increased from that at 80 ^{o}C. From Figure 32(b), similar trend was found for creep displacements, which also contributed to maximum displacements during nanoindentation tests. Creep displacement of GO-SF-CNC after 30 seconds load hold was also higher at 25 ^{o}C and then it gradually decreased with increasing temperature up to 80 ^{o}C. Again at 100 ^{o}C, the creep displacement started increasing from that at 80 ^{o}C. During unloading stages, the sample was again held at lower load (1 μN) for 30 seconds to allow viscoelastic recovery for GO-SF-CNC before fully unloading. Like maximum and creep displacements, the permanent deformation after fully unloading was also higher at 25 ^{o}C and then gradually decreased with increasing temperature up to 80 ^{o}C and then it again increased at 100 ^{o}C.

Hardness and reduced modulus of GO-SF-CNC were determined from the experimental responses using equations (1-3,8). Figures 33(a) and 33(b) show summary results of hardness and reduced modulus respectively for all five temperature conditions. From the figures, it was evident that hardness and reduced modulus of GO-SF-CNC increased with increasing temperatures from 25 ^{o}C to 80 ^{o}C. This increase in mechanical properties was attributed to crystallization of SF and CNC components. Heat treatment at elevated temperatures increased the formation of β-sheet SF nanocrystals, which contributed to increase in mechanical properties with temperature [11,109]. At the same time, the presence of GO in the nanocomposite also enhanced silk crystal formations due to increased interfacial interactions between GO and SF than pure SF only [88]. Crystallinity

of CNC also increased with increasing the temperature, while at the same time, the amount of water molecules absorbed in CNC via hydrogen bonding also decreased, both leading to increase of mechanical properties of GO-SF-CNC nanocomposite [10,110]. GO does not undergo thermal decomposition until it reaches a temperature of 220 ^{o}C [12], which implies that mechanical properties of GO were not significantly affected within the range of 25 ^{o}C to 100 ^{o}C. Increase in reduced modulus due to crystallization also implied increase in reduced modulus of viscoelastic component, thereby showing reduction in creep displacement for 30 seconds hold under the maximum load.

However, at 100 ^{o}C, both hardness and reduced modulus of GO-SF-CNC deteriorated. It was attributed to evaporation of water molecules from the nanocomposite, making them softer [111]. Also, longer exposure to heat can cause thermal degradation of the nanocomposite components, which might also lead to reduction in mechanical properties [88]. Because of reduction in mechanical properties at 100 ^{o}C, GO-SF-CNC showed increased creep displacements. The average hardness of GO-SF-CNC increased from 0.6 GPa at 25 ^{o}C to 1.27 GPa at 80 ^{o}C, showing 112% increase in hardness. However, the average hardness value dropped to 1 GPa at 100 ^{o}C, which is 21% reduction in hardness after heating from 80 ^{o}C to 100 ^{o}C. Similarly, the average reduced modulus of GO-SF-CNC increased from 13.0 GPa at 25 ^{o}C to 19.25 GPa at 80 ^{o}C (48% increase) and again decreased to 15.6 GPa at 100 ^{o}C (19% decrease) due to heating from 80 ^{o}C to 100 ^{o}C. Because of crystallization effects, creep displacements (Figure 32(b)) after load hold for 30 seconds reduced from 4.7 nm at 25 ^{o}C to 2.2 nm at 80 ^{o}C, which was 53% reduction in

creep displacements. At 100 ^{o}C, the creep displacement again increased to 2.85 nm, showing 29% increase because of heating from 80 ^{o}C to 100 ^{o}C.

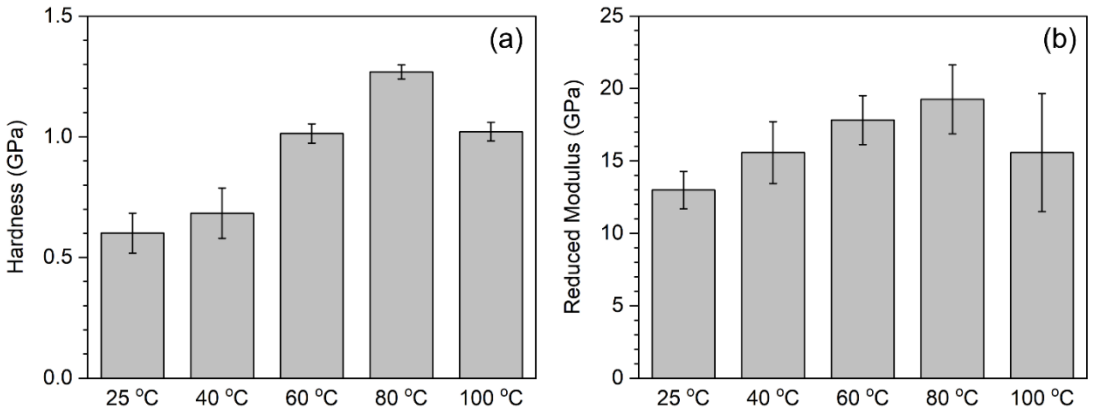

Figure 33. Summary of (a) hardness and (b) reduced modulus of GO-SF-CNC from nanoindentation experiments at different temperature conditions. Error bars represent ± 1 standard deviation.

5.4.2. Yield strength and creep exponent values from FEA

Nanoindentation load-displacement responses, along with creep displacements during load hold stages were fitted with FEA to determine yield strength and creep exponent of GO-SF-CNC at different temperature conditions. Elastic modulus of GO-SF-CNC from nanoindentation experiments were entered into FEA for curve fitting. Figure 34 shows FEA fitted nanoindentation load-displacement and creep displacement responses at 25 ^{o}C. Summary of FEA predicted yield strengths and creep exponents at different temperature conditions are shown in Figure 35. Like hardness and reduced modulus, yield strength also increased with increasing the temperature up to 80 ^{o}C, due to increased crystallization of SF and CNC components as discussed in section 4.1. After reaching 100 ^{o}C, the yield strength decreased from its maximum value at 80 ^{o}C due to evaporation of water from the

nanocomposite, making them softer. Specifically, yield strength increased from 0.29 GPa at 25 ^{o}C to 0.7 GPa at 80 ^{o}C, showing 140% increase. At 100 ^{o}C, yield strength reduced to 0.56 GPa, which is a 20% reduction due to heating up to 100 ^{o}C.

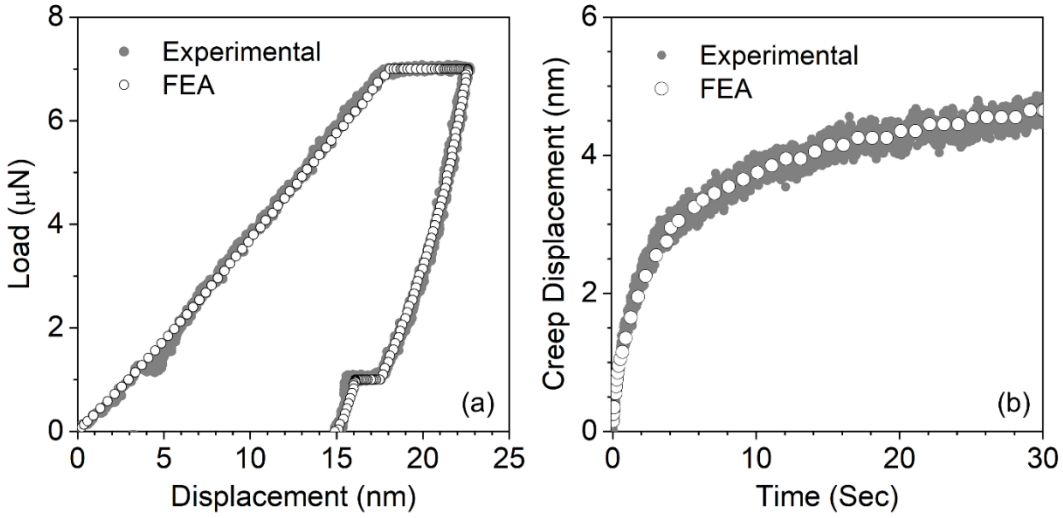

Figure 34. FEA curve fitting of (a) nanoindentation load-displacement response and (b) creep displacement response of GO-SF-CNC at 25 ^{o}C.

Average values of creep exponents predicted from FEA at 25 ^{o}C and 40 ^{o}C were 2.82 and 2.9 respectively, showing a slight increase that may be attributed to increased mobility of atoms with temperature. However, when the temperature further increased to 60 ^{o}C, crystallization of SF and CNC components dominated the behavior, and the creep exponent reduced to 2.22 at 60 ^{o}C. At 80 ^{o}C, the creep exponent further decreased to 2.03, which was the minimum value within the temperature range. At 100 ^{o}C, the creep exponent again increased to 2.27, due to weakening of the nanocomposite because of water evaporation.

The ratio of elastic modulus of the elastic-viscoelastic network to the instantaneous elastic modulus (*f*) was also predicted from FEA and found within the range of 0.62-0.71 with no

significant dependence on temperature. Using hardness results from the experiments and yield strength results from FEA, hardness to yield strength ratios (H/σ_y) were calculated and found within the range of 1.84-2.06 for the temperature conditions. No significant trend of H/σ_y ratio with temperature was observed.

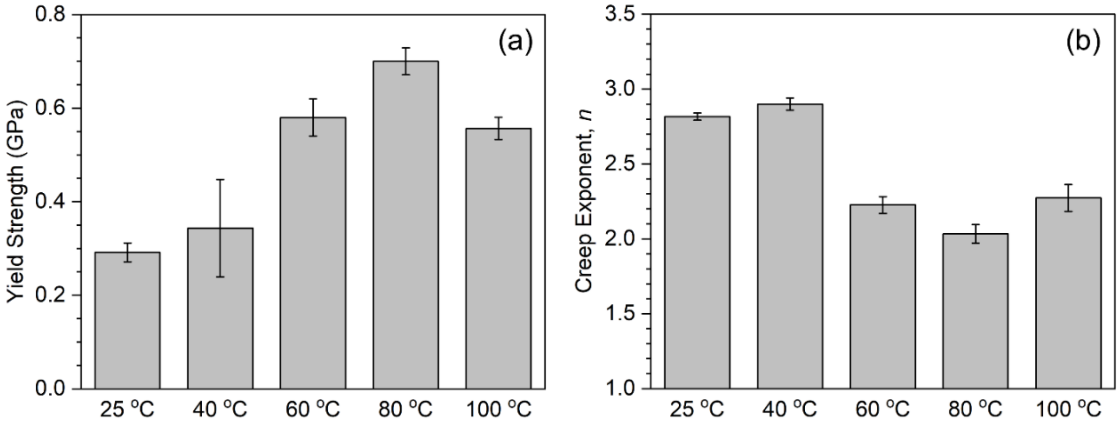

Figure 35. FEA predicted (a) yield strength and (b) creep exponent results of GO-SF-CNC at different temperature conditions.

5.5. Summary

Nanoindentation creep experiments at different temperatures using constant load hold method has been performed to investigate mechanical and creep behavior of state-of-the-art graphene oxide (GO), silk fibroin (SF) and cellulose nanocrystals (CNC) nanocomposite thin films. Results of the study can be summarized as follows:

(a) Because of increase in crystallizations of silk fibroin and cellulose nanocrystals, hardness and reduced modulus values increased with increasing the temperature from 25 °C to 80 °C. Because of increase of mechanical properties, creep displacements during load hold stage showed a decreasing trend with increasing

temperature up to 80 ^{o}C. However, hardness and reduced modulus deteriorated at 100 ^{o}C due to water evaporation from the composite, and at the same time creep displacement also increased due to water evaporation and thermal degradation at 100 ^{o}C;

(b) Finite element results showed that yield strength of the GO-SF-CNC followed the same behavior as hardness and reduced modulus, i.e., increase of yield strength with increase in temperature up to 80 ^{o}C and then deterioration at 100 ^{o}C. Hardness to yield strength ratio values (H/σ_y) were found within the range of 1.84 - 2.06 for all temperature conditions investigated in this work; and

(c) Although creep exponent (n) predicted from FEA slightly increased at 40 ^{o}C, it then decreased significantly from 2.9 to 2.06 with further increase in temperature from 40 ^{o}C to 80 ^{o}C. After that, creep exponent again increased to 2.27 due to weakening of the GO-SF-CNC structure at 100 ^{o}C.

The above properties make GO-SF-CNC a potential nanocomposite material for several applications, e.g., flexible electronics, thermal interface materials, energy storage etc. where long term exposure to different temperatures might be critical.

This study concludes the mechanical and tribological studies of solid-solid dry contacts for thin film systems. The interfacial forces between the surfaces can be significantly affected by a third material if present between contacting surfaces. Surface haptics is such an application, where sweat and moisture contents of human fingertip can affect the adhesion between the fingertip and the haptics surface when they are in contact. In the

next chapter, theoretical modeling has been performed to investigate interfacial forces between this solid-liquid contact system.

CHAPTER VI

AN IMPROVED ELECTROADHESION MODEL FOR HAPTICS APPLICATIONS CONSIDERING MENISCUS AND ROUGHNESS EFFECTS

6.1. Introduction

Surface haptics is becoming a more popular field of study now-a-days partly due to the widespread use of smart devices. This technology involves human finger touch, which increases the interactions of human fingers with a device. Figures 36(a) and 36(b) show a schematic representation of a human finger-haptics device interaction and zoomed-in view of the contact region (not in scale). Surface haptic surfaces typically consists of an electroadhesion coating on nanotextured glass substrate surface. the coating consists of three major components-an electroadhesion layer, a dielectric layer, and a conductive layer. Indium Tin Oxide (ITO) layer and substrate. The human fingertip is rubbed against the electroadhesion layer and the dielectric layer. Voltage is supplied through the conductive layer for tactile sensation, which is on top of the glass substrate. Typical dielectric materials are, silicon dioxide, PDMS etc. typical conductive materials are Indium Tin Oxide (ITO), poly(3,4-ethylenedioxythiophene) polystyrene sulfonate (PEDOT/PSS) etc.

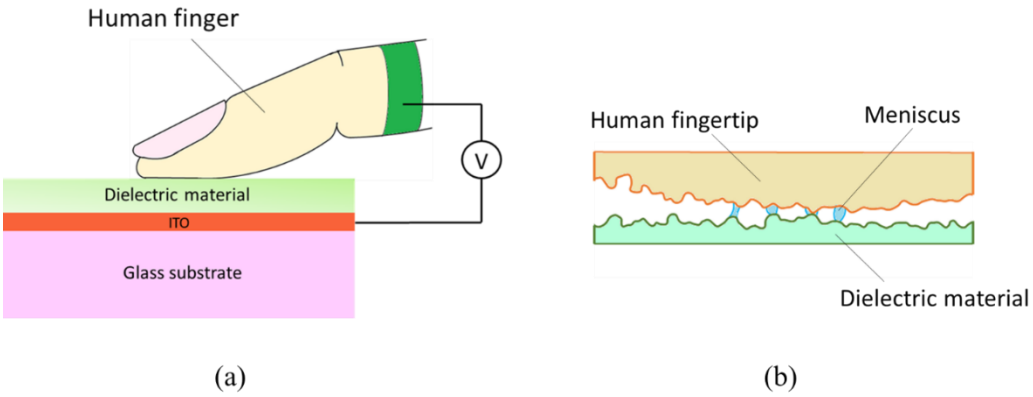

Figure 36. (a) Schematic representation of human finger and haptics surface interaction, (b) zoomed-in view to show microscopic contact under meniscus action

Haptic devices use electric field to sense the fingertip surface, which also can influence the contact performance. Adhesion between the contact surfaces is a combination of several interfacial forces. Vaan Der Waals force acts between the fingertip and haptics surface when they come sufficiently close to each other. As electric field is applied during the application, an electrostatic force is also induced in between the surfaces. It is well known as electroadhesion as the adhesion is induced by application of an electrical voltage and thus an electrostatic force. Due to moisture content in the environment, perspiration (sweat), sebum etc. from human fingertips, menisci form between the surfaces and meniscus forces (due to Laplace pressure) also contribute to electroadhesion [14]. After applying an electric voltage, meniscus contact angles significantly change, and meniscus forces also change. This increases wettability of the dielectric of haptics surface, which is widely known as electrowetting on-dielectric (EWOD) [112–114]. The change in meniscus forces also affects the electrostatic force, indicating that meniscus formation and electrostatic force are not simultaneous. To predict adhesion forces between fingertips and

haptics surfaces, all interfacial forces mentioned above need to be considered and their individual contribution to overall performance are of great importance.

Several modeling approaches have been adopted to investigate electroadhesion of haptics applications. Ivan et al. [115] considered the fingertip as a spherical asperity and investigated adhesion and friction forces at the macro scale. However, meniscus and roughness effects were not considered in the model. Xinyi et al. [116] investigated interfacial forces for a single asperity of the dielectric material by assuming a trapezoidal geometry and interfacial forces were predicted considering meniscus effects.

Roughness of the contact surfaces can also significantly affect electroadhesion and surface characteristics also need to be taken into account for accurate predictions of adhesion forces. However, such studies on haptics devices are not abundant in literature. Therefore, the objective of this study is to develop a model to predict overall adhesion forces between the fingertip and haptics surface by considering all interfacial forces acting between them, along with surface properties of the surfaces, e.g., roughness, surface asperity height distributions, asperity radius etc.

Greenwood-Williamson (GW)-type statistical model [117] is widely used to incorporate roughness effect with single asperity models with different contact conditions. Several meniscus models have been proposed before to investigate adhesion forces by considering roughness and humidity effects [118–120]. However, these models were oversimplified and did not consider deformation of the asperities due to meniscus forces.

Maugis first proposed a single asperity adhesion model by considering a constant stress at the Dugdale zone outside of the contact area. The model is well known as Maugis-Dugdale

(MD) model [121]. Shi and Polycarpou [122] extended the MD model and proposed the Extended Maugis-Dugdale (EMD) model to predict full range dry adhesion, from noncontact to just-contact to elastic and then plastic contact. In their model, both contacting and noncontacting asperities were considered to predict adhesion assuming Dugdale stress distribution. Literature shows that Laplace pressure due to meniscus effects can be considered as a Dugdale stress [121,123]. Xue and Polycarpou [124] proposed a meniscus model including roughness effects by taking Laplace pressure as Dugdale stress and incorporating them into the EMD model. The model also considers spherical deformation of both contacting and noncontacting asperities.

In this study, an improved electroadhesion model for haptics is proposed by incorporating the electrostatic effect into the model proposed by Xue et al. In this study, contact angles with human fingertip and dielectric surface were separately considered and contact angles after electrostatic effect were also calculated to predict meniscus forces before and after applying voltage.

6.2. Sample description and properties

For predictions of interfacial forces, surface characteristics and mechanical properties of contact surfaces need to be determined. In this study, a haptics glass sample was considered with the coating consisting of 1 μm of silicon dioxide layer used as dielectric, followed by 30 nm ITO layer on top of the glass substrate (Figure 36(a)), taken from [116]. Mechanical and electrical parameters for both human fingertip and haptics glass were taken from literature and shown in Table 12. Literature shows that human fingertip has a

wavy pattern with a wavelength of approximately 567 μm and an amplitude of approximately 42 μm [125]. Which means that curvature of the human skin may affect the interfacial forces calculations. For a single asperity study, the fingertip surface can easily be considered as a flat surface, since the asperity radius is much smaller compared to wavelength of the fingertip ridge. Similar approach was found from literature [116].

Table 12. Mechanical, electrical, and contact parameters used in this study

Parameter	Value	Reference
Contact angle on dielectric surface	108^{o}	[116]
Contact angle on human fingertip	80^{o}	[126]
Elastic modulus of asperity on dielectric surface (GPa)	70	[116]
Poisson's ratio of dielectric	0.3	[116]
Elastic modulus of skin (MPa)	50	[127]
Poisson's ratio of skin	0.4	[116]
Dielectric constant of dielectric surface	3.8	[116]
Dielectric constant of human fingertip	1000	[128]
Dielectric constant of water	80	[116]

6.3. Improved single asperity electroadhesion model

Two rough surfaces in contact can be modeled as the contact between a flat rigid surface and an equivalent rough surface. The equivalency is geometry dependent and is valid as the asperity radii are large compared to their height surface roughness (of the order of 3 orders of magnitude difference). Due to sweat, sebum and moisture content of human fingertips, meniscus can form around the asperities of the haptic surface. The adhesion forces and contact loads between the two surfaces can be determined by integrating the

contribution from each asperity. The asperity can be considered as a deformable sphere of radius *R* which is in contact with a flat rigid surface.

In classical meniscus adhesion models, the meniscus formation was assumed due to capillary condensation from the environment and can be related to relative humidity of the environment. However, the human fingertip also contains sweat, sebum etc. Therefore, the liquid volume in the human fingertip-haptics interface consists of human perspiration and capillary condensation. For an average human finger sweat rate of about 0.5 ~ 1 mg cm^{-2} min^{-1} [129] and a typical sliding speed of 50 ~ 150 mm s^{-1} on touchscreens for a fingertip of ~10 mm in width, the liquid volume from human perspiration can be estimated as 0.12 ~ 0.67 μm^3 for one asperity [116]. Also considering the capillary condensation, the thickness of meniscus film can be found as 0.28 ~ 1.84 nm from Kelvin equation for 15%~ 75% relative humidity [116]. Following the work from [116], the total water volume of 0.1 ~ 0.8 μm^3 was considered for the single asperity electroadhesion modeling in this study.

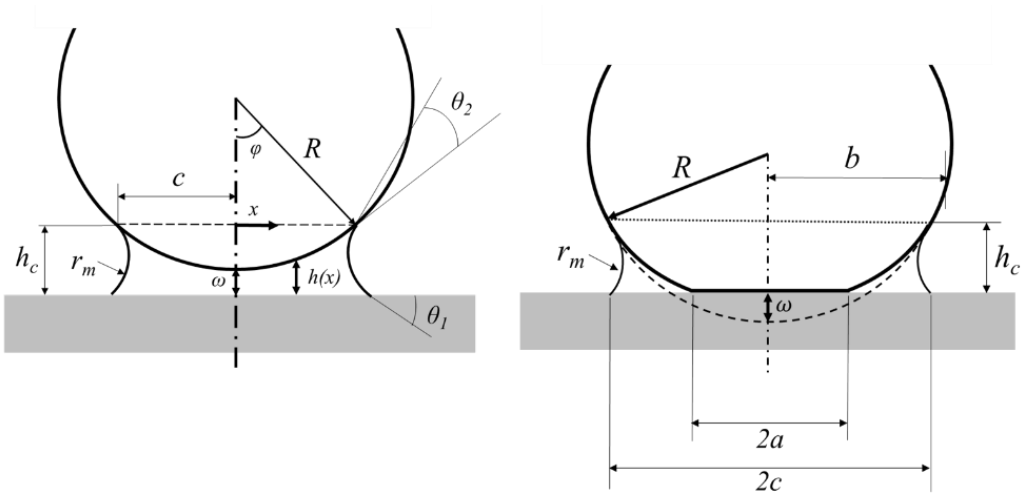

Figure 37. Schematic presentation of equivalent single asperity-flat rigid surface contact under meniscus actions, without showing any deformed shape; (a) non-contacting, (b) Under contact.

To determine thickness of the meniscus liquid formed at each asperity, a spherical asperity of radius *R* and a flat surface under the influence of meniscus action for both contacting and noncontacting conditions has been considered as shown in Figure 37. In the figure, ω is the spherical interference, which is negative in the noncontacting region; r_m is the radius of the meniscus; h_c is the meniscus liquid thickness at the asperity; and θ_1 and θ_2 are contact angles of liquid with the flat surface and asperity respectively. The pressure inside the liquid is lower than outside of the liquid for a concave meniscus. The pressure difference Δp acting at the wetted circular area can be determined by Laplace relationship, given by equation (11),

$$\Delta p = \frac{\gamma_{lv}}{r_m} = \frac{\gamma_{lv}(\cos\theta_1 + \cos\theta_2)}{h_c} \qquad (11)$$

where γ_{lv} is the surface tension of the liquid–air interface. Without considering spherical deformation due to meniscus adhesion or contact force, the meniscus adhesion force was

proposed by Israelachvili [130] for both contacting and noncontacting conditions, given by equation (12),

$$f_{m_{simplified}} = \begin{cases} 2\pi R\gamma_{lv}(\cos\theta_1 + \cos\theta_2)\left(1 + \frac{\omega}{h_c}\right) & ,\omega < 0 \\ 2\pi R\gamma_{lv}(\cos\theta_1 + \cos\theta_2) & ,\omega \geq 0 \end{cases} \quad (12)$$

The gap between the asperity and the flat surface along the lateral direction, *h(x)* for both noncontacting and contacting conditions and without considering spherical deformation can be approximated as [131],

$$h(x) = -\omega + \frac{x^2}{2R} \quad (13)$$

Assuming the meniscus bridge is approximately cylindrical, the volume of the meniscus liquid can be calculated as [131],

$$V = \pi R[h(x)^2 - \omega^2] \quad (14)$$

The meniscus volume and film thickness remain almost constant for capillary actions, which indicates that only the meniscus area changes with interference as long as the asperity is in contact with the liquid film. When the asperity just comes into contact with the flat surface, $\omega = 0$, and *h(x)* can be considered as the liquid film thickness, h_c, which can be calculated as,

$$h_c = h(x) = \sqrt{\frac{V}{\pi R}} \quad (15)$$

The improved meniscus model proposed by Xue and Polycarpou [124] model considers spherical deformation of the asperity within elastic limit during the contact with the flat surface. The model predicts the adhesion force due to meniscus for both contacting and

non-contacting conditions and therefore the model was adopted for calculating meniscus adhesion force in this study.

6.3.1. Noncontacting asperity (ω < 0)

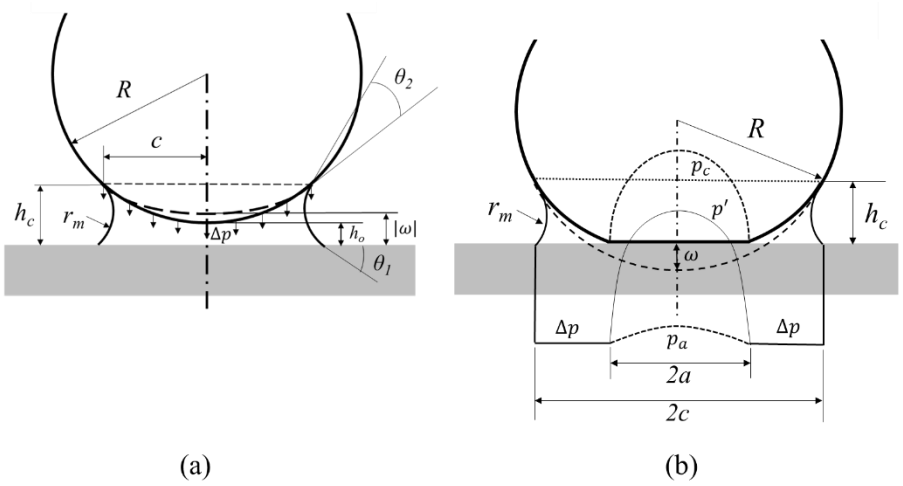

Figure 38. Schematic presentation of equivalent single asperity-flat rigid surface contact under meniscus actions, showing deformed shapes and pressure distributions; (a) non-contact condition, (b) Under contact condition.

Figure 38(a) shows the geometry of a noncontacting spherical asperity with its deformed shape (ω <0) in the presence of capillary adhesion. Assuming the displacement is negative in the departing direction, the vertical displacement, u, due to the Laplace pressure is obtained from equation 16 [122,132],

$$u = \begin{cases} \frac{4c\Delta p}{\pi E_r}, & when\ r = c \\ \frac{2c\Delta p}{E_r}, & when\ r = 0 \end{cases} \quad (16)$$

where r is the radial coordinate. E_r is the reduced elastic modulus given by,

$$\frac{1}{E_r} = \frac{1-{\nu_1}^2}{E_1} + \frac{1-{\nu_2}^2}{E_2} \quad (17)$$

where E_1, E_2, v_1, and v_2 are elastic moduli and Poisson's ratios of the spherical asperity and the flat surface, respectively. The radius of the meniscus area, c, is given by

$$\frac{c^2}{2R} + \frac{2\Delta p c(\pi-2)}{\pi E_r} + h_o - h_c = 0 \quad (18)$$

where h_o is the normal separation at the center. The meniscus area due to Laplace pressure is πc^2, and the attraction force pulling the asperity to the flat surface is given by equation (19),

$$f_m = \pi \Delta p c^2 \quad (19)$$

The thick dashed line in Figure 38(a) represents the original asperity profile and the solid line represents the deformed shape. The spherical asperity deforms towards the surface due to the meniscus force. The approach of the sphere is given by

$$\omega = h_o + \frac{2c\Delta p}{E_r} \quad (20)$$

6.3.2. Contacting asperity ($\omega > 0$)

Figure 38(b) shows a sphere contacting with a rigid surface ($\omega > 0$). During the contact, the liquid is expelled from the contact region. The Dugdale stress Δp acts on the wetted area $a < r < c$ beyond which the stress is zero. The Hertzian compressive pressure $p_c(r)$ and the tensile adhesive pressure $p_a(r)$ inside the contact zone are given by equation (11) [121]:

$$\begin{cases} p_c(r) = \frac{2E_r\sqrt{a^2-r^2}}{\pi R} \\ p_a(r) = \frac{2}{\pi}\Delta p \tan^{-1}\sqrt{\frac{c^2-a^2}{a^2-r^2}} \end{cases}, \quad for\ r>a \quad (21)$$

At $r = a$, the Dugdale stress is equal to Δp, ensuring stress continuity at the crack tip. The work of adhesion (w) is defined as the external work done to separate a unit area of the adhering surfaces. In this model, the work of adhesion is calculated for the meniscus adhesion assuming no solid–solid interaction across the liquid (outside the contact region), given by equation (22)

$$w = h_c \Delta p = r_m(\cos\theta_1 + \cos\theta_2)\frac{\gamma_{lv}}{r_m} = \gamma_{lv}(\cos\theta_1 + \cos\theta_2) \quad (22)$$

The adhesion parameter, λ is given by,

$$\lambda = \Delta p \left(\frac{9R}{2\pi w E_r^2}\right)^{1/3} = \frac{1}{r_m}\left(\frac{9R{\gamma_{lv}}^2}{2\pi(\cos\theta_1+\cos\theta_2)E_r^2}\right)^{1/3} \quad (23)$$

The MD theory gives [121],

$$\frac{\lambda a^{*2}}{2}\left[\sqrt{m^2-1} + (m^2-2)\tan^{-1}\sqrt{m^2-1}\right] + \frac{4\lambda^2 a^*}{3}\left[\sqrt{m^2-1}\tan^{-1}\sqrt{m^2-1} - m + 1\right] = 1 \quad (24)$$

Where, $m=c/a$ and a^* is the normalized contact radius, which is given by,

$$a^* = a\left(\frac{4E_r}{3\pi w R^2}\right)^{1/3} \quad (25)$$

The normalized approach can be determined by,

$$\omega^* = \omega\left(\frac{16{E_r}^2}{9\pi^2 w^2 R}\right)^{1/3} = a^{*2} - \frac{4a^*\lambda}{3}\sqrt{m^2-1} \quad (26)$$

The adhesion force due to Laplace pressure outside the contact area can be obtained as

$$f_m = \Delta p\pi(c^2 - a^2) \; or \; \frac{f_m}{\pi w R} = \frac{\pi}{2}\lambda a^{*2}(m^2-1) \quad (27)$$

The MD model becomes a "DMT like" contact for small λ values (e.g., high humidity levels and small stiff spheres) [133]. The model becomes a "JKR-type" contact at low humidity levels and large compliant spheres, and λ becomes larger [134].

For large λ values, the adhesive force inside the contact region ($r < a$) also needs to be considered. The adhesion force inside the contact region can be calculated by integrating the adhesive stress, which is given by,

$$f_{s-s} = \int_0^a 2\pi r p_a(r) dr = 4\Delta p \int_0^a r \tan^{-1} \sqrt{\frac{c^2-a^2}{a^2-r^2}}\, dr \quad (28)$$

And the total meniscus adhesion force is obtained as

$$f_a = f_m + f_{s-s} = 2\Delta p a^2 \left(m^2 \tan^{-1} \sqrt{m^2-1} + \sqrt{m^2-1}\right) \quad (29)$$

Contact force can be calculated by integrating the compressive stress, given by,

$$p = \int_0^a 2\pi r p_c(r) dr = \frac{4E_r a^3}{3R} \quad (30)$$

The external force can be calculated by,

$$f_{ex} = p - f_a \quad (31)$$

6.3.3. Inclusion of electrostatic force in the improved meniscus model

When an external voltage is applied to the haptics surface, the electrostatic force between the asperity and the flat surface is affected by the meniscus action. The contact angle between the dielectric and water significantly changes with the applied voltage and therefore meniscus adhesion also changes. The change in meniscus force affects the electrostatic force. The total adhesion force can be calculated as the sum of the electrostatic and meniscus forces after applying the voltage.

Referring to Figure 37(b), the region outside of the contact between the spherical asperity and the flat surface can be considered as parallel plate capacitors, where the gap between the asperity and the flat surface is filled with a third material, either air or gas. The thickness of dielectric material (Figure 36) needs to account for electrostatic effect, which can be achieved by taking the thickness of the flat surface equal to dielectric thickness, *d* of 1 µm. When the gap is filled with a single material only, following the work from [115], the normal component of the electrostatic stress at a point after applying voltage is presented as,

$$\sigma(h(x)) = \frac{U^2 \varepsilon_o {\varepsilon_d}^2 \varepsilon_g}{2\left(\varepsilon_g d + \varepsilon_d h(x)\right)^2} \quad (32)$$

Where, *U* is the applied voltage, ε_o is the vacuum permittivity and ε_d and ε_g are dielectric constants of the dielectric material and the gap material respectively, *h* is the thickness of the gap at a lateral distance from *x* from the center of the sphere, which can be determined from equation (3). The gap material can be either water or air. Dielectric constant of air and water are 1 and 80 respectively. The electrostatic force can be calculated by integrating $\sigma(h(x))$ over the projected area filled with the gap material. The net electrostatic force for the gap filled with both air and meniscus water can be determined by,

$$f_{el} = 2\pi \left[\int_a^c [\sigma(h(x))]_{water}\, x\, dx + \int_c^b [\sigma(h(x))]_{air}\, x\, dx\right] \quad (33)$$

The distance *b* is the maximum lateral distance from the center of the sphere. It is the maximum distance where the effect of electrostatic force is significant.

After applying the voltage, the contact angle between the water and the flat surface significantly changes. Young-Lippman electrowetting on-dielectric (EWOD) model was

widely used to determine the contact angle after applying the voltage. The Y-L model was extended by Klarman et al. [135] to account for high frequency AC voltage, which is given by,

$$cos\theta_1'(U,\omega') = cos\theta_1 + \eta = cos\theta_1 + \frac{1}{\sqrt{1+\omega'^2\tau_b^2}}\frac{\varepsilon_0\varepsilon_d U^2}{2\gamma_{lv}d} \quad (34)$$

When very high voltage is applied, contact angle saturation can also happen. The energy balance model by Lin et al. [136] is widely used for determining the contact angle under saturation state after applying the voltage, which is given by,

$$cos\theta_1'(sat) = \frac{1}{2} - \frac{1+E_0\, cos\,\theta_1/3-2E_0/3}{2(\eta-cos\theta_1+E_0/3)} \quad (35)$$

Where θ_1 and θ_1' are the contact angles at 0 V and the applied voltage respectively, η is the EWOD number, ω' is the AC frequency, τ_b and E_0 are fitting parameters, which represent the double-layer build-up time and constant dependent on the initial droplet geometry. The values of τ_b and E_0 were taken as 0.32 ms and 0.5 respectively, for the 5 kHz AC frequency, found from the literature [116].

After calculating θ_1', the meniscus force can be recalculated using equations (16-29). Then the total adhesion force can be calculated as

$$f_{total} = \begin{cases} f_{el} + f_m' \,, noncontacting \\ f_{el} + f_a' \quad , contacting \end{cases} \quad (36)$$

Where, f_m' and f_a' are meniscus forces for corresponding θ_1' at noncontacting and contacting conditions respectively.

The contact force now includes the electrostatic force, leading to a higher interference. The contact force can be calculated using the same equation (30).

Finally, the external force can be calculated as-

$$f_{ex} = p - f_{total} \tag{37}$$

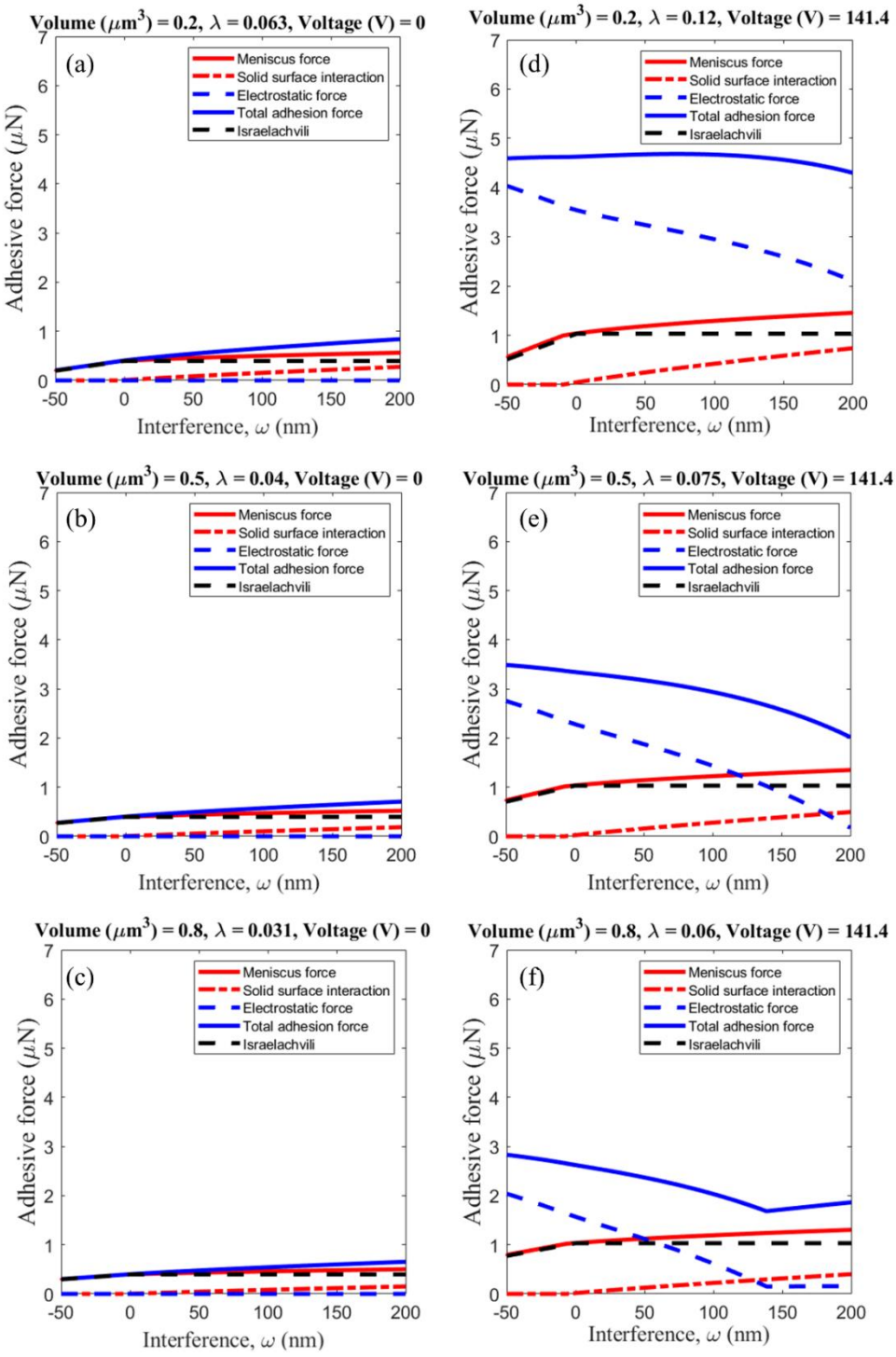

Figure 39. Summary results of adhesion forces before and after applying the voltage of 141.4 V at different water volumes.

6.4. Simulation results for single asperity electroadhesion model

Figure 39 shows dependence of adhesion forces on liquid meniscus volumes before and after applying voltage for an asperity radius of 6.4 μm. This radius is equivalent to the larger trapezoidal asperity geometry shown by Xinyi et al. [116] in their single asperity electroadhesion model. The base radius of the asperity was considered as b = 2 μm (Appendix F), which was also used in this study to account for electrostatic force from equation (23) when a voltage is applied. Although [116] showed the contact results for a single contact interference, Figure 39 represents the results for a range of interference from -50 nm to 200 nm, which were under elastic limit. Negative interference indicates asperity separation from the surface. The contact angle θ_1 between the flat surface and liquid water is 108^o, and the contact angle θ_2 between the asperity and liquid water is 80^o. After applying a voltage of 141.4 V, the contact angle θ_1 changes to 79.7^o according to equations (24,25) while θ_2 remains the same. All contact angles and voltage measurements were found somewhere else from the literature [116] and used in this study. Figures 40(a-c) and 40(d-f) show the results for adhesion forces before and after applying the voltage. Results for three water volume was shown in the figure-0.2 μm^3, 0.5 μm^3 and 0.8 μm^3. It was found that the total adhesion forces before applying voltage were lower than 1 μN for the three water volumes at the interference of 200 nm. This was attributed to hydrophobic meniscus formation with the haptic dielectric layer. Schematic diagram of the contact and meniscus conditions before and after applying voltage are shown in Figure 40. Since the meniscus did not significantly wet the surface, total adhesion forces were much lower. This adhesion force further decreased with decreasing the interference up to -50 nm. Note

that adhesion due to solid-solid interactions are present during contact and increased with increasing interference. The changes in λ also suggest that at lower water volume, the contact was "JKR like" as indicated by higher value of λ and hence higher solid-solid interactions than those for higher water volume. With increase in water volume, the contact becomes more "DMT like" and meniscus force dominates over solid-solid interactions.

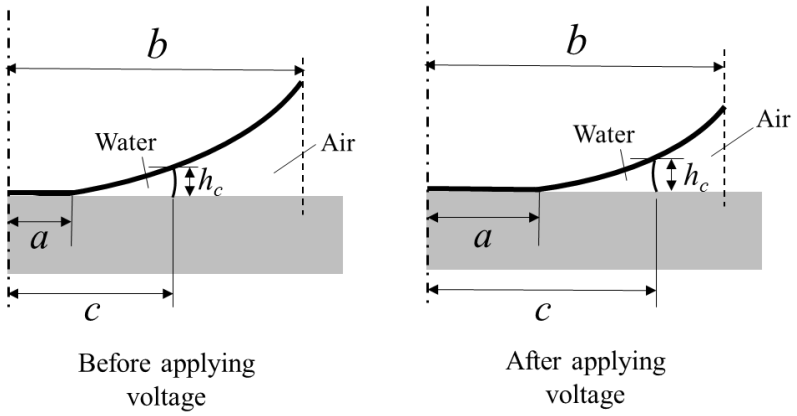

Figure 40. Schematic diagram of contact and meniscus conditions of the asperity before and after applying voltage

The total adhesion force significantly increased after applying voltage due to inclusion of the electrostatic force. For a given water volume and positive interference, the meniscus adhesion force after applying the voltage increased than before applying the voltage due to decrease in contact angle, making the meniscus action hydrophilic. This resulted in increase in meniscus force as the meniscus area increased after applying the voltage. It was also evident from Figure 40. The total electrostatic force consists of the contributions from both air and water. Air medium, having lower dielectric constants than water, contributes more to the electrostatic force than water medium. Although the meniscus

force and solid-solid interaction increased with the interference for a given water volume, the electrostatic force decreased with increasing the interference as more area of the asperity was covered with water, suppressing the electrostatic effect. The electrostatic force further decreased with increasing the water volume for a given interference due to increase in asperity contact with water. For each water volume, the electrostatic force reaches a minimum value when the individual contribution of air becomes negligible. With increasing the water volume, the minimal electrostatic force was reached at lower interference. From Figures 39(d-f), the maximum total adhesion force was 4.6 μN for the water volume of 0.2 μm^3, then the adhesion gradually decreased with increasing the water volume. The minimum adhesion force was found as 1.6 μN for the water volume of 0.8 μm^3 at the interference of 130 nm. Applying the voltage also increase the value of λ for the same water volume, indicating the external voltage makes the meniscus contact more "JKR like", especially at very low water volume.

The meniscus forces calculated from the improved EMD model were higher than those calculated from Israelachvili's model, due to considering spherical deformation of the asperity at different interferences. The solid-solid interactions were also found zero for noncontact conditions.

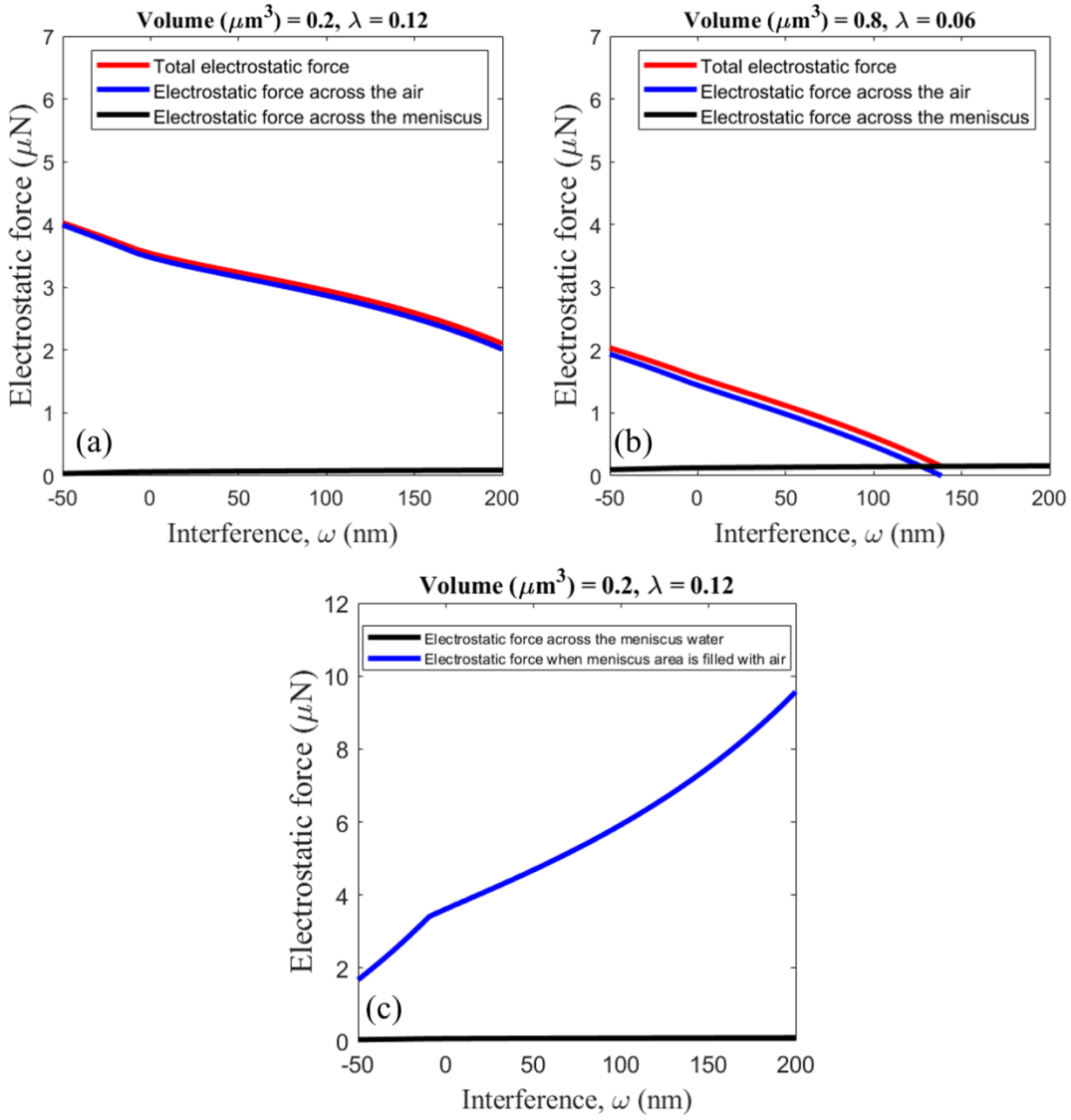

Figure 41. Contributions of meniscus water and air gap to the total electrostatic force.

Figure 41 shows electrostatic forces across the meniscus water and the air gap between the fingertip and haptic surfaces and their contributions to the total electrostatic force. Figures 41(a) and 41(b) show the results for the water volume of 0.2 μm^3 and 0.8 μm^3 respectively. Under both meniscus conditions, the contribution of air is predominant to the total electrostatic force due to lower dielectric constant of air. Since water has much higher

dielectric constant than air, the electrostatic effect is much less compared to air. For higher water volume, the total electrostatic force decreased due to lesser contribution of air to the electrostatic effect at higher water volume and interference and eventually becomes minimal as shown in Figure 41(b). Figure 41(c) shows the comparison between the electrostatic force across the meniscus water volume of 0.2 μm^3 and theoretical electrostatic force across the same area when the water is replaced with air. From the figure, it is evident that meniscus water is significantly suppressing the electrostatic effect, reducing to electrostatic force to nearly zero in the meniscus area. The suppression is more prominent for higher interferences.

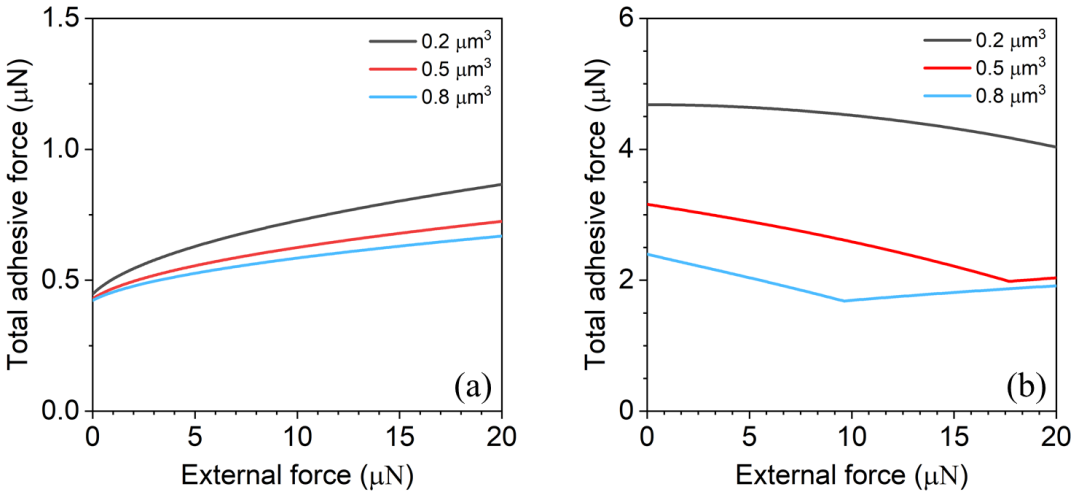

Figure 42. Variation of calculated total adhesion force with external force at different meniscus water volumes, (a) before applying voltage, (b) after applying voltage.

Figure 42 shows variation of total adhesive force with the external force at different water volumes. The results shown in Figure 42 corresponds to the interferences shown in Figure 40. It is evident from the figure that the total adhesion force increased with increasing the external force. Increasing the external force increased the contact area, which in turn

increased the meniscus area and meniscus force, leading to increase in total adhesion force. Higher meniscus water volume led to higher meniscus force for any external force.

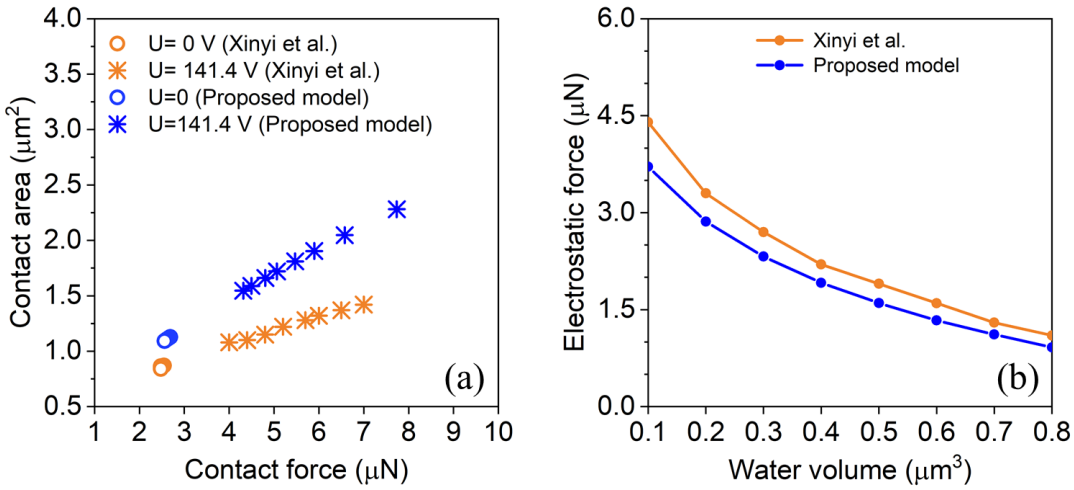

Figure 43. Comparison of the proposed model with literature. Figure (a) shows comparison of contact forces and areas, and Figure (b) shows comparison of electrostatic force.

After applying voltage, at the water volume of 0.2 μm^3, total adhesion force decreased with increasing the external force. It was attributed to reduction in electrostatic forces with the external force, as the asperity came more into contact with the meniscus water, suppressing the electrostatic effect. For 0.5 μm^3 and 0.8 μm^3, the total adhesion force reached a minimum value with increasing the external force and then it again started increasing with external force. The minimum adhesion was attributed to minimum value of electrostatic force as the asperity was completely covered with the meniscus water. With increase in external force, the meniscus force dominated the total adhesion, which increased with increasing the external force.

Xinyi et al. [116] proposed a electroadhesion model by considering the asperity as a truncated cone. A finite element model was developed, and meniscus and electrostatic

effect was considered in their model to predict electroadhesion forces. Multiple asperity dimensions were used in their study, however, only one asperity dimension was taken for comparison purposes in this study. As mentioned earlier, the asperity radius of 6.4 μm was used in this study which is equivalent to dimensions of one of the trapezoidal asperities in their model. The trapezoidal dimension and the equivalent spherical dimension are shown in the Appendix F. Figure 43 shows comparison of the proposed model with the single asperity model by Xinyi et al. [116]. Figure 43(a) shows the comparison of contact areas and contact forces for different meniscus water volumes and Figure 43(b) shows comparison of electrostatic force with water volume using both models. The data points for the proposed model were extracted for the external force of 2 μN and electrostatic forces were calculated for the applied voltage of 141.4 V using a base circular area with a radius of 2 μm. From Figure 43(a), it is evident that the proposed model showed higher contact areas and contact forces then Xinyi et al. at different water volumes before and after applying the voltage. In the proposed model, the direction of meniscus adhesion force before applying voltages was considered towards the flat surface. Although the contact was slightly hydrophobic, that does not exclude the adhesion between the surfaces, otherwise meniscus water would get separated from the surfaces. Due to hydrophobicity, the meniscus force was considered in departing direction from the surface in Xinyi et al. model, contributing to lesser contact forces than the proposed model before applying voltages. Moreover, solid-solid interactions were considered for meniscus force calculation in the proposed model, which was not present in Xinyi et al. These resulted in higher meniscus force and higher meniscus area before and after applying the voltage. As

more areas were covered by water due to higher meniscus forces according to proposed model, they suppressed the electrostatic forces after applying voltages, resulting in lower electrostatic forces than those reported by Xinyi et al. for different water volumes, shown in Figure 43(b).

6.5. Rough surface electroadhesion model

The EMD based single asperity electroadhesion model (EMD-EA) can be incorporated into the GW (statistical) based rough surface model to predict adhesion forces for a finite contact surface. The GW model assumes that two rough surfaces can be represented by an equivalent rough surface which is in contact with a smooth rigid surface [117]. Figure 44 shows an equivalent rough surface in contact with a smooth surface under meniscus actions. The meniscus actions can be altered by the application of electrostatic force. The net adhesion forces can be predicted by considering individual asperity contributions in terms of meniscus and electrostatic forces.

According to GW model, surface properties of an equivalent rough surface can be characterized by three parameters: average radius of curvature of the asperities (R), surface roughness (σ) and areal density of the asperities (η), where the asperity heights follow a certain statistical distribution, usually assumed a Gaussian distribution, given by,

$$\Phi(z) = \frac{1}{\sigma\sqrt{2\pi}} e^{-0.5(z/\sigma)^2} \quad (38)$$

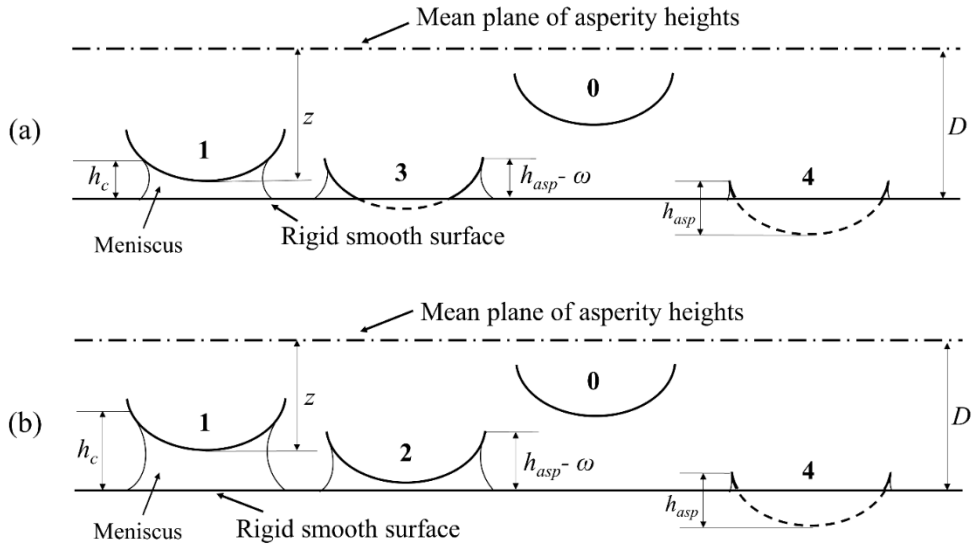

Figure 44. Schematic representation of GW based rough surface electroadhesion contact model, (a) when $h_{asp} > h_c$, (b) when $h_{asp} \leq h_c$.

Where, z is the asperity height from the mean reference plane. Another roughness parameter h_{asp}, defined as limiting asperity height, was also introduced by Xue et al. [124] to account for meniscus forces for individual asperities. The nominal area of a single asperity can be written as,

$$\frac{1}{\eta} = 2\pi R h_{asp} \quad (39)$$

And limiting asperity height (h_{asp}) can be written as

$$h_{asp} = \frac{1}{2\pi R\eta} \tag{40}$$

Depending on h_{asp}, meniscus film thickness (h_c), and spherical interference (ω), all asperities under meniscus actions can be grouped into five different types:

Type 0: Asperity not in contact with either liquid or the flat surface

Type 1: h_{asp} is partially covered by the liquid but noncontacting with the flat surface.

Type 2: h_{asp} is completely covered by the liquid but noncontacting with the flat surface.

Type 3: h_{asp} is partially covered by the liquid and contacting with the flat surface.

Type 4: h_{asp} is completely covered by the liquid and contacting with the flat surface.

At a particular mean surface separation, D between the average plane of asperity heights and the flat rigid surface, two contact cases can be found depending on h_{asp} and $h_{c.}$

Case 1: when $h_{asp} > h_{c,}$ $\begin{cases} Type\ 1: D - h_c \le z \le D \\ Type\ 2: Impossible \\ Type\ 3: D \le z \le h_{asp} - h_c + D \\ Type\ 4: h_{asp} - h_c + D \le z \le D + h_c \end{cases}$

And the meniscus force F_m for Case 1 can be calculated as,

$$F_m = A_n\eta \left[\int_{D-h_c}^{D} f_{m1}\Phi(z)dz + \int_{D}^{h_{asp}-h_c+D} f_{m3}\Phi(z)dz + \int_{h_{asp}-h_c+D}^{D+h_c} f_{m4}\Phi(z)dz\right] \tag{41}$$

Case 2: when $h_{asp} \le h_{c,}$ $\begin{cases} Type\ 1: D - h_c \le z \le h_{asp} - h_c + D \\ Type\ 2: h_{asp} - h_c + D \le z \le D \\ Type\ 3: Impossible \\ Type\ 4: D \le z \le D + h_c \end{cases}$

And the meniscus force F_m for Case 2 can be calculated as,

$$F_m = \eta A_n \left[\int_{D-h_c}^{h_{asp}-h_c+D} f_{m1}\Phi(z)dz + \int_{h_{asp}-h_c+D}^{D} f_{m2}\Phi(z)dz + \int_{D}^{D+h_c} f_{m4}\Phi(z)dz\right] \tag{42}$$

Here, f_{mi} $(i = 0 - 4)$ are meniscus forces for single asperities at different conditions. A_n is the nominal area of contact of the interface. For Type 0 condition, the meniscus contribution is zero. For Type 1 and 3 conditions, meniscus forces can be calculated using equations (19) and (29) respectively, as discussed in Section 6.3. For Type 2 and 4 contact conditions, the effective meniscus film thickness, h_c can be determined by

$$h_c = h_{asp} - \omega \tag{43}$$

For Type 2, the wetted area is the nominal area of the asperity, given by,

$$A_m = \frac{1}{\eta} \tag{44}$$

And the meniscus force for Type 2 contact is given by,

$$f_{m2} = \Delta p A_m = \frac{\gamma_{lv}(\cos\theta_1 + \cos\theta_2)}{(h_{asp} - \omega)\eta} \tag{45}$$

For Type 4, the wetted area is affected by the deformed shape of the spherical asperity, and can be written as,

$$A_m = \frac{1}{\eta} - \pi a^2 \tag{46}$$

And the corresponding meniscus force is given by,

$$f_{m4} = \Delta p A_m = \frac{\gamma_{lv}(\cos\theta_1 + \cos\theta_2)}{(h_{asp} - \omega)} \left(\frac{1}{\eta} - \pi a^2\right) \tag{47}$$

The adhesive force due to solid-solid interactions can be calculated as,

$$F_{s-s} = A_n \eta \int_D^\infty f_{s-s} \Phi(z) dz \tag{48}$$

After applying voltage on the haptics surface, meniscus parameters will be affected and F_m and $F_{s\text{-}s}$ can be recalculated using equations (10-29) and (38-48).

All five contact types need to be considered for calculating electrostatic forces between the interfaces. For Type 0 contact, the gap between the asperity and the flat surface will be filled with only air and for Types 2 and 4, the gaps will be filled with only liquid water. Since electrostatic force equation (23) is an integral equation, it can be directly used for all five contact conditions. The two contact cases for meniscus force calculations are also applicable for electrostatic force calculations, except Type 0 contact will also be included to both cases. To calculate electrostatic forces for all conditions, the limiting asperity radius (r_{asp}) is used as maximum radius, b in the equation (23). r_{asp} is the radius of the projected area of the asperity at the height of h_{asp}.

For Case 1, the total electrostatic force can be calculated as,

$$F_{el} = A_n\eta \left[\int_0^{D-h_c} f_{el0}\Phi(z)dz + \int_{D-h_c}^{D} f_{el1}\Phi(z)dz + \int_{D}^{h_{asp}-h_c+D} f_{el3}\Phi(z)dz + \int_{h_{asp}-h_c+D}^{D+h_c} f_{el4}\Phi(z)dz\right] \quad (49)$$

Similarly, the total electrostatic force for Case 2 can be calculated as,

$$F_{el} = A_n\eta \left[\int_0^{D-h_c} f_{el0}\Phi(z)dz + \int_{D-h_c}^{h_{asp}-h_c+D} f_{el1}\Phi(z)dz + \int_{h_{asp}-h_c+D}^{D} f_{el2}\Phi(z)dz + \int_{D}^{D+h_c} f_{el4}\Phi(z)dz\right] \quad (50)$$

Here, f_{eli} $(i = 0 - 4)$ are electrostatic forces for single asperities at different conditions.

The total adhesive force between the interfaces can be calculated as,

$$F_{adh} = F_m + F_{s-s} + F_{el} \quad (51)$$

The contact force between the interfaces can be determined by,

$$P = A_n\eta \int_D^{\infty} p\Phi(z)dz \quad (52)$$

And the external force can be calculated as,

$$F_{ex} = P - F_{adh} \quad (53)$$

For a single asperity study, the fingertip surface can easily be considered as a flat interface, since the asperity radius is much smaller than the radius of curvature of skin. For rough surface modeling of small nominal area, the fingertip surface can still be considered as a flat interface. In this study, the contact between the fingertip and the haptics sample with a small nominal area of 100 µm ×100 µm was considered for rough surface electroadhesion modeling. Since the nominal area is smaller compared to wavelength of wavy shaped ridges of the fingertip surface, moreover the fingertip surface is very complaint, the present study considers the fingertip as a flat smooth surface to avoid computational complexities. An equivalent deformable rough surface was considered to be in contact with a rigid flat surface, according to GW model. In this study, the surface profile of a haptic surface shown in [116] was considered and the surface parameters of the equivalent rough surface are shown in Table 13. It was also assumed that individual asperities were under meniscus actions with the same water volume and simulation results were showed in terms of meniscus water volume of individual asperities.

Table 13. Surface parameters of the equivalent rough surface.

σ (nm)	R (µm)	η (µm^{-2})	h_{asp} (nm)	r_{asp} (µm)	γ_{lv} (mN/m)	A_n (µm^{-2})	E_r (MPa)	θ_1 (º)	θ_2 (º)
96	1.4	0.49	232	0.8	72.8	10000	60	108	80

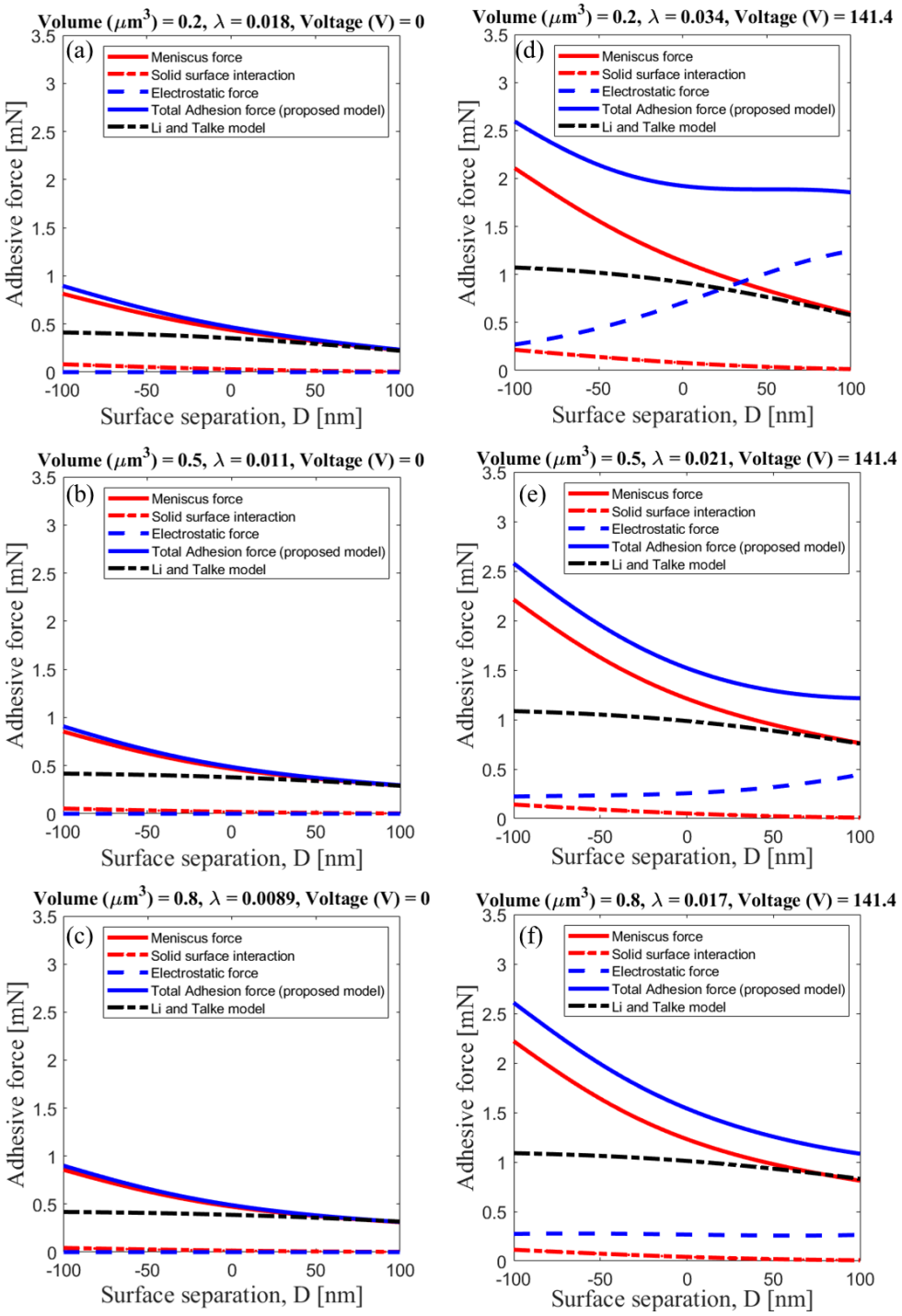

Figure 45. Summary results of adhesive forces under rough surface contact before and after applying the voltage of 141.4 V at different water volumes.

6.6. Rough surface simulation results

6.6.1. Adhesive forces

Figure 46 shows summary results of adhesive forces for different meniscus water volumes in terms of surface separations, D. Figures 46(a-c) and 46(d-f) represent the results for the adhesive forces before and after applying voltages respectively. Negative surface separation means the surface is in contact with an interference. It is evident from Figures 46(a-c) that for a particular water volume, the adhesive forces have much lower values at higher surface separations and the force increased with decreasing the separation. When the surface came into contact with the flat surface, the adhesive forces further increased. More asperities of the equivalent rough surface came into contact with the flat surface, increasing the contact and meniscus areas, leading to higher meniscus forces. Meniscus forces calculated at negative separations were much higher compared to the results found from Li and Talke [137] model. In that model, asperity deformations were neglected under contact conditions. For a particular separation, meniscus forces slightly increased with increasing the water volume. Again solid-solid interactions were slightly decreasing with increasing the water volume. Interestingly, meniscus water volume per asperity did not significantly affect the adhesion forces before applying voltage under the same surface separation.

The adhesive forces significantly increased after application of the voltage. In Figures 46(d-f), results were shown after applying the voltage of 141.4 V. For any surface separation under the same water volume, electrostatic force after applying voltage contributed to total adhesion by changing the contact angle, thereby affecting the meniscus

force. As the meniscus contact became hydrophilic after applying the voltage, meniscus forces increased due to increase in meniscus areas. In addition to that, the electrostatic force itself contributed to total adhesion. The meniscus forces increased by more than 100% after applying voltages at different surface separations. Meniscus forces further increased rapidly under contact conditions. At the same time, electrostatic forces decreased by decreasing the surface separation. Under contact conditions, electrostatic forces were suppressed by meniscus water volumes surrounding individual asperities. As the surface separation was decreased, meniscus forces predominantly contributed to total adhesion forces. Meniscus forces calculated using the proposed model were much higher than those predicted by Li and Talke model under the same contact conditions. Lesser differences in meniscus forces were found between the two models when surface separations were higher. Solid-solid interactions also increased at negative separations after applying voltages. Meniscus water volumes did not significantly affect the meniscus forces under contact conditions. On the other hand, electrostatic forces were higher at higher surface separations, which gradually decreased with decreasing the separation from 100 nm to -100 nm for the water volumes of 0.2 μm^3 and 0.5 μm^3. Electrostatic force at 0.5 μm^3 were lower than 0.2 μm^3 for any surface separations as electrostatic force was suppressed more with higher water volume. At 0.8 μm^3, asperities were immersed with meniscus water volumes even at higher separations, suppressing electrostatic forces even more. Therefore, electrostatic forces were almost constant under the surface separations shown in Figure 43(f). the maximum adhesive force at a surface separation of 100 nm was the highest at the water volume of 0.2 μm^3 and lowest at the water volume of 0.8 μm^3.

Maximum adhesive forces at the separation of -100 nm were almost the same for all water volumes.

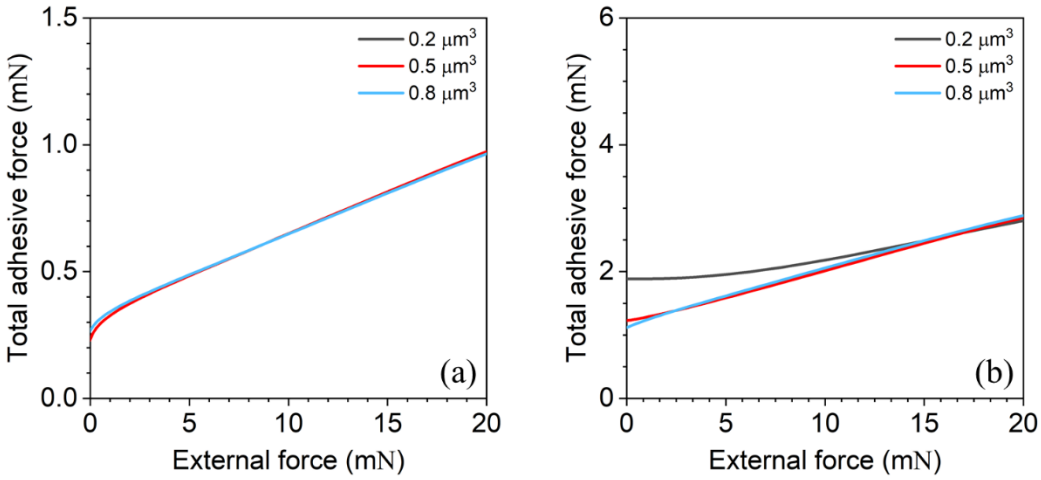

Figure 46. Variation of calculated total adhesion force with external force for rough surface contacts at different meniscus water volumes, (a) before applying voltage, (b) after applying voltage.

Figure 47 shows variation of total adhesive force with the external force for rough surface contacts at different water volumes. The results shown in Figure 47 corresponds to the interferences shown in the Figure 46. It was found that the total adhesion force did not significantly changed with changing the meniscus water volume. However, the total adhesion increased with increasing the external force under meniscus actions. This increase was attributed to increase in meniscus forces. After applying voltage, the total electroadhesion force was much higher compared to that before applying voltage. The electrostatic force was dominant at the water volume of 0.2 μm^3 even under contact and therefore, the total adhesion force was higher at lower external force compared to other meniscus volumes. For 0.5 μm^3 and 0.8 μm^3, the total adhesion force was almost the same at any external force. This was attributed to least electrostatic effect as a result of asperities

fully covered with the water. Higher water volume suppressed the electrostatic behavior, allowing the meniscus force to dominate the total adhesion for both water volumes.

6.6.2. Pull-off forces

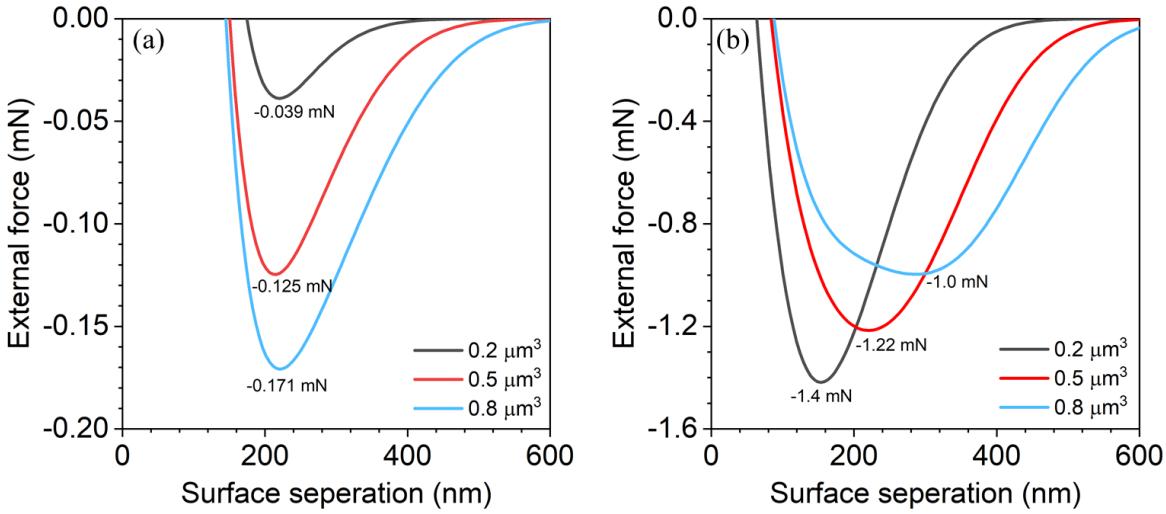

Figure 47. External and pull off forces vs surface separations at different meniscus water volumes (a) before applying voltage, (b) after applying voltage.

Figure 48 shows variation of external forces with surface separations under different meniscus water volumes. Figures 48(a) and 48(b) show the results before and after applying the voltage of 141.4 V, respectively. Pull-off force for each condition can be calculated by the minimum value of external force. From 48(a), it was found that with increase in water volume, the pull-off force increased before applying the voltage. In these cases, meniscus forces dominated the adhesion at positive surface separations, which increased with increasing the water volumes, leading to higher pull-off forces at higher meniscus water volumes. The results were in good agreement with other studies in the literature [138]. Maximum and minimum pull of forces before applying the voltage were

found as 0.171 mN and 0.039 mN respectively. However, the opposite trend of pull-off forces was noticeable after applying the voltage. Pull-off force increased with decreasing water volume after applying the voltage. In these cases, electrostatic forces dominated the adhesion under positive surface separations. As electrostatic forces decrease with increasing the water volume, higher adhesion forces were found for positive separations at lower water volumes. Pull-off forces after applying voltages were much higher compared to that before applying voltage. Maximum and minimum pull-off forces were found as 1.4 mN and 1.0 mN respectively, corresponding to water volumes of 0.8 μm^3 and 0.2 μm^3 respectively. Interestingly, pull-off force at 0.8 μm^3 were found with a wider range of surface separations. This may be attributed to mutual contribution of meniscus force and electrostatic force to total adhesion within the range, since meniscus forces were also higher at 0.8 μm^3 under positive separations.

6.7. Effects of different roughness parameters on interfacial forces

To investigate the effects of different rough surface parameters on the interfacial forces, three arbitrary equivalent rough surfaces have been considered in this study. The variables under considerations are surface roughness (σ), average asperity radius (R) and areal density of asperities (η). the variables are chosen in such as way that the product of all three parameters remain the same for all surfaces. Table 14 show different surface parameters of the arbitrary surfaces. Surface 1 has the lowest roughness and largest asperity radius; and Surface 3 has the highest roughness and smallest asperity radius. Note that the values of surface parameters are closer to the parameters shown in Table 13.

Table 14. Roughness parameters of three arbitrary equivalent rough surfaces

Rough Surface	σ (nm)	R (μm)	η (μm^{-2})
1	75	2.5	0.4
2	100	1.5	0.5
3	125	1	0.6

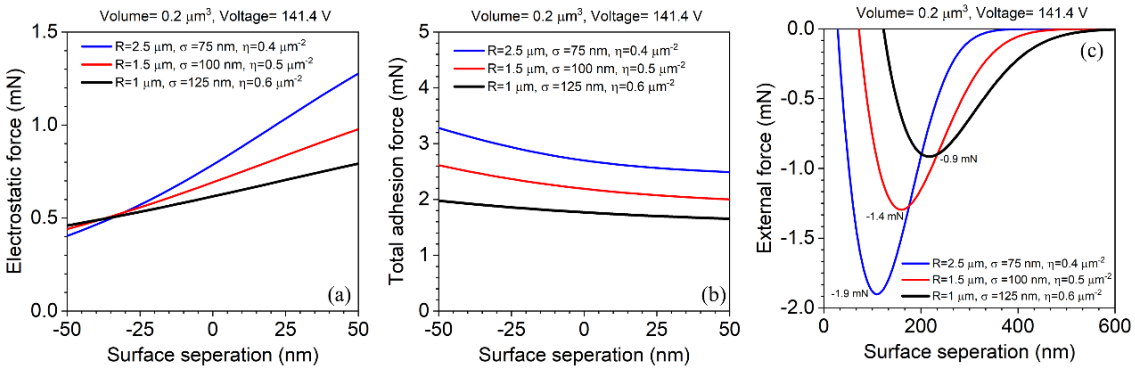

Figure 48. Variation of interfacial forces with different rough surface parameters.

Rough surface contact simulations were performed for the arbitrary surfaces under the meniscus volume of 0.2 μm^3 and the applied voltage of 141.4 V. Summary of different interfacial forces are shown in Figure 49. Figure 49(a), 49(b) and 49(c) shows the results for electrostatic force, total adhesion force and external force respectively. From the figure, it was evident that the Surface 1 showed higher electrostatic force compared to other surfaces under positive surface separations. Because of largest asperity radius, the interfacial gaps under non-contact conditions were lower compared to other surfaces, leading to higher electrostatic force. However, under contact conditions, the electrostatic effect was suppressed by water meniscus. Higher asperity radius and smoother surface led to higher meniscus radii and forces, which also reduced the electrostatic force. The rate of

decrease in electrostatic force was higher compare to other surfaces. At the same time, the meniscus forces were much higher for Surface 1 for the same reason. It led to highest total adhesion forces among all surfaces, for both contacting and non-contacting conditions. Because of higher adhesion, the pull-off force for surface 1 was higher than other two surfaces. the maximum pull-off force was 1.9 mN for Surface 1 and the minimum pull-off force was 0.9 mN for Surface 3 with highest roughness and lowest asperity radius.

6.8. Summary

In this study, a single asperity electroadhesion model was first proposed and it was implemented to a rough surface contact model to predict electroadhesion between human fingertip and haptics surfaces at different meniscus water volumes. The results can be summarized as follows:

(a) Under single asperity contacts, meniscus forces were predominant and did not significantly change with changing the water volume under the same interference due to hydrophobicity. However, electrostatic forces started contributing to the total adhesion forces at lower water volumes and interferences, but the effects gradually decreased with increasing the water volumes and interferences.

(b) Rough surface contact modeling showed that adhesion forces before applying voltages were not significantly affected by the meniscus water volumes due to hydrophobicity at any surface separations. However, total adhesion forces were significantly higher after applying the voltages. At higher surface separations, electrostatic forces were predominant and total adhesion forces decreased with

increasing the meniscus water volume for each asperity. At lower separations or higher contact interferences, meniscus forces were predominant, which were not significantly affected by the water volumes, leading to constant total adhesion forces at different water volumes under contact conditions.

(c) Before applying voltages, the pull-off forces increased with increasing the water volumes, primarily due to contribution of meniscus forces. After applying voltages, the pull-off forces significantly increased due to addition of electrostatic effects, and the pull-off forces decreased with increasing the meniscus water volumes. At the asperity water volume of 0.8 μm^3, the pull-off force was found with a wider range of surface separations, which was attributed to mutual balancing of meniscus and electrostatic effects.

(d) A rough surface with higher asperity radius and lower roughness showed higher electrostatic force under non-contact conditions, and higher total adhesion force and pull-off forces compared to surfaces with lower asperity radii and higher roughnesses.

CHAPTER VII

CONCLUSIONS

7.1. Summary of the research

In this research study, experimental, finite element analysis and analytical modeling have been performed to investigate nanomechanical, nanotribological and surface interactions of ultra-thin films. Three types of contact conditions were considered in this research-solid-solid contacts for hard coatings, solid-solid contacts for softer coatings and solid-liquid contacts. New finding and contributions of the research can be summarized as follows:

1. In Chapter II, elevated temperature nanomechanical and nanotribological properties of ultra-thin nitrogen-doped carbon overcoat (NCOC) or nitrogen-doped diamond like carbon (NDLC) protective film for heat assisted magnetic storage (HAMR) applications were investigated. NCOC with three different thicknesses (2.5, 3.5, and 4.5 nm) were examined in terms of both chemical and mechanical properties at temperatures up to 300 ^{o}C. The chemical changes were traced by XPS, revealing that the configuration of both carbon and nitrogen elements change partially from sp^3- to sp^2-hybridizations with exposure of NCOC samples to annealing. The friction coefficient, wear rate, and deformation of the NCOC films were measured using nanoindentation, nanoscratch and nanowear experiments. Three sets of mechanical experiments verified the operating temperature and thickness dependence of the mechanical and tribological behavior of the NCOC films. Thicker NCOC led to better mechanical and wear behavior at

25 ^{o}C before and after heat treatment and at 300 ^{o}C. Coefficient of friction (COF) of NCOCs significantly increased at 300 ^{o}C due to increase in adhesion. The COFs did not show thickness dependent behavior. Average wear depths of NCOCs were acceptably small after exposure to annealing, thus offering durable films for high temperature applications. Noteworthy, the permanent reduction in mechanical properties associated with annealing reduces in the presence of N dopants.

2. Nanoindentation and nanoscratch studies in Chapter II revealed that Due to instrument limitations and very shallow films, it is very challenging to accurately measure sub-5 nm NCOC/ NDLC films and other HAMR components from experiments without substrate effects. To ensure the robustness of the media especially at higher temperature applications, mechanical properties of ultra-thin sub 5-nm NDLC coatings are of great interest. In Chapter III, very shallow nanoindentations were performed and results were fitted with finite element analysis using a modified indenter geometry to predict the elastic modulus and yield strength of NDLC films of two different thicknesses (3.5 and 4.5 nm) and other components without any substrate effect. Results showed that higher NDLC film thickness led to better elastic modulus and yield strength at 25 ^{o}C before and after heating and at 300 ^{o}C. Hardness to yield strength ratio (H/Y) for NDLC films was also determined and found within the range of 2.2-2.8, which is higher than H/Y ratio of DLC films from earlier studies. This implied the dependence of H/Y ratio on thickness, temperature conditions and chemical structure of NDLC films. Results also showed that the yield strength of FeCo metal layer and glass substrate

in HAMR media decreased at 300 ^{o}C, but almost fully recovered to their initial properties after removal of heat.

3. In Chapter IV, a high temperature mechanical and tribological study was performed to investigate the dependence of friction, wear and mechanical properties of ultra-thin nitrogen doped diamond like carbon (NDLC) films on their sp^2/sp^3 carbon configurations. Two NDLC films with the same thickness of 3 nm, almost the same nitrogen content, and different sp^2/sp^3 carbon ratios of 53% and 49% were deposited on FeCo/glass substrates. Heating to 300 ^{o}C led to partial reduction in sp^3 carbon content of NDLCs, ending up with a softer layer. NDLC with 49% sp^2/sp^3 carbon ratio showed better mechanical properties at 300 ^{o}C and 25 ^{o}C before and after heat treatments, indicating that the lower the sp^2/sp^3 carbon ratio, the better the mechanical properties. The same NDLC also showed lower coefficient of friction because of lower sp^2 carbon content. Wear tests revealed that NDLC with 49% sp^2/sp^3 carbon ratio also had better wear resistance at 300 ^{o}C because of improved mechanical properties. However, both NDLCs were not delaminated during wear tests at 300 ^{o}C and the average wear depths were less than 1 nm, which also indicated robustness and durability of the NDLC films.
4. Graphene oxide (GO), silk fibroin (SF) and cellulose nanocrystals (CNC) nanocomposite is a novel biomaterial with superior mechanical properties. Creep behavior of softer biomaterials are of great importance when they are subjected to elevated temperature for longer duration of time. In Chapter V, elevated temperature nanoindentation experiments using constant load hold method were

performed to investigate temperature dependent mechanical and creep behavior of the GO-SF-CNC nanocomposite. Hardness and reduced modulus of GO-SF-CNC were determined from experiments at 25 ^{o}C, 40 ^{o}C, 60 ^{o}C, 80 ^{o}C and 100 ^{o}C, and yield strength and creep coefficients were predicted from finite element analysis using two-layer viscoplasticity theory. Results showed that increasing the temperature from 25 ^{o}C to 80 ^{o}C, hardness, reduced modulus and yield strength of GO-SF-CNC nanocomposite dramatically increased by 112%, 40% and 140% respectively, and creep displacements during constant load hold reduced by 53%. It was attributed to increase in crystallizations in the nanocomposite because of increase in β-sheet formations of SF material and reduction in water molecules in CNC material. However, at 100 ^{o}C, the mechanical properties deteriorated, and creep displacements increased because of water evaporation from the nanocomposite, making it weaker. Hardness to yield strength ratio was found within 1.84-2.06. Maximum creep exponent was 2.9 at 40 ^{o}C, which reduced to 2.06 at 80 ^{o}C and again increased to 2.27 at 100 ^{o}C.

5. In Chapter VI, analytical modeling has been performed to investigate electroadhesion forces between the human fingertip and the haptics surface under the meniscus actions. A single asperity model was first proposed, and adhesive forces were predicted for different meniscus water volumes before and after applying the voltage. Results showed that before applying the voltage, the adhesion forces due to meniscus actions do not show any significant trend with water volume at any interference, because of hydrophobicity. After applying the

voltage, electrostatic forces contributed to total adhesion. Due to electrostatic effect, meniscus actions became hydrophilic and meniscus forces significantly increased. With increase in water volume, electrostatic effect also decreased at a particular interference. The single asperity model was implemented into a GW based rough surface contact model to predict adhesion behaviors over a finite area under meniscus actions. Results from rough surface modeling revealed that before applying voltage, adhesion between the surfaces were much lower and the values decreased with increasing the surface separation. However, the adhesion forces significantly increased after applying voltage. When the surfaces were in contact, the total adhesion forces did not significantly vary with water volumes. However, at positive separations, total adhesion forces were higher at lower meniscus water volume, due to electrostatic effect. Before applying voltage, pull-off forces increased with increasing the water volume due to meniscus effects. After applying voltage, pull-off forces were much higher, and the values decreased with increasing the water volumes because of electrostatic forces dominating the behavior at lower water volumes.

7.2. Recommendations for future study

In Chapters II and IV, nanoindentation and nanoscratch experiments were performed to investigate mechanical properties of NDLC/NCOC at high temperature conditions. It was found that substrate effect can influence true mechanical properties of ultra-thin films. Due to instrument limitations, substrate effects were present in the mechanical properties reported in the chapters. To obtain true mechanical properties from pure experiments, very

shallow nanoindentations need to be carried out using even more sharper indenters than those used in these studies. Also because of using diamond indenters, the maximum temperatures for all experiments were limited to 300 ^{o}C to avoid indenter oxidation. To investigate mechanical behavior of the films at even higher temperatures, other tip materials need to be used e.g., cubic boron nitride, sapphire etc. Also, all high temperature experiments need to be performed in air in order to investigate the effect of oxidation on mechanical and tribological behavior of NDLCs at elevated temperatures.

In Chapter III, finite element analysis (FEA) of nanoindentation responses were performed to obtain true mechanical properties of NDLC and other HAMR components. Especially for NDLC, mechanical properties from FEA were obtained by simultaneously changing elastic modulus and yield strength of NDLCs. To perform better analysis in future studies, elastic nanoindentations need to perform first and then use FEA to predict elastic modulus only. After that, nanoindentations with higher contact depths can be performed for plastic deformations and then yield strengths can be obtained by entering elastic modulus of the film in the FEA model. From this study, the ratio of hardness over yield strengths of NDLC were found dependent on environmental conditions. Thorough study needs to be carried out to investigate the behaviors.

Creep results from Chapter V were shown for GO based nanocomposites only. Reduced GO and annealed GO can also be considered for future biomaterial study and creep studies also need to be carried out to investigate and optimize these state-of-the art biocomposites.

In the rough surface contact model shown in Chapter VI, the human fingertip surface was considered as a smooth complaint surface. In reality, fingertip surfaces are wavy shaped,

and each ridge surface can be considered as a cylinder with a certain roughness to model the contact with the haptics surface for better prediction of interfacial forces. Also, the contact model investigated electroadhesion behavior under elastic regime only. In future studies, viscoelasticity of human skin and elastic-plastic contact also needs to consider for better understanding of electroadhesion behavior. Friction modeling also needs to be carried out considering above assumptions for better predictions.

REFERENCES

[1] Donnet C, Erdemir A. Historical developments and new trends in tribological and solid lubricant coatings. Surf Coatings Technol 2004;180–181:76–84. doi:10.1016/J.SURFCOAT.2003.10.022.

[2] Wang N, Komvopoulos K. Thermal Stability of Ultrathin Amorphous Carbon Films for Energy-Assisted Magnetic Recording. IEEE Trans Magn 2011;47:2277–82. doi:10.1109/TMAG.2011.2139221.

[3] Pathem BK, Guo X-C, Rose F, Wang N, Komvopoulos K, Schreck E, et al. Carbon Overcoat Oxidation in Heat-Assisted Magnetic Recording. IEEE Trans Magn 2013;49:3721–4. doi:10.1109/TMAG.2012.2236645.

[4] Kryder MH, Gage EC, McDaniel TW, Challener WA, Rottmayer RE, Ganping Ju, et al. Heat Assisted Magnetic Recording. Proc IEEE 2008;96:1810–35. doi:10.1109/JPROC.2008.2004315.

[5] Zhang Y, Polychronopoulou K, Humood M, Polycarpou AA. High temperature nanotribology of ultra-thin hydrogenated amorphous carbon coatings. Carbon N Y 2017;123:112–21. doi:10.1016/j.carbon.2017.07.047.

[6] Xu S, Sinha S, Rismaniyazdi E, Wolf C, Dorsey P, Knigge B. Effect of Carbon Overcoat on Heat-Assisted Magnetic Recording Performance. IEEE Trans Magn 2015;51:1–5. doi:10.1109/TMAG.2015.2445871.

[7] Wei B, Zhang B, Johnson KE. Nitrogen-induced modifications in microstructure and wear durability of ultrathin amorphous-carbon films. J Appl Phys

1998;83:2491–9. doi:10.1063/1.367009.

[8] Zou YS, Wang QM, Du H, Song GH, Xiao JQ, Gong J, et al. Structural characterization of nitrogen doped diamond-like carbon films deposited by arc ion plating. Appl Surf Sci 2005;241:295–302. doi:10.1016/j.apsusc.2004.07.043.

[9] Kiely JD, Jones PM, Wang H, Yang R, Scholz W, Benakli M, et al. Media Roughness and Head-Media Spacing in Heat-Assisted Magnetic Recording. IEEE Trans Magn 2014;50:132–6. doi:10.1109/TMAG.2013.2291684.

[10] Wu Q, Meng Y, Concha K, Wang S, Li Y, Ma L, et al. Influence of temperature and humidity on nano-mechanical properties of cellulose nanocrystal films made from switchgrass and cotton. Ind Crops Prod 2013;48:28–35. doi:10.1016/j.indcrop.2013.03.032.

[11] Hu X, Shmelev K, Sun L, Gil E-S, Park S-H, Cebe P, et al. Regulation of Silk Material Structure by Temperature-Controlled Water Vapor Annealing. Biomacromolecules 2011;12:1686–96. doi:10.1021/bm200062a.

[12] Chen H, Müller MB, Gilmore KJ, Wallace GG, Li D. Mechanically Strong, Electrically Conductive, and Biocompatible Graphene Paper. Adv Mater 2008;20:3557–61. doi:10.1002/adma.200800757.

[13] Kim S, Xiong R, Tsukruk V V. Probing Flexural Properties of Cellulose Nanocrystal–Graphene Nanomembranes with Force Spectroscopy and Bulging Test. Langmuir 2016;32:5383–93. doi:10.1021/acs.langmuir.6b01079.

[14] Li X, Choi C, Ma Y, Boonpuek P, Felts JR, Mullenbach J, et al. Electrowetting: A Consideration in Electroadhesion. IEEE Trans Haptics 2020;13:522–9.

doi:10.1109/TOH.2020.2979439.

[15] Shakil A, Amiri A, Tang H, Polycarpou AA. High temperature nanomechanical and nanotribological behavior of sub-5 nm nitrogen-doped carbon overcoat films. Appl Surf Sci 2021;535:147662. doi:10.1016/j.apsusc.2020.147662.

[16] Marchon B, Guo X-C, Pathem BK, Rose F, Dai Q, Feliss N, et al. Head–Disk Interface Materials Issues in Heat-Assisted Magnetic Recording. IEEE Trans Magn 2014;50:137–43. doi:10.1109/TMAG.2013.2283068.

[17] Wheeler JM, Oliver RA, Clyne TW. AFM observation of diamond indenters after oxidation at elevated temperatures. Diam Relat Mater 2010;19:1348–53. doi:10.1016/j.diamond.2010.07.004.

[18] Oliver WC, Pharr GM. An improved technique for determining hardness and elastic modulus using load and displacement sensing indentation experiments. J Mater Res 1992;7:1564–83. doi:10.1557/JMR.1992.1564.

[19] Pu J-C, Wang S-F, Sung JC. High-temperature oxidation behaviors of CVD diamond films. Appl Surf Sci 2009;256:668–73. doi:10.1016/j.apsusc.2009.08.042.

[20] Tayebi N, Conry TF, Polycarpou AA. Determination of hardness from nanoscratch experiments: Corrections for interfacial shear stress and elastic recovery. J Mater Res 2003;18:2150–62. doi:10.1557/JMR.2003.0301.

[21] Lee KM, Yeo C-D, Polycarpou AA. Nanomechanical Property and Nanowear Measurements for Sub-10-nm Thick Films in Magnetic Storage. Exp Mech 2007;47:107–21. doi:10.1007/s11340-006-9393-x.

[22] Lee KM, Yeo CD, Polycarpou AA. Relationship between scratch hardness and yield strength of elastic perfectly plastic materials using finite element analysis. J Mater Res 2008;23:2229–37. doi:10.1557/jmr.2008.0279.

[23] Mérel P, Tabbal M, Chaker M, Moisa S, Margot J. Direct evaluation of the sp3 content in diamond-like-carbon films by XPS. Appl Surf Sci 1998;136:105–10. doi:10.1016/S0169-4332(98)00319-5.

[24] Shekhawat A, Ritchie RO. Toughness and strength of nanocrystalline graphene. Nat Commun 2016;7:10546. doi:10.1038/ncomms10546.

[25] Wang H, Maiyalagan T, Wang X. Review on Recent Progress in Nitrogen-Doped Graphene: Synthesis, Characterization, and Its Potential Applications. ACS Catal 2012;2:781–94. doi:10.1021/cs200652y.

[26] Reddy ALM, Srivastava A, Gowda SR, Gullapalli H, Dubey M, Ajayan PM. Synthesis Of Nitrogen-Doped Graphene Films For Lithium Battery Application. ACS Nano 2010;4:6337–42. doi:10.1021/nn101926g.

[27] Joucken F, Tison Y, Le Fèvre P, Tejeda A, Taleb-Ibrahimi A, Conrad E, et al. Charge transfer and electronic doping in nitrogen-doped graphene. Sci Rep 2015;5:14564. doi:10.1038/srep14564.

[28] Schiros T, Nordlund D, Pálová L, Prezzi D, Zhao L, Kim KS, et al. Connecting Dopant Bond Type with Electronic Structure in N-Doped Graphene. Nano Lett 2012;12:4025–31. doi:10.1021/nl301409h.

[29] Fei X, Neilson J, Li Y, Lopez V, Garrett SJ, Gan L, et al. Controlled Synthesis of Nitrogen-Doped Graphene on Ruthenium from Azafullerene. Nano Lett

2017;17:2887–94. doi:10.1021/acs.nanolett.7b00038.

[30] Khurshudov A, Kato K, Sawada D. Tribological and mechanical properties of carbon nitride thin coating prepared by ion-beam-assisted deposition. Tribol Lett 1996;2. doi:10.1007/BF00182544.

[31] Yan X, Xu T, Chen G, Yang S, Liu H. Study of structure, tribological properties and growth mechanism of DLC and nitrogen-doped DLC films deposited by electrochemical technique. Appl Surf Sci 2004;236:328–35. doi:10.1016/j.apsusc.2004.05.005.

[32] Bhushan B. Chemical, mechanical and tribological characterization of ultra-thin and hard amorphous carbon coatings as thin as 3.5 nm: recent developments. Diam Relat Mater 1999;8:1985–2015. doi:10.1016/S0925-9635(99)00158-2.

[33] Tsui TY, Pharr GM, Oliver WC, Bhatia CS, White RL, Anders S, et al. Nanoindentation and Nanoscratching of Hard Carbon Coatings for Magnetic Disks. MRS Proc 1995;383:447. doi:10.1557/PROC-383-447.

[34] Cui L, Lu Z, Wang L. Probing the low-friction mechanism of diamond-like carbon by varying of sliding velocity and vacuum pressure. Carbon N Y 2014;66:259–66. doi:10.1016/j.carbon.2013.08.065.

[35] Bowden FPP, Tabor D. Friction, lubrication and wear: a survey of work during the last decade. Br J Appl Phys 1966;17:1521–44. doi:10.1088/0508-3443/17/12/301.

[36] Chang WR, Etsion I, Bogy DB. Static Friction Coefficient Model for Metallic Rough Surfaces. J Tribol 1988;110:57–63. doi:10.1115/1.3261575.

[37] Gao GT, Mikulski PT, Harrison JA. Molecular-Scale Tribology of Amorphous Carbon Coatings: Effects of Film Thickness, Adhesion, and Long-Range Interactions. J Am Chem Soc 2002;124:7202–9. doi:10.1021/ja0178618.

[38] Lee KM, Yeo C-D, Polycarpou AA. Mechanical property measurements of thin-film carbon overcoat on recording media towards 1Tbit/in2. J Appl Phys 2006;99:08G906. doi:10.1063/1.2166595.

[39] Chatterjee A, Polycarpou AA, Abelson JR, Bellon P. Nanoscratch study of hard HfB2 thin films using experimental and finite element techniques. Wear 2010;268:677–85. doi:10.1016/j.wear.2009.11.001.

[40] Miyake S, Kurosaka W, Oshimoto K. Nanometre scale mechanical properties of extremely thin diamond-like carbon films. Tribol - Mater Surfaces Interfaces 2009;3:158–64. doi:10.1179/175158309X12586382418535.

[41] Chatterjee A, Kumar N, Abelson JR, Bellon P, Polycarpou AA. Nanowear of Hafnium Diboride Thin Films. Tribol Trans 2010;53:731–8. doi:10.1080/10402001003753341.

[42] Rose F, Wang N, Smith R, Xiao Q-F, Inaba H, Matsumura T, et al. Complete characterization by Raman spectroscopy of the structural properties of thin hydrogenated diamond-like carbon films exposed to rapid thermal annealing. J Appl Phys 2014;116:123516. doi:10.1063/1.4896838.

[43] Shakil A, Polycarpou AA. High temperature nanomechanical properties of sub-5 nm nitrogen doped diamond-like carbon using nanoindentation and finite element analysis. J Appl Phys 2021;129:135302. doi:10.1063/5.0037159.

[44] Dekempeneer EHA, Meneve J, Smeets J, Kuypers S, Eersels L, Jacobs R. Structural, mechanical and tribological properties of plasma-assisted chemically vapour deposited hydrogenated CxN1−x:H films. Surf Coatings Technol 1994;68–69:621–5. doi:10.1016/0257-8972(94)90227-5.

[45] Kleinsorge B, Ferrari AC, Robertson J, Milne WI. Influence of nitrogen and temperature on the deposition of tetrahedrally bonded amorphous carbon. J Appl Phys 2000;88:1149–57. doi:10.1063/1.373790.

[46] Abaqus V. 6.14 Documentation. Dassault Syst Simulia Corp 2014;651:2–6.

[47] Radford DD, McShane GJ, Deshpande VS, Fleck NA. The response of clamped sandwich plates with metallic foam cores to simulated blast loading. Int J Solids Struct 2006;43:2243–59. doi:10.1016/j.ijsolstr.2005.07.006.

[48] Shim S, Oliver WC, Pharr GM. A critical examination of the Berkovich vs. conical indentation based on 3D finite element calculation. MRS Proc 2004;841:R9.5. doi:10.1557/PROC-841-R9.5.

[49] Yu N, Polycarpou AA, Conry TF. Tip-radius effect in finite element modeling of sub-50 nm shallow nanoindentation. Thin Solid Films 2004;450:295–303. doi:10.1016/j.tsf.2003.10.033.

[50] Rehman H ur, Ahmed F, Schmid C, Schaufler J, Durst K. Study on the deformation mechanics of hard brittle coatings on ductile substrates using in-situ tensile testing and cohesive zone FEM modeling. Surf Coatings Technol 2012;207:163–9. doi:10.1016/j.surfcoat.2012.06.049.

[51] Lee KM, Yeo C-D, Polycarpou AA. Relationship between scratch hardness and

yield strength of elastic perfectly plastic materials using finite element analysis. J Mater Res 2008;23:2229–37. doi:10.1557/JMR.2008.0279.

[52] Katta RR, Polycarpou AA, Lee S-C, Suk M. Experimental and FEA Scratch of Magnetic Storage Thin-Film Disks to Correlate Magnetic Signal Degradation With Permanent Deformation. J Tribol 2010;132:1–11. doi:10.1115/1.4000848.

[53] Katta RR, Nunez EE, Polycarpou AA, Lee S-C. Plane strain sliding contact of multilayer magnetic storage thin-films using the finite element method. Microsyst Technol 2009;15:1097–110. doi:10.1007/s00542-009-0859-5.

[54] Zhang Y, Wang H, Li X, Tang H, Polycarpou AA. A finite element correction method for sub-20 nm nanoindentation considering tip bluntness. Int J Solids Struct 2017;129:49–60. doi:10.1016/j.ijsolstr.2017.09.015.

[55] Beake BD, Smith JF. High-temperature nanoindentation testing of fused silica and other materials. Philos Mag A 2002;82:2179–86. doi:10.1080/01418610208235727.

[56] Xu Z-H, Rowcliffe D. Nanoindentation on diamond-like carbon and alumina coatings. Surf Coatings Technol 2002;161:44–51. doi:10.1016/S0257-8972(02)00364-X.

[57] Fu K, Chang L, Ye L, Yin Y. Thickness-dependent fracture behaviour of amorphous carbon films on a PEEK substrate under nanoindentation. Vacuum 2017;144:107–15. doi:10.1016/j.vacuum.2017.07.027.

[58] Cheng Y-T, Cheng C-M. Scaling approach to conical indentation in elastic-plastic solids with work hardening. J Appl Phys 1998;84:1284–91.

doi:10.1063/1.368196.

[59] Johnson KL. The correlation of indentation experiments. J Mech Phys Solids 1970;18:115–26.

[60] Robertson J. Diamond-like amorphous carbon. Mater Sci Eng R Reports 2002;37:129–281. doi:10.1016/S0927-796X(02)00005-0.

[61] Ye N, Komvopoulos K. Indentation analysis of elastic-plastic homogeneous and layered media: Criteria for determining the real material hardness. J Tribol 2003;125:685–91. doi:10.1115/1.1572515.

[62] Liskiewicz TW, Beake BD, Schwarzer N, Davies MI. Short note on improved integration of mechanical testing in predictive wear models. Surf Coatings Technol 2013;237:212–8. doi:10.1016/j.surfcoat.2013.07.044.

[63] Chudoba T, Schwarzer N, Richter F. Steps towards a mechanical modeling of layered systems. Surf Coatings Technol 2002;154:140–51. doi:10.1016/S0257-8972(02)00016-6.

[64] Shakil A, Amiri A, Polycarpou AA. Effect of Carbon Configuration on Mechanical, Friction and Wear Behavior of Nitrogen-Doped Diamond-Like Carbon Films for Magnetic Storage Applications. Tribol Lett 2021;69:151. doi:10.1007/s11249-021-01525-8.

[65] Mangolini F, Krick BA, Jacobs TDB, Khanal SR, Streller F, McClimon JB, et al. Effect of silicon and oxygen dopants on the stability of hydrogenated amorphous carbon under harsh environmental conditions. Carbon N Y 2018;130:127–36. doi:10.1016/j.carbon.2017.12.096.

[66] Kalin M, Vižintin J, Barriga J, Vercammen K, Acker K van., Arnšek A. The Effect of Doping Elements and Oil Additives on the Tribological Performance of Boundary-Lubricated DLC/DLC Contacts. Tribol Lett 2004;17:679–88. doi:10.1007/s11249-004-8073-1.

[67] Mangolini F, McClimon JB, Segersten J, Hilbert J, Heaney P, Lukes JR, et al. Silicon Oxide-Rich Diamond-Like Carbon: A Conformal, Ultrasmooth Thin Film Material with High Thermo-Oxidative Stability. Adv Mater Interfaces 2019;6:1801416. doi:10.1002/admi.201801416.

[68] Zeng C, Chen Q, Xu M, Deng S, Luo Y, Wu T. Enhancement of mechanical, tribological and morphological properties of nitrogenated diamond-like carbon films by gradient nitrogen doping. Diam Relat Mater 2017;76:132–40. doi:10.1016/j.diamond.2017.05.004.

[69] Bootkul D, Supsermpol B, Saenphinit N, Aramwit C, Intarasiri S. Nitrogen doping for adhesion improvement of DLC film deposited on Si substrate by Filtered Cathodic Vacuum Arc (FCVA) technique. Appl Surf Sci 2014;310:284–92.

[70] Ferrari AC, Rodil SE, Robertson J. Interpretation of infrared and Raman spectra of amorphous carbon nitrides. Phys Rev B 2003;67:155306. doi:10.1103/PhysRevB.67.155306.

[71] Lee KM, Yeo C-D, Polycarpou AA. Mechanical property measurements of thin-film carbon overcoat on recording media towards 1Tbit/in2. J Appl Phys 2006;99:08G906. doi:10.1063/1.2166595.

[72] Bowden FP, Tabor D. Friction, lubrication and wear: a survey of work during the last decade. Br J Appl Phys 1966;17:1521–44. doi:10.1088/0508-3443/17/12/301.

[73] Kaciulis S. Spectroscopy of carbon: from diamond to nitride films. Surf Interface Anal 2012;44:1155–61.

[74] Mezzi A, Kaciulis S. Surface investigation of carbon films: from diamond to graphite. Surf Interface Anal 2010;42:1082–4.

[75] Mizokawa Y, Miyasato T, Nakamura S, Geib KM, Wilmsen CW. Comparison of the CKLL first-derivative auger spectra from XPS and AES using diamond, graphite, SiC and diamond-like-carbon films. Surf Sci 1987;182:431–8.

[76] Lascovich JC, Giorgi R, Scaglione S. Evaluation of the sp2/sp3 ratio in amorphous carbon structure by XPS and XAES. Appl Surf Sci 1991;47:17–21.

[77] Mizokawa Y, Miyasato T, Nakamura S, Geib KM, Wilmsen CW. The CKLL first-derivative x-ray photoelectron spectroscopy spectra as a fingerprint of the carbon state and the characterization of diamondlike carbon films. J Vac Sci Technol A Vacuum, Surfaces, Film 1987;5:2809–13.

[78] Tabbal M, Mérel P, Chaker M, El Khakani MA, Herbert EG, Lucas BN, et al. Effect of laser intensity on the microstructural and mechanical properties of pulsed laser deposited diamond-like-carbon thin films. J Appl Phys 1999;85:3860–5. doi:10.1063/1.369757.

[79] HIRATSUKA M, NAKAMORI H, KOGO Y, SAKURAI M, OHTAKE N, SAITOH H. Correlation between Optical Properties and Hardness of Diamond-Like Carbon Films. J Solid Mech Mater Eng 2013;7:187–98.

doi:10.1299/jmmp.7.187.

[80] Tallant DR, Parmeter JE, Siegal MP, Simpson RL. The thermal stability of diamond-like carbon. Diam Relat Mater 1995;4:191–9. doi:10.1016/0925-9635(94)00243-6.

[81] Tsui TY, Pharr GM, Oliver WC, Chung YW, Cutiongco EC, Bhatia CS, et al. Nanoindentation and nanoscratching of hard coating materials for magnetic disks. Mater. Res. Soc. Symp. - Proc., 1995.

[82] Zhang Y, Polychronopoulou K, Humood M, Polycarpou AA. High temperature nanotribology of ultra-thin hydrogenated amorphous carbon coatings. Carbon N Y 2017;123:112–21. doi:10.1016/j.carbon.2017.07.047.

[83] Bhushan B. Introduction to tribology. John Wiley & Sons; 2013.

[84] McCue I, Ryan S, Hemker K, Xu X, Li N, Chen M, et al. Size Effects in the Mechanical Properties of Bulk Bicontinuous Ta/Cu Nanocomposites Made by Liquid Metal Dealloying. Adv Eng Mater 2016;18:46–50. doi:10.1002/adem.201500219.

[85] Wegst UGK, Bai H, Saiz E, Tomsia AP, Ritchie RO. Bioinspired structural materials. Nat Mater 2015;14:23–36. doi:10.1038/nmat4089.

[86] Shi Y, Jiang S, Zhou K, Bao C, Yu B, Qian X, et al. Influence of g-C 3 N 4 Nanosheets on Thermal Stability and Mechanical Properties of Biopolymer Electrolyte Nanocomposite Films: A Novel Investigation. ACS Appl Mater Interfaces 2014;6:429–37. doi:10.1021/am4044932.

[87] Gao Y, Xu H, Cheng Q. Multiple synergistic toughening graphene

nanocomposites through cadmium ions and cellulose nanocrystals. Adv Mater Interfaces 2018;5:1800145.

[88] Wang Y, Ma R, Hu K, Kim S, Fang G, Shao Z, et al. Dramatic Enhancement of Graphene Oxide/Silk Nanocomposite Membranes: Increasing Toughness, Strength, and Young's modulus via Annealing of Interfacial Structures. ACS Appl Mater Interfaces 2016;8:24962–73. doi:10.1021/acsami.6b08610.

[89] Li Y-Q, Yu T, Yang T-Y, Zheng L-X, Liao K. Bio-Inspired Nacre-like Composite Films Based on Graphene with Superior Mechanical, Electrical, and Biocompatible Properties. Adv Mater 2012;24:3426–31. doi:10.1002/adma.201200452.

[90] Zhang N, Yang S, Xiong L, Hong Y, Chen Y. Nanoscale toughening mechanism of nacre tablet. J Mech Behav Biomed Mater 2016;53:200–9. doi:10.1016/j.jmbbm.2015.08.020.

[91] Phiri J, Johansson L-S, Gane P, Maloney T. A comparative study of mechanical, thermal and electrical properties of graphene-, graphene oxide- and reduced graphene oxide-doped microfibrillated cellulose nanocomposites. Compos Part B Eng 2018;147:104–13. doi:10.1016/j.compositesb.2018.04.018.

[92] Xiong R, Hu K, Zhang S, Lu C, Tsukruk V V. Ultrastrong Freestanding Graphene Oxide Nanomembranes with Surface-Enhanced Raman Scattering Functionality by Solvent-Assisted Single-Component Layer-by-Layer Assembly. ACS Nano 2016;10:6702–15. doi:10.1021/acsnano.6b02012.

[93] Zhu J, Andres CM, Xu J, Ramamoorthy A, Tsotsis T, Kotov NA. Pseudonegative

Thermal Expansion and the State of Water in Graphene Oxide Layered Assemblies. ACS Nano 2012;6:8357–65. doi:10.1021/nn3031244.

[94] Ho M, Wang H, Lau K, Lee J, Hui D. Interfacial bonding and degumming effects on silk fibre/polymer biocomposites. Compos Part B Eng 2012;43:2801–12. doi:10.1016/j.compositesb.2012.04.042.

[95] Wang S, Ning H, Hu N, Huang K, Weng S, Wu X, et al. Preparation and characterization of graphene oxide/silk fibroin hybrid aerogel for dye and heavy metal adsorption. Compos Part B Eng 2019;163:716–22. doi:10.1016/j.compositesb.2018.12.140.

[96] Xie W, Tadepalli S, Park SH, Kazemi-Moridani A, Jiang Q, Singamaneni S, et al. Extreme mechanical behavior of nacre-mimetic graphene-oxide and silk nanocomposites. Nano Lett 2018;18:987–93.

[97] Moon RJ, Martini A, Nairn J, Simonsen J, Youngblood J. Cellulose nanomaterials review: Structure, properties and nanocomposites. Chem Soc Rev 2011;40:3941–94. doi:10.1039/c0cs00108b.

[98] Wen Y, Wu M, Zhang M, Li C, Shi G. Topological Design of Ultrastrong and Highly Conductive Graphene Films. Adv Mater 2017;29:1702831. doi:10.1002/adma.201702831.

[99] Xiong R, Kim HS, Zhang S, Kim S, Korolovych VF, Ma R, et al. Template-Guided Assembly of Silk Fibroin on Cellulose Nanofibers for Robust Nanostructures with Ultrafast Water Transport. ACS Nano 2017;11:12008–19. doi:10.1021/acsnano.7b04235.

[100] Chu JH, Tong LB, Zhang JB, Kamado S, Jiang ZH, Zhang HJ, et al. Bio-inspired graphene-based coatings on Mg alloy surfaces and their integrations of anti-corrosive/wearable performances. Carbon N Y 2019;141:154–68. doi:10.1016/j.carbon.2018.09.047.

[101] Salari S, Rahman MS, Polycarpou AA, Beheshti A. Elevated temperature mechanical properties of Inconel 617 surface oxide using nanoindentation. Mater Sci Eng A 2020;788:139539. doi:10.1016/j.msea.2020.139539.

[102] Bullock CJ, Bussy C. Biocompatibility Considerations in the Design of Graphene Biomedical Materials. Adv Mater Interfaces 2019;6:1900229. doi:10.1002/admi.201900229.

[103] Hummers WS, Offeman RE. Preparation of Graphitic Oxide. J Am Chem Soc 1958;80:1339–1339. doi:10.1021/ja01539a017.

[104] Zhou G, Shao Z, Knight DP, Yan J, Chen X. Silk Fibers Extruded Artificially from Aqueous Solutions of Regenerated Bombyx mori Silk Fibroin are Tougher than their Natural Counterparts. Adv Mater 2009;21:366–70. doi:10.1002/adma.200800582.

[105] Bondeson D, Mathew A, Oksman K. Optimization of the isolation of nanocrystals from microcrystalline cellulose by acid hydrolysis. Cellulose 2006;13:171–80. doi:10.1007/s10570-006-9061-4.

[106] Feng G, Ngan AHW. Effects of Creep and Thermal Drift on Modulus Measurement Using Depth-sensing Indentation. J Mater Res 2002;17:660–8. doi:10.1557/JMR.2002.0094.

[107] Solasi R, Zou Y, Huang X, Reifsnider K. A time and hydration dependent viscoplastic model for polyelectrolyte membranes in fuel cells. Mech Time-Dependent Mater 2008;12:15–30. doi:10.1007/s11043-007-9040-7.

[108] Shirazi HA, Asnafi A, Navidbakhsh M, Ayatollahi MR. To study the effects of nano-additives and nano-indentation variables on viscoplastic behaviour of a polymeric orthopaedic bone cement. Mater Res Express 2019;6. doi:10.1088/2053-1591/ab66f5.

[109] Freddi G, Tsukada M, Beretta S. Structure and physical properties of silk fibroin/polyacrylamide blend films. J Appl Polym Sci 1999;71:1563–71. doi:10.1002/(SICI)1097-4628(19990307)71:10<1563::AID-APP4>3.0.CO;2-E.

[110] Man Z, Muhammad N, Sarwono A, Bustam MA, Kumar MV, Rafiq S. Preparation of Cellulose Nanocrystals Using an Ionic Liquid. J Polym Environ 2011;19:726–31. doi:10.1007/s10924-011-0323-3.

[111] Magoshi J, Nakamura S. Studies on physical properties and structure of silk. Glass transition and crystallization of silk fibroin. J Appl Polym Sci 1975;19:1013–5. doi:10.1002/app.1975.070190410.

[112] Choudhuri JR, Vanzo D, Madden PA, Salanne M, Bratko D, Luzar A. Dynamic Response in Nanoelectrowetting on a Dielectric. ACS Nano 2016;10:8536–44. doi:10.1021/acsnano.6b03753.

[113] Bratko D, Daub CD, Leung K, Luzar A. Effect of field direction on electrowetting in a nanopore. J Am Chem Soc 2007;129:2504–10. doi:10.1021/ja0659370.

[114] Quilliet C, Berge B. Electrowetting: A recent outbreak. Curr Opin Colloid

Interface Sci 2001;6:34–9. doi:10.1016/S1359-0294(00)00085-6.

[115] Argatov II, Borodich FM. A Macro Model for Electroadhesive Contact of a Soft Finger With a Touchscreen. IEEE Trans Haptics 2020;13:504–10. doi:10.1109/TOH.2020.2969628.

[116] Li X, Ma Y, Choi C, Ma X, Chatterjee S, Lan S, et al. Electroadhesion-Based Haptics: Nanotexture Shape and Surface Energy Impact on Electroadhesive Human–Machine Interface Performance (Adv. Mater. 31/2021). Adv Mater 2021;33:2170240. doi:10.1002/adma.202170240.

[117] Greenwood JA, Williamson JBP. Contact of nominally flat surfaces. Proc R Soc London Ser A Math Phys Sci 1966;295:300–19. doi:10.1098/rspa.1966.0242.

[118] Gao C, Tian X, Bhushan B. A Meniscus Model for Optimization of Texturing and Liquid Lubrication of Magnetic Thin-Film Rigid Disks. Tribol Trans 1995;38:201–12. doi:10.1080/10402009508983397.

[119] Gui J, Marchon B. A stiction model for a head-disk interface of a rigid disk drive. J Appl Phys 1995;78:4206–17. doi:10.1063/1.359882.

[120] Tian H, Matsudaira T. The Role of Relative Humidity, Surface Roughness and Liquid Build-Up on Static Friction Behavior of the Head/Disk Interface. J Tribol 1993;115:28–35. doi:10.1115/1.2920983.

[121] Maugis D. Adhesion of spheres: The JKR-DMT transition using a dugdale model. J Colloid Interface Sci 1992;150:243–69. doi:10.1016/0021-9797(92)90285-T.

[122] Shi X, Polycarpou AA. Adhesive transition from noncontacting to contacting elastic spheres: extension of the Maugis–Dugdale model. J Colloid Interface Sci

2005;281:449–57. doi:10.1016/j.jcis.2004.08.069.

[123] Johnson KL. Mechanics of adhesion. Tribol Int 1998;31:413–8. doi:10.1016/S0301-679X(98)00060-7.

[124] Xue X, Polycarpou AA. An improved meniscus surface model for contacting rough surfaces. J Colloid Interface Sci 2007;311:203–11. doi:10.1016/j.jcis.2007.02.038.

[125] Rodríguez Urribarrí AC, van der Heide E, Zeng X, de Rooij MB. Modelling the static contact between a fingertip and a rigid wavy surface. Tribol Int 2016;102:114–24. doi:10.1016/j.triboint.2016.05.028.

[126] Mavon A, Zahouani H, Redoules D, Agache P, Gall Y, Humbert P. Sebum and stratum corneum lipids increase human skin surface free energy as determined from contact angle measurements: A study on two anatomical sites. Colloids Surfaces B Biointerfaces 1997;8:147–55. doi:10.1016/S0927-7765(96)01317-3.

[127] Yuan Y, Verma R. Measuring microelastic properties of stratum corneum. Colloids Surfaces B Biointerfaces 2006;48:6–12. doi:10.1016/j.colsurfb.2005.12.013.

[128] Yamamoto T, Yamamoto Y. Dielectric constant and resistivity of epidermal stratum corneum. Med Biol Eng 1976;14:494–500. doi:10.1007/BF02478045.

[129] Machado-Moreira C, Aviation JC-, space undefined, and undefined, 2008 undefined. Sweat secretion from palmar and dorsal surfaces of the hands during passive and active heating. IngentaconnectCom 2008;79:1034–40. doi:10.3357/ASEM.2354.2008.

[130] Israelachvili J. Intermolecular and Surface Forces. Elsevier; 2011. doi:10.1016/C2009-0-21560-1.

[131] Wang L, Rong W, Guo B, Huang G, Sun L. Dynamic Separation of a Sphere from a Flat or Sphere in the Presence of a Liquid Meniscus. Tribol Trans 2011;54:542–7. doi:10.1080/10402004.2011.575534.

[132] Johnson KL. Contact mechanics. Cambridge university press; 1987.

[133] Derjaguin B V., Muller VM, Toporov YP. Effect of contact deformations on the adhesion of particles. J Colloid Interface Sci 1975;53:314–26. doi:10.1016/0021-9797(75)90018-1.

[134] Johnson KL, Kendall K, Roberts A. Surface energy and the contact of elastic solids. Proc R Soc London A Math Phys Sci 1971;324:301–13. doi:10.1098/rspa.1971.0141.

[135] Klarman D, Andelman D. A model of electrowetting, reversed electrowetting, and contact angle saturation. Langmuir 2011;27:6031–41. doi:10.1021/la2004326.

[136] Lin J-L, Lee G-B, Chang Y-H, Lien K-Y. Model Description of Contact Angles in Electrowetting on Dielectric Layers. Langmuir 2006;22:484–9. doi:10.1021/la052011h.

[137] Li Y, Talke FE. A Model for the Effect of Humidity on Stiction of the Head/Disk Interface. Tribol Trans 1992;35:429–34. doi:10.1080/10402009208982139.

[138] Suh AY, Polycarpou AA. Adhesive contact modeling for sub-5-nm ultralow flying magnetic storage head-disk interfaces including roughness effects. J Appl Phys 2005;97:104328. doi:10.1063/1.1914951.

APPENDIX A

XPS ADDITIONAL ANALYSIS OF NCOC FILMS (CHAPTER II)

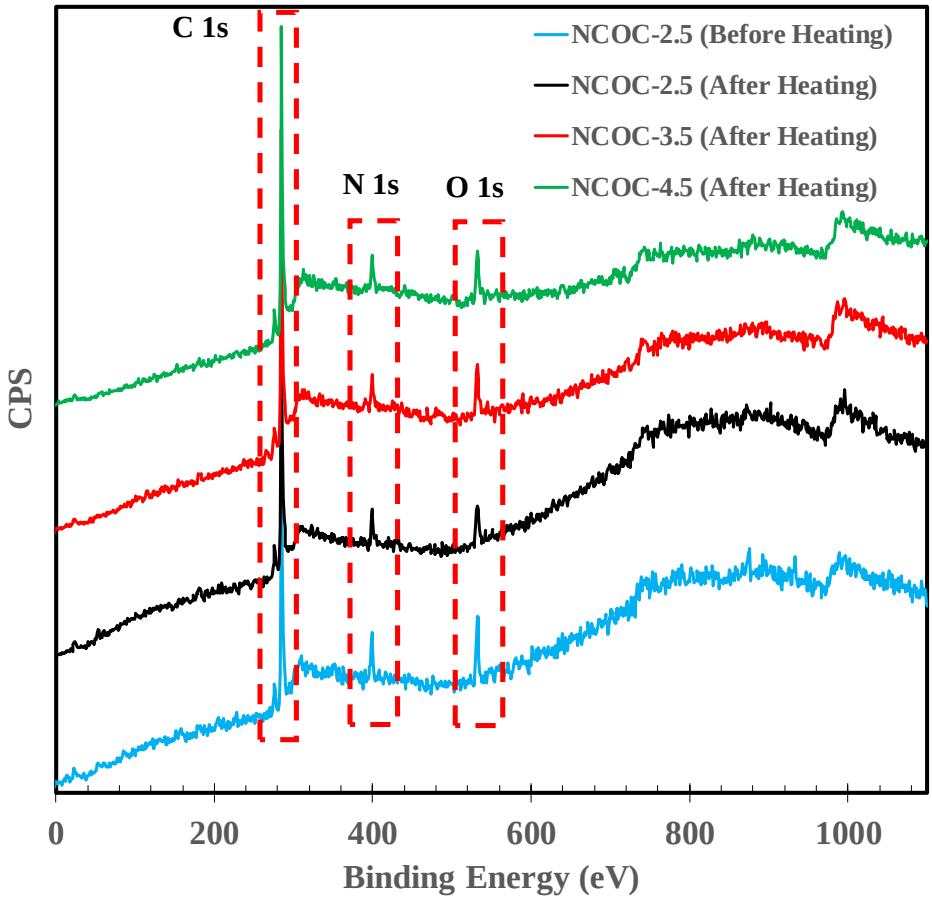

Figure A1: XPS survey spectra of NCOC-2.5 before heat treatment process, and NCOC-2.5, NCOC-3.5 and NCOC-4.5 after heat treatment process.

APPENDIX B

FEA-PREDICTED MECHANICAL PROPERTIES OF NDLCS AT DIFFERENT CONTACT DEPTHS (CHAPTER III)

Figure B1 shows FEA-predicted nanomechanical properties of NDLCs at different contact depths. Nanomechanical properties were taken from Table 8 and corresponding contact depths were calculated from nanoindentation experiments (Figures. 16 and 17) using the Oliver-Pharr method. The contact depth range shown (1.5-3.0 nm) are way above 10% of NDLC film thicknesses, at which true mechanical properties without substrate effects cannot be determined from pure experiments. Therefore, FEA was used in this study to obtain true NDLC properties, which are independent of contact depth.

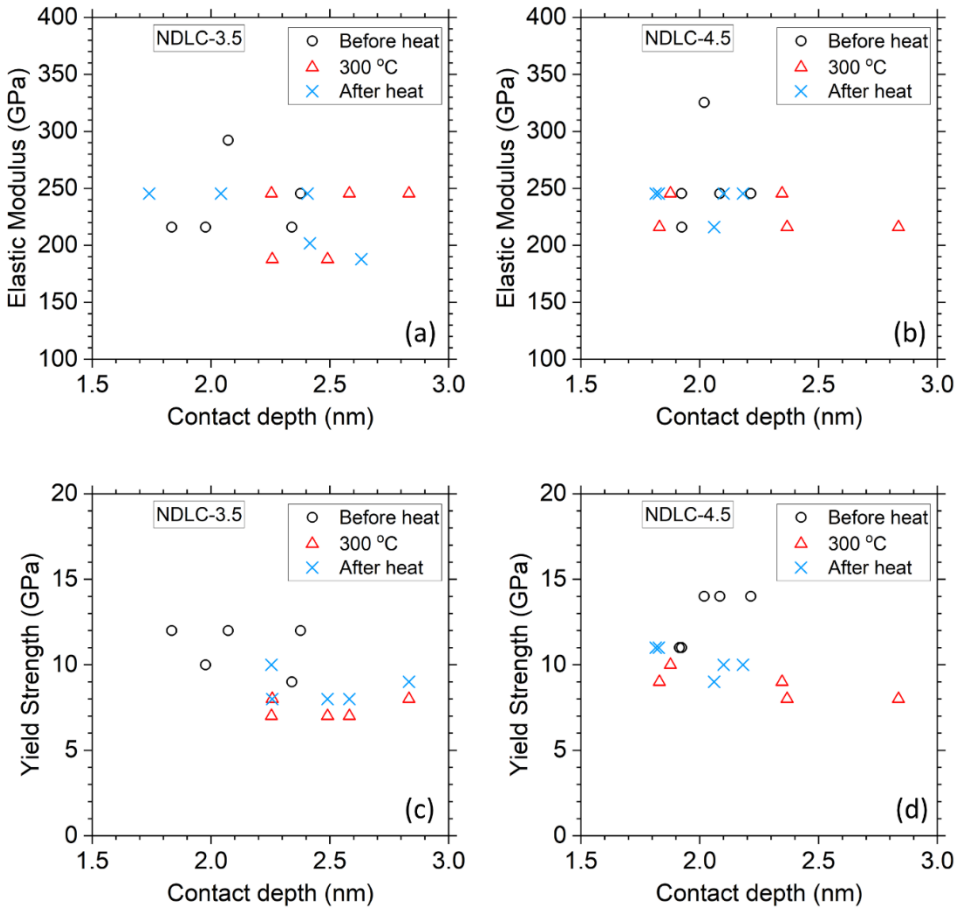

Figure B1. FEA-predicted mechanical properties of NDLCs at different experimental contact depths and different temperature conditions; (a) Elastic modulus of NDLC-3.5, (b) Elastic modulus of NDLC-4.5, (c) Yield strength of NDLC-3.5, (d) Yield strength of NDLC-4.5.

APPENDIX C

NANOINDENTATION OF NDLC SAMPLES (CHAPTER IV)

Nanoindentation experiments were performed to determine reduced modulus of NDLCs at three experimental conditions- 25 ^{o}C before heat, 300 ^{o}C and 25 ^{o}C after heat. Steps of a typical nanoindentation experiment involve: loading the indenter in 5 seconds from the initial load to the maximum load, holding the maximum load for 2 seconds to reduce any creep effects and finally unloading in 5 seconds to initial load. Displacement responses were measured for the loading steps from nanoindentation experiments. Oliver-Pharr method was used to determine reduced modulus of NDLCs from load-displacement responses. A cube corner indenter with a radius of 85 nm was used for nanoindentations. Maximum nanoindentation loads were in the range of 26-32 μN and resulting contact depths were within 3.3-4.2 nm.

Figures. C1(a) and C1(b) show nanoindentation load displacement responses of NDLC-1 and NDLC-2 samples respectively for the normal load of 28 μN. From the responses, it was evident that NDLC-1 and NDLC-2 had similar maximum displacement at 25 ^{o}C before and after heat treatment. However, NDLC-1 showed higher maximum displacement at 300 ^{o}C compared to NDLC-2. Residual nanoindentation depths of NDLC-1 were also found larger than that of NDLC-2 at all three experimental conditions. This implies that because or lesser relative sp^3 carbon and nitrogen contents at all conditions, NDLC-1 underwent higher plastic deformations than NDLC-2 under the same load.

Fig. C1(c) depicts the reduced modulus results of NDLCs at all experimental conditions. No significant trend of reduced modulus was found with temperature and chemical composition of NDLCs. Nanoindenatation contact depths were much higher than 10% of film thicknesses of NDLCs, therefore, nanoindentation results were affected by substrate material. Because of this, nanoindentation hardness results were not reported in this study. Instead, nanoscratch tests were performed which can determine NDLC hardnesses at all experimental conditions with minimal substrate effect. For nanoscratch calculations, elastic modulus of NDLCs were required, which were entered from the reduced modulus results shown in Fig. C1(c).

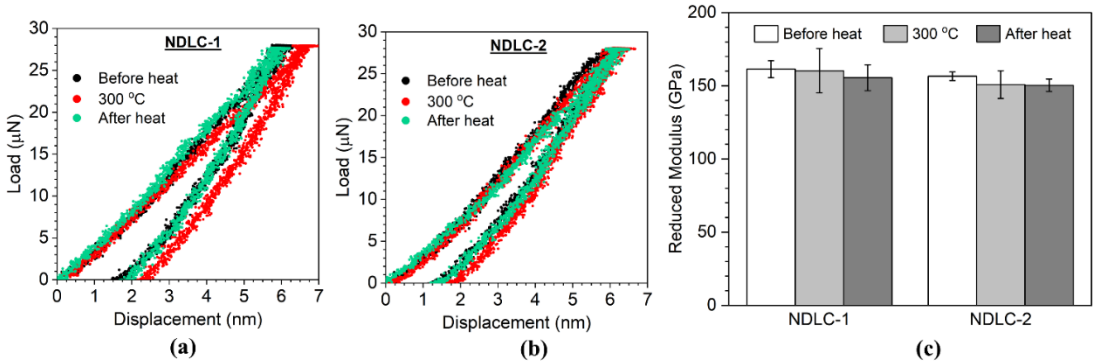

Figure C1. Nanoindentation load-displacement responses of **(a)** NDLC-1; **(b)** NDLC-2 at 25 °C before heating, 300 °C, and 25 °C after heating. **(c)** Reduced modulus of NDLCs determined from nanoindentation experiments. Error bars designate ± one standard deviation.

APPENDIX D

DETERMINATION OF INDENTER GEOMETRY OF THE FEA MODEL AND MODEL VALIDATION (CHAPTER V)

To determine the indenter geometry of the FEA model (section 5.3.1), a standard fused quartz (FQ) sample with known elastic modulus of 72 GPa was used, following the works from the literature [43,54]. First, very shallow nanoindentations were performed on the FQ sample so that the load-displacement response is elastic, as shown in Fig D1(a). In this case, the indenter acted as a flat punch pushing the FQ sample without any plastic deformation. The experimental response was simulated by considering FQ as the only material in the FEA model and the elastic modulus of FQ was entered into the model. From the simulations, the flat part length 'a' was determined as 12.5 nm for the indenter radius 'R' of 80 nm. To validate the indenter geometry, several nanoindentations were performed at higher loads on FQ; and finite element simulations were performed using the indenter geometry to predict yield strength and elastic modulus of FQ. Figure D1(b) shows the experimental and FEA load-displacement responses for FQ at the maximum load of 50 μN. Summary of the FEA predicted FQ properties are shown in Table D1. From the table, the average elastic modulus and yield strength were found as 69.5 GPa and 5.0 GPa respectively, which were within the range found from the literature [48,49]. This validated the FEA model for creep behavior study of GO-SF-CNC nanocomposite.

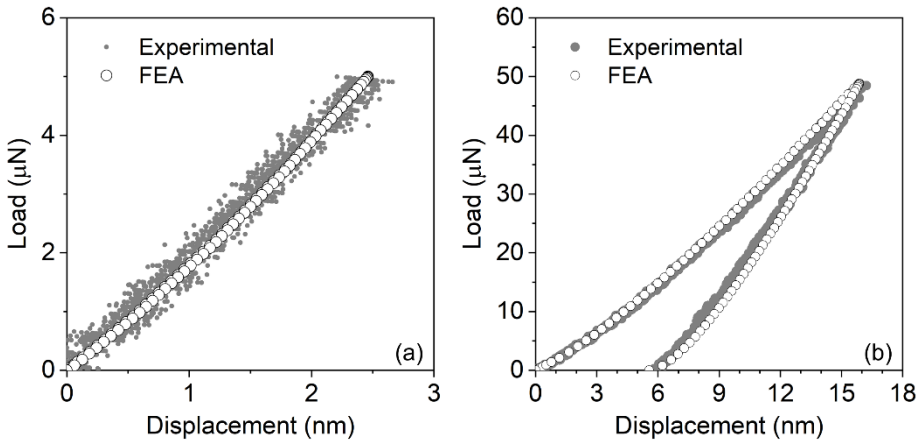

Figure D1. (a) Elastic nanoindentation on FQ sample and fitted FEA response for indenter geometry determination. (b) Experimental and FEA responses of nanoindentation on the FQ sample at 50 μN load.

Table D1. FEA predicted mechanical properties of fused quartz at different loads.

Indenter	**Load (μN)**	5	15	35	50	70	110	**Average**	**Yu et al. (2004)** [49]	**Shim et al. (2005)** [48]
R: 80 nm *a*: 12.5 nm	**Elastic Modulus (GPa)**	72	72	68	69	68	68	**69.5**	67.6	72
	Yield Strength (GPa)	-	4.6	5.0	5.1	5.1	5.3	**5.0**	4.3	5.5

APPENDIX E

AREAL FUNCTION OF NANOINDENTATION CREEP EXPERIMENTS AND MECHANICAL PROPERTIES OF SILICON SUBSTRATE (CHAPTER V)

Areal function of nanoindentation creep experiments

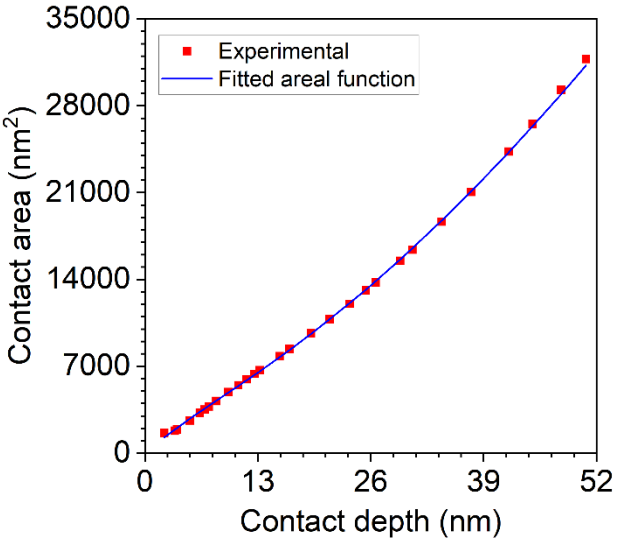

Figure E1. Areal function for nanoindentation creep experiments

Figure E1 shows the areal function for nanoindentation creep experiments, which is given by,

$$A_c = 2.598h_c^2 + 1438.47h_c^0 - 38975.46h_c^{1/2} + 279502.25h_c^{1/4} - 586406.94h_c^{1/8} + 345188.50h_c^{1/16}$$

Where, A_c and h_c are contact area and contact depth respectively. Areal function was determined by performing multiple nanoindentation experiments on a standard fused quartz sample with known mechanical properties.

Mechanical properties of silicon substrate

Mechanical properties of silicon substrate were needed for FEA simulations and therefore nanoindentation experiments with trapezoidal load function were performed on bare silicon substrate at different temperature conditions, 25 ^{o}C, 40 ^{o}C, 60 ^{o}C, 80 ^{o}C and 100 ^{o}C. Figure E2 shows nanoindentation load-displacement responses of bare silicon for the maximum load of 60 µN at 25 ^{o}C and 100 ^{o}C. it is evident from the figure that the load-displacement curves were overlapped, implying that mechanical properties were not significantly affected by the temperature range used in this study. Hardness and reduced modulus of the silicon substrate within the temperature range was determined as 11.9 ± 0.1 GPa and 149.7 ± 4.0 GPa respectively. Using the hardness to yield strength ratio of 2.8, the average yield strength of the silicon was determined as 4.2 GPa within the temperature range. These mechanical properties were directly fed into the FEA model for creep study of GO-SF-CNC nanocomposite at different temperature conditions.

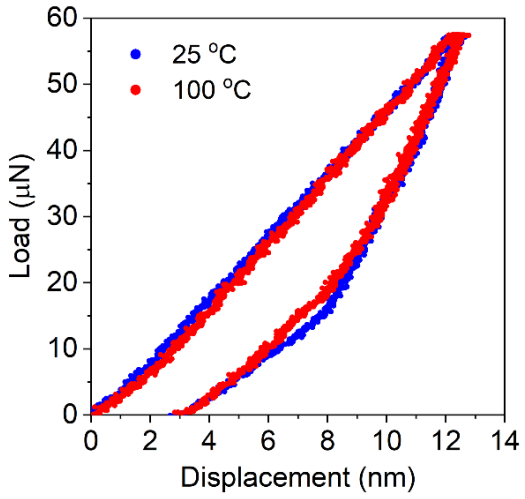

Figure E2. Nanoindentation load-displacement responses of bare silicon at different temperature conditions.

APPENDIX F

ASPERITY RADIUS DETERMINATION FOR THE SINGLE ASPERITY MODEL

(CHAPTER VI)

Asperity radius determination for single asperity model

Figure F1 shows the truncated trapezoidal asperity used by Xinyi et al. in their single asperity electroadhesion model. as shown in the figure, the top radius, bottom radius, slope and base radius was fixed as 0.5 µm, 2 µm, 12 ^{o} and 2 µm respectively. only the height was varied in their model. For the study in Chapter VI, the height of 318.8 nm was chosen, and the trapezoidal geometry was fitted with an equivalent spherical radius, as shown in Figure F2. The fitted asperity radius was 6.4 um and used in the study of Chapter VI.

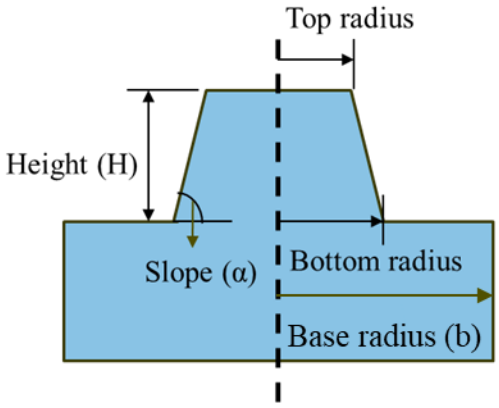

Figure F1. Truncated trapezoidal asperity geometry from Xinyi et al. model [116]

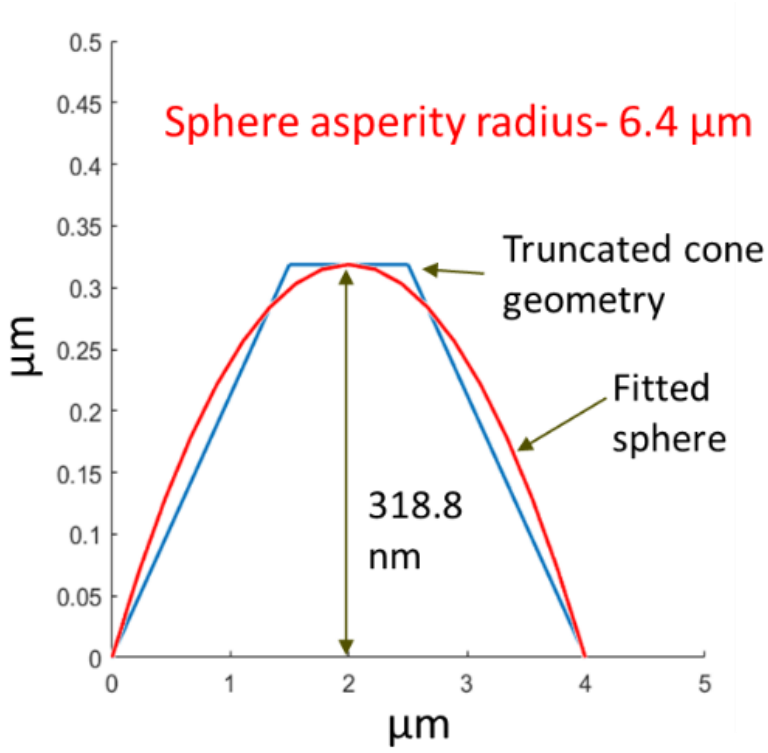

Figure F2. Truncated trapezoidal asperity and fitted spherical geometry.